IN SITU REAL-TIME VISUALIZATION AND CORROSION TESTING OF STAINLESS STEEL 316LVM WITH EMPHASIS ON DIGITAL IN-LINE HOLOGRAPHIC MICROSCOPY

by

Peter Edward Klages

Submitted in partial fulfillment of the
requirements for the degree of
Doctor of Philosophy

at

Dalhousie University
Halifax, Nova Scotia
August 2012

DALHOUSIE UNIVERSITY

DEPARTMENT OF PHYSICS AND ATMOSPHERIC SCIENCE

The undersigned hereby certify that they have read and recommend to the Faculty of Graduate Studies for acceptance a thesis entitled "*IN SITU* REAL-TIME VISUALIZATION AND CORROSION TESTING OF STAINLESS STEEL 316LVM WITH EMPHASIS ON DIGITAL IN-LINE HOLOGRAPHIC MICROSCOPY" by Peter Edward Klages in partial fulfillment of the requirements for the degree of Doctor of Philosophy.

Dated: August 17, 2012

External Examiner: _____
Dr. A. Jochen Lauterbach

Research Supervisor: _____
Dr. Harm H. Rotermund

Examining Committee: _____
Dr. Manfred H. Jericho

_____
Dr. H. Jürgen Kreuzer

Departmental Representative: _____
Dr. Daniel Labrie

DALHOUSIE UNIVERSITY

DATE: August 17, 2012

AUTHOR: Peter Edward Klages

TITLE: *IN SITU* REAL-TIME VISUALIZATION AND CORROSION
            TESTING OF STAINLESS STEEL 316LVM WITH EMPHASIS ON
            DIGITAL IN-LINE HOLOGRAPHIC MICROSCOPY

DEPARTMENT OR SCHOOL: Department of Physics and Atmospheric Science

DEGREE: Ph.D.   CONVOCATION: October   YEAR: 2012

_____
Signature of Author

I would like to dedicate this thesis to the memory of A. M. J., who believed in me enough to take the time to arrange for me to meet Harm Rotermund and to encourage me to start this degree, to my family who supported me throughout all of my degrees, and to P. S., who has helped me in so many ways, including helping me to finally believe in myself enough to finish.

Table of Contents

List of Figures

Abstract

Digital in-line holographic microscopy (DIHM) has been incorporated as an additional simultaneous *in situ* optical technique with ellipsomicroscopy for surface imaging and microscopy to study metastable pitting corrosion on stainless steel 316LVM in simulated biological solutions. DIHM adds microscopic volume imaging, allows one to detect local changes of the index of refraction in the vicinity of a pitting event, and allows one to track tracer particles and/or material ejected from the pitting sites.

To improve the pitting corrosion resistance of stainless steel 316LVM, a simple surface treatment was tested and the aforementioned imaging techniques were used to verify that pitting occurred only on the wire face. Treatments consisted of polishing the samples to remove the passive layer, then immersing the wires in 90 °C nanopure water for several hours. Treated wires show a marked increase in pitting corrosion resistance over untreated wires: the pit initiation potential increases by a minimum of 200 mV. Additional testing with scanning electron microscopy and energy dispersive X-ray spectroscopy indicate that the removal of sulphide inclusions from the surface is the most probable cause of this enhancement.

To increase holographic reconstruction performance, Graphics Processing Units (GPUs) have been used; 4 Mpixel holograms are reconstructed using the dot product approximation of the Kirchhoff-Fresnel integral in 60 ms on a Tesla c1060 GPU. Errors in sizes and positions can easily be as large as 5 to 10 % for regions where the dot product approximation is not valid, so algorithms with fewer or no approximations are also required. Reconstructions for arbitrary holographic geometries using the full Kirchhoff-Fresnel integral take approximately 1 hour (compared to 1 week on a quad-core CPU), and reconstructions using convolution methods, in which the results of 256 reconstructions at 4096×4096 pixels in one plane are combined, take 17 s. This method is almost exact, with approximations only in the obliquity factor.

List of Abbreviations and Symbols Used

A_{ref}	-	Amplitude of the reference wave
Ag/AgCl	-	Silver/Silver Chloride
AISI	-	American Iron and Steel Institute
Cl^-	-	Negative Chloride ion
CMOS	-	Complementary Metal Oxide Semiconductor
$\cos(\mathbf{r}, \mathbf{n})$	-	Cosine of the angle between vectors $\mathbf{r}$ and $\mathbf{n}$
CPU	-	Central Processing Unit
CUDA	-	Compute Unified Device Architecture
d	-	Object to sensor distance $\equiv Z - z$
$\frac{\partial}{\partial n}$	-	Partial derivative with respect to the normal of the aperture
		or recording screen (context dependent)
δx	-	Lateral spacing between pixel sites
DIHM	-	Digital In-line Holographic Microscopy
DP	-	Dot Product
ds	-	Infinitesimal area element
ECC	-	Error Correction Code
EDS	-	Energy Dispersive x-ray Spectroscopy
EMSI	-	EllipsoMicroscopy for Surface Imaging
exp	-	Exponential with base e $\equiv 2.7182818...$
FeS	-	Iron Sulphide
FLOPS	-	FLoating point Operations Per Second
FFT	-	Fast Fourier Transform
FPGA	-	Field Programmable Gate Array
fps	-	Frames Per Second
G	-	Generic Green's Function

GPU	-	Graphics Processing Unit
H^+	-	Positive Hydrogen Ion
i	-	Unit imaginary number $\equiv \sqrt{-1}$
I	-	Intensity
$\widetilde{I}$	-	Contrast Hologram Intensity $\equiv I - U_{reference}^2$
k	-	Wavenumber $\equiv 2\pi/\lambda$
$\hat{\mathbf{k}}$	-	Unit normal in +z direction
KF	-	Kirchhoff-Fresnel
λ	-	Wavelength of light
LED	-	Light Emitting Diode
MIMD	-	Multiple Instruction Multiple Data
MnS	-	Manganese Sulphide
Mo	-	Molybdenum
Mpixel	-	Megapixel
n_1	-	Index of refraction 1
n_2	-	Index of refraction 2
NA	-	Numerical Aperture
NaCl	-	Sodium Chloride (Salt)
Ω	-	Resistance, measured in Ohms
$\mathbf{P}$	-	An arbitrary point in space
PCSA	-	Polarizer, $\frac{1}{4}$ wavelength Compensator, Sample, Analyzing polarizer
π	-	3.14159265...
ψ	-	The portion of the obliquity factor that can change between the Kirchhoff-Fresnel and Rayleigh-Sommerfeld diffraction integrals
$\mathbf{r}$	-	Vector originating at the point source of light
$\mathbf{r}_2$	-	Vector to a point on the aperture originating at point P
RS	-	Rayleigh-Sommerfeld

S	-	Sulphur
SEM	-	Scanning Electron Microscopy
Σ	-	Aperture or Recording Screen
SIMD	-	Single Instruction Multiple Data
SS 316LVM	-	Stainless Steel 316 Low carbon Vacuum Melt
SS 316L	-	Stainless Steel 316 Low carbon
θ_B	-	Brewster Angle
UV	-	Ultraviolet
U	-	Complex wavefront
U'	-	Complex wavefront at the aperture plane
ξ	-	Vector from point source to a point on the camera sensor
*	-	Denotes complex conjugate is to be used

Acknowledgements

I would like to thank my supervisor, Harm Rotermund, for the opportunity to work on these projects, for his encouragement throughout, and for the freedom to investigate various aspects of holography in detail. I would also like to thank Jürgen Kreuzer, Stefan Jericho, and Manfred Jericho for initially introducing me to the field of DIHM, and for the many discussions we've had since then. Jorge Garcia-Sucerquia was also a good mentor regarding digital holographic microscopy. Meike Rotermund has been a wonderful assistant for experimental work these last few years, and Nathan Musoke has been a very good addition for holography and corrosion studies this year, too. Their combined effort in editing has also helped to make the introduction and conclusion sections much more readable. I want to acknowledge Zhijun Bai for the initial idea to treat SS 316LVM with nanopure water, and Matthew Lobban for his preliminary experimental work. All of my lab-mates have been helpful throughout the years, willing to lend a hand when needed. I would also like to thank the technical staff (Robbie Sanderson, Andy George, Willi Krauss, John Noddin, Kevin Borgel, Alex Feargrieve, and Simon Trussler) who have helped translate my ideas into functioning devices, without which the experimental work could not have been completed.

All of the people in the department have been wonderful and have helped to make this a nice place to work, but I would especially like to thank Parisa Sadeghi, Markus Karahka, Simon de Vet, and Aaron van Donkelaar for their friendship, encouragement, support, and helpful discussions throughout this PhD. They have helped me keep perspective and have changed how I look at the world around me. I would also like to thank my family, who have continuously loved and supported me throughout all of my studies.

Chapter 1

Introduction

Stainless steels have been engineered to resist general corrosion for the bulk of the iron alloy, yet they are still susceptible to localized forms of corrosion. Local corrosion types include pitting and crevice corrosion, which leave only microscopic marks on the surface yet can hide larger-scale subsurface corrosion. This corrosion can cause health concerns in relation to corrosion products from biological implants, or can reduce structural integrity and lead to catastrophic failure in industrial settings.

To prevent stable, or long lived corrosion, a thorough understanding of the mechanisms and interactions between pitting sites at early stages of development is required. Optical techniques provide non-destructive methods to investigate different aspects of metastable pitting, and using multiple techniques simultaneously allows one to probe multiple aspects simultaneously.

This body of work is composed of three interrelated projects, developed simultaneously and used to study metastable pitting *in situ* and to help prevent pitting corrosion on stainless steel 316LVM in saline solutions. The results of each project have been submitted to peer-reviewed journals; these articles each form a chapter of this thesis, with additional information and general introductions provided in this chapter. The first project is primarily concerned with the development of three simultaneous *in situ* optical techniques used to gain additional information about metastable pitting. The techniques used include digital in-line holography for microscopic volume imaging of the solution, ellipsomicroscopy for surface imaging to observe nanometer-sized changes in the thickness of the passive layer, and microscopy to observe pitting on the surface of the electrode as it occurs. For digital in-line holographic microscopy, new parallel programming methods that leverage the power of Graphics Processing Units

(GPUs) were adopted to allow more than 10 reconstructions per second using an approximate method, and 1 reconstruction in 17 s with sub-wavelength lateral resolution using approximations only in a minor weighting factor. The second project describes a simple method to treat stainless steel that increases its resistance to corrosion in NaCl solutions. The optical techniques described in the first part were used to verify that corrosion occurs only on the polished surface (pitting corrosion) and not between the insulating coating and the wire (crevice corrosion), and used scanning electron microscopy and energy dispersive X-ray spectroscopy for compositional determinations of the stainless steel. The third project explores the numerical methods used for reconstructing holograms using the full Kirchhoff-Fresnel or Rayleigh-Sommerfeld integrals, and shows how interleaved reconstructions made with the convolution method can give more accurate results than well established approximate methods and in reasonable time frames. Since researching holographic reconstruction methods was the second largest project and since the paper specifically about holographic reconstructions was quite succinct, the largest portion of this introductory chapter is spent on the development of digital holographic reconstruction methods.

These three projects demonstrate the power and usefulness of the simultaneous *in situ* optical techniques in studying metastable pitting corrosion, show a simple surface treatment which improves pitting resistance in saline solutions, and demonstrate GPU based methods to reconstruct holograms with increased speed or accuracy over older methods. While these projects were successful in and of themselves, they also serve as starting points for new investigations into pitting corrosion and in digital holographic microscopy, including off-line holography.

1.1 Simultaneous *In Situ* Imaging Methods

1.1.1 Historical Perspective on Stainless Steels

Stainless steel, the third most widely used metal after aluminum and steel [1], was invented approximately 100 years ago, though it had nearly been discovered almost a century earlier than that. Pierre Berthier experimented with iron alloy compositions in 1821 following experiments conducted by Faraday and Stodart a year earlier, and while the alloys he produced contained high percentages of chromium, the carbon content was too high for them to resist oxidation [1,2]. Misunderstandings at that time about how corrosion should be tested led people to believe that chromium was actually detrimental to corrosion resistance, so it was not until the negative effects of carbon on the corrosion resistance of iron alloys were understood that stainless steel alloys were finally developed. In 1911, Philipp Monnartz published an article (in German) that identified the key aspects that determined the corrosion resistance of stainless steel and paved the way for further developments [1–3]. Industrial developments of stainless steel occurred simultaneously in France, Germany, England, and the United States starting in 1912. Today, there are hundreds of commercially available stainless steel alloys and uses range from nuclear reactors to industrial reaction vessels to building materials to medical implants to kitchenware and more.

The corrosion resistance of stainless steel can be attributed to the chromium content (at least 11 %) of the iron alloy. The chromium creates a thin protective oxide/hydroxide film (on the order of nm thick [2, 4, 5]) at the surface, which protects the bulk of the alloy from corrosive attacks and will 'heal' itself when it is damaged; the passive film spontaneously re-forms in most environments. Different alloy mixes have been developed for a variety of applications and while stainless steel resists general corrosion, it is still susceptible to localized corrosion. Inclusions, scratches, and defects in the passive oxide layer can all lead to microscopic localized corrosion in the form of crevice and pitting corrosion. If the passive film is able to reform in the early stages of development then these microscopic pits are more or less harmless.

If, however, the passive protective layer is unable to reform, then the microscopic metastable pitting can transition to stable pitting. Pitting corrosion is difficult to detect, and can cause health and safety concerns with regard to medical and dental implants, or can lead to catastrophic failure in industrial applications.

Attempts to understand how and where pitting events initiate have been made over the last half-century in an effort to create alloys that are more corrosion resistant [4, 6–9]. It has been found that pitting corrosion occurs in the presence of anionic species and chloride rich environments are particularly aggressive toward stainless steels [4]. If carbon concentrations are higher than 0.1 %, it can collect and combine with chromium at grain boundaries in stainless steels to deplete chromium and reduce its corrosion resistance [2]. However, in low carbon stainless steels, it has been shown that sulphide inclusions, and MnS in particular [4, 9–12], are important sites for pit nucleation. There has not been agreement about the mechanisms involved [13–15], though recent discoveries of FeS at the edges of MnS inclusions by Williams *et al.* [16] could perhaps explain the initiation mechanisms.

Initial pitting corrosion sites appear to be random in position and time; however, they are dependent on the passive film that protects the metal against corrosion. A pitting event initiates at a flaw in the passive layer, and the dissolution of an inclusion or the attack on the metal is shown by an increase in anodic current. It is thought that initial pitting sites are aided by protective covers (salt films or the oxide layer itself [16–19]), which limit transport and mixing with the environment and allow the pit to grow with a constant current. The solution inside the pit becomes increasingly aggressive in an autocatalytic cycle: metal dissolution in the oxygen depleted solution produces H^+, which draws in Cl^-, which then acts to further attack the metal. As more openings in the cover are created or existing openings get larger, the anodic current will rise quickly as mixing occurs. If the pit stability product (current $\times$ pit depth) is sufficiently large (> 0.3 A m^{-1}) then when the protective cover is removed the depth of the pit is sufficient to limit diffusion of ions and the pit will continue to grow; this type of pit is considered a stable pit [20]. Below this critical stability

product, additional physical barriers to diffusion are required for sustained pit growth. When the pit cover is removed the pit will repassivate; these events are referred to as metastable pitting events and they last several seconds. Figure 1.1 shows a cartoon of the development cycle of a metastable pit.
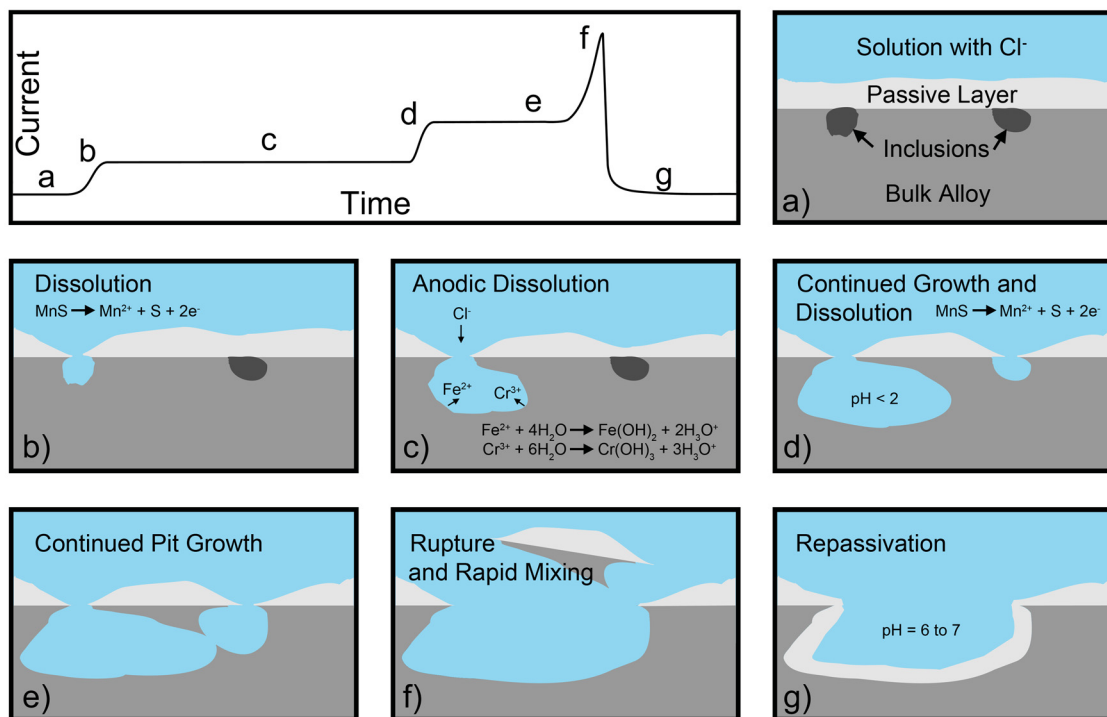
Figure 1.1: A plot showing the anodic current as a function of time for the development cycle of a metastable pit. In (a) two inclusions can be seen below the passive layer in the bulk of the alloy. In (b) the passive layer weakens enough at the one inclusion that the inclusion can dissolve. There is a corresponding increase in anodic current. In (c) the pit grows protected by the passive layer and the anodic current remains roughly constant. In (d) the other inclusion dissolves, increasing the anodic current again. In (e) both pits develop with constant current until (f) when the cover breaks off and there is a sharp increase in anodic current. In (g) the pit is not large enough to persist without the cover, so it repassivates and the anodic current drops to zero amperes. Images based on theory by Pistorius and Burstein [20], with chemical equations from [4, 12, 21, 22].

Theories, models, and experiments about the cooperative behaviour of metastable pits that can lead to stable pitting have been made [23–28], and it was this body of

work which led to the development of simultaneous *in situ* Ellipsomicroscopy for Surface Imaging (EMSI) and contrast enhanced microscopy at the Fritz-Haber-Institute in Berlin [29, 30]. The main idea is that if aggressive species are released when pitting occurs, then they can affect and weaken the passive layer in the surrounding region, which exposes new pit initiation sites (such as sulphide inclusions), producing a cycle that can repeat. Thus, more and more metastable pits should occur in a localized region, and while none of these metastable events might be significant enough to transition to stability on their own, as a group they might create favourable local conditions to allow the creation of a stable pit. Work by Budiansky, Hudson and Scully [31] has shown that solution effects exist by using arrays of microelectrodes and observing pitting events temporally correlated in neighbouring electrodes.

1.1.2 *In Situ* Imaging Motivations

To better see the spatiotemporal relationships between pitting events, our surface imaging group was approached. The group's experience with EMSI [32–37], based on a light polarization technique that is sensitive to changes in oxide layer thicknesses on the order of nanometers, would allow qualitative investigations into the changes of the passive layer. Quantitative measurements of the passive layer require precise modelling of the entire optical system; any mistaken assumptions, including assumptions about the surface roughness, render quantitative ellipsometric data incorrect. EMSI, which uses a PCSA arrangement (Polarizer, $\frac{1}{4}$ wavelength Compenstator, Sample, Analyzing polarizer), is aligned to an almost null-image orientation and is sensitive to changes in the passive layer. These changes will appear as variations in the recorded intensity since the polarization of the light will be modified and the nulling criteria will no longer be fulfilled. The illumination angle is approximately the Brewster angle, θ_B:

$$\tan(\theta_B) \quad = \quad \frac{n_2}{n_1} \tag{1.1}$$

where n_2 is the index of refraction for the oxide being investigated and n_1 is the index of refraction for the medium before it (in our case, the NaCl solution). Using $n_2 = 2.54$ for Cr_2O_3 [38], and $n_1 = 1.332$ for the NaCl solution [39], the Brewster angle is 62.5°. The imaging setup is also arranged to best fulfil the Scheimpflug principle [40][1] for the geometrical magnification required. The Scheimpflug principle can be verified with the thin lens equation and states that a planar object tilted with respect to the lens plane can be imaged entirely in focus by tilting the imaging sensor such that the imaging plane, lens plane, and object plane all intersect in a line. The single orientation qualitative ellipsometric imaging technique has lower lateral resolution (~ 10 μm) than an ordinary long working distance diffraction limited microscope (~ 1.5 μm), but is limited temporally only by the camera used to acquire the images.

Dornhege (née Bölscher), Punckt, *et al.* [29, 30] obtained simultaneous *in situ* videos using EMSI and high resolution microscopy to observe spatiotemporal relationships between metastable pits. They observed wavefronts of changes in the passive layer which preceded clusters of pitting events, and noted the ejection of particles from the metal surface into the solution during some pitting events. The limited depth of field associated with the microscopic techniques precluded any analysis of these particles, but created the question of whether there would be a way to analyze their trajectories in 3D.

Digital In-line Holographic Microscopy (DIHM) was proposed as a possible technique to gain volume imaging capabilities with lateral resolution on the order of 2 μm while retaining the already successful simultaneous *in situ* EMSI and microscopy. Phase objects and changes in index of refraction can also be analyzed [42], so using this diffraction based technique would also yield direct information about the local changes in concentrations associated with pitting events. Prior to this PhD work, the computation time for a single reconstruction of the complex wavefront at a plane

---

[1]In Theodor Scheimpflug's 1904 patent he refers to and acknowledges Carpentier's patent of 1901 [41], but says that the results of the prior patent are limited in scope. Carpentier's patent, however, also states that the lens plane, image plane, and object plane must intersect in a line for the entire image plane to be in focus.

between the light source and recording plane was approximately 1 s using multiple CPUs, so an additional goal was to create a way to compute reconstructions in 'real-time'. Here we define 'real-time' as a minimum of 10 reconstructions per second and/or reconstructions as fast as the digital camera could acquire images. Both aspects, the addition of DIHM and the high speed reconstructions, presented significant technical challenges and their development constituted the bulk of the work for this PhD.

1.1.3 Apparatus Modifications

Modifications of the glass cuvettes used to hold the saline solutions for electrochemical experiments were necessary to allow the addition of DIHM. The cuvettes used in Germany were large and made of flat pieces of glass glued together so that they were perpendicular to the optical paths for EMSI and microscopy. Seams were heavily glued to prevent leakage and there was no need to worry about the physical height of the glass pieces. Introducing simultaneous DIHM necessitated the miniaturization of the cuvettes (see Figure 1.2) with height $\sim$ 1 cm. This cuvette size would allow $\sim$ 2 μm lateral resolution in reconstructions for the volume of the solution nearest the stainless steel wire samples being tested. To ensure clear optical paths for holography, microscopy and EMSI, only minimal amounts of glue could be used at the seams, so cuvettes built from 4 separate pieces of glass on a coverslip were fragile. Willi Krauss suggested that we bend the glass pieces instead of gluing, so we carefully shaped fire-block moulds that Andy George used to bend the glass pieces into shape (see Figure 1.3). After bending, stresses were introduced into the glass which would affect the polarization of light; to relieve stresses the glass was annealed by heating the glass at 3 °C/min to 500 °C, holding the temperature for $\sim$ 5 h, then cooling the glass at a rate of 3 °C/min. Cross polarization techniques were used to verify that the stresses were relieved (see Figure 1.4). After bending the glass, the edges had to be polished to make them flat for gluing. Norland Optical Adhesive 61, which cures in UV light and is resistant to most solvents, was used to join the cuvette pieces together. After

attaching the back face of the custom cuvette, the top edge had to be repolished so that it would be possible to affix a lid.
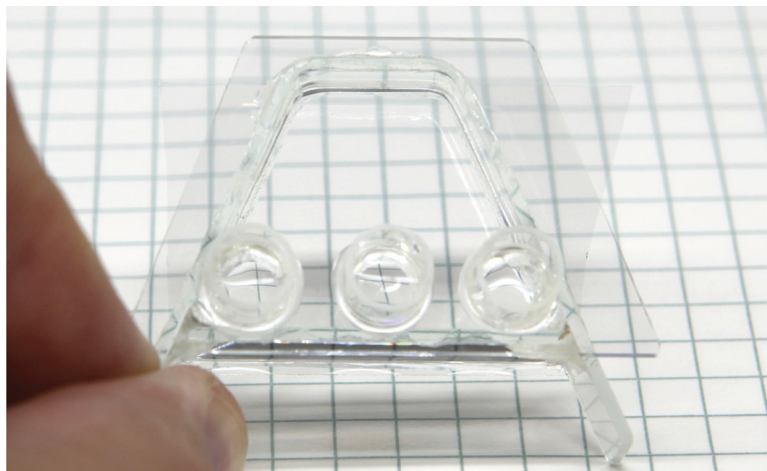
Figure 1.2: A photo of the finished cuvette. The back face of the trapezoid measures 30 mm, the front face is 11 mm, and the distance from the front face to the back face is 20 mm. This creates a total surface area for the trapezoid of 410 mm^2. The height of the cuvette is 11.37 mm including the glass lid and base. The glass thickness for the side walls is 1.06 mm, for the lid is 1.08 mm, and for the base is 0.15 mm.

The optical arrangement also needed to be modified to allow the addition of DIHM. The point source of light used in the holographic setup is located below the cuvette, and the camera is above the cuvette looking downward. The entire apparatus had to be raised, to give room for the microscope objective and the 3-axis X-Y-Z stage used to position the 0.5 - 0.7 μm pinhole. Spatial constraints required us to move the laser away from the objective and necessitated the use of a 45° mirror beneath the objective. The distance between the laser source and the objective proved fortuitous, since the Zeiss objective we use to focus the light through the pinhole is an epiplan objective; episcopic objectives are designed to observe reflected light from objects using the light that enters the back of the objective. By creating a screen with a hole in it to allow the laser beam to illuminate the objective unobscured, we were able to image what the objective was pointed at. This method makes the alignment of pinholes trivial if there are features that can be observed on the pinhole support disk, such as concentric circles where the molydenum was thinned out (Norsam Technologies pinholes), or a

Figure 1.3: A photo of the glass being bent for the cuvette using a hydrogen-oxygen flame.

small groove etched in nickel (National Aperture pinholes).

1.1.4 Additional Programming

As well as modifying the setups, additional software had to be created to integrate all of the data into a visual record of the experiment. Holograms are acquired as still images, and while the file names had time stamps included in them, there is no guarantee of consistent spacing in time. Frames are simply acquired as quickly as the computer system allows. A camera flash is used to synchronize the holograms to the other microscopic techniques; the flash generally appears in just one acquired frame. This frame becomes frame 0 in the sequence, and a custom program processes a copy
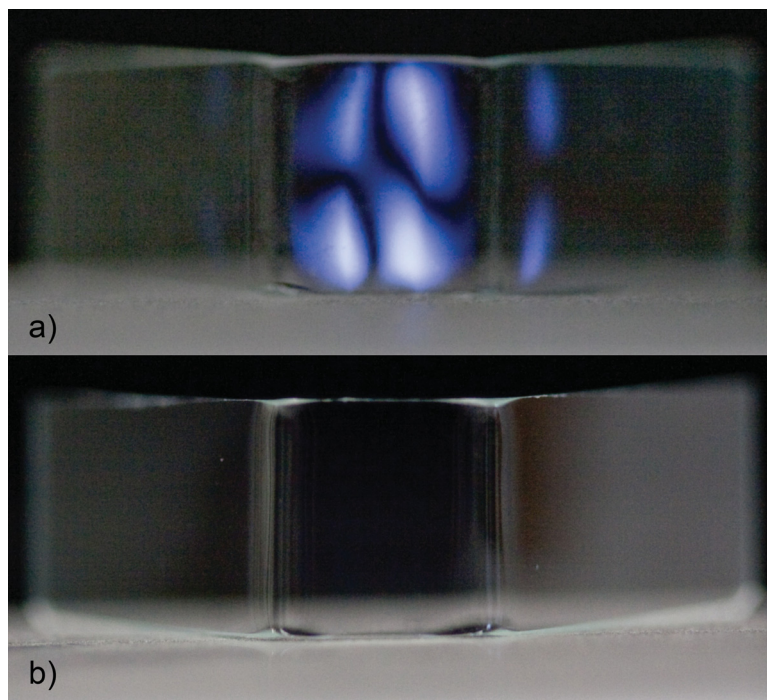
Figure 1.4: Cross-polarization photos showing: (a) the stresses in the glass before annealing, and (b) how the stresses have been relieved after annealing.

of the original hologram sequence so that there will be 25 evenly spaced frames per second (fps) to include in the movie. The data from the potentiostat are saved as text files for the potential and current, so a program was written to plot the data as linear potential versus time and either linear or semilog (log-lin) plots of current versus time. To synchronize the start time of the sequence of plots of potentiostat data with the 3 microscopic techniques, a photodetector was used to detect a camera flash. This photodectector was attached to the same analogue to digital converter as the potentiostat so a third text file of data allowed time synchronization of the different feeds to be done. Apple Quicktime was used to turn sequences of images into movies and Final Cut Express was used to create the combined data movies. While an experiment would take between 20 - 40 minutes to perform, the setup (including alignment, cleaning, and sample preparation) and the subsequent processing of the data sets to combine them into a single movie would each take days.

1.1.5 Experiments and Introduction to the First Paper

Initial experiments were conducted in cuvettes without lids, which gave inaccurate distance results for DIHM because of the meniscus at the top of the cuvette, or with a coverslide sitting loosely at the top, which often resulted in saltwater dripping onto the pinhole. These experiments showed that the 3 simultaneous *in situ* optical techniques could be used together, but did not yield useful holographic data. Lids were developed to alleviate these problems, with the requirements that the cuvette must be completely fillable to the base of the lid and wires must be free to move for adjustment with the 3-axis manipulator. The final version was fabricated from a glass slide (1 mm thick) with holes drilled through it for access, and cylindrical glass tubes glued on top above the holes. These lids could be temporarily attached to the cuvettes using rubber cement. Sealed cuvettes created a well-defined optical path for holography, prevented leaks and subsequent pinhole destruction, and reduced problems with evaporation, which was noticeable in dry winter weather. Without lids the evaporation rate of water from the cuvettes in winter was, on average, 30 μg/s, based on measurements over a couple of weeks (relative humidity $\sim$ 15 %). With a precision electronic semi-balance (Sartorius R 160 P), this change in mass due to evaporation was directly observable.

5 μm beads were added to the saltwater solution to see if flows related to the positions of the electrodes could be detected. However, it was observed that whenever the EMSI laser was turned on, the dominant effect was that the beads would move upwards through the cuvette[2]. It is thought that absorption of light at the surface of the working electrode, based on the angles used for EMSI, caused local heating which would drive convection cells. When large pitting events occurred, lensing effects caused by local changes in concentration modified the light interaction with the wire

---

[2]Video Clip 1.1 (File: NeutralDensityFilterTest.mov Duration: 3 min 19 s) is a movie demonstrating the effect of the HeNe laser used in an EMSI configuration on the flow pattern of the 5 μm beads. When a neutral density filter (0.0005 transmission) is used, the amount of energy at the wire face is on the order of μW.

face and the bead paths changed, almost circling the pits[3]. Tests, in which the microscope was refocused at different distances from the wire face, demonstrated that upward bead movement was limited to the region in closest proximity to the wire face. The heating effect was minimized by putting a neutral density filter on the HeNe laser. Flow paths related to electrode positions were not detected and since beads would obscure the ability to detect small changes in index of refraction associated with metastable pitting events, beads were not used in subsequent experiments.

The sensitivity to changes in the index of refraction, as well as the observation, tracking, and attempts to identify the composition of material ejected from the wire face make up the bulk of the work presented in the paper that was submitted to Corrosion Science (Chapter 2). In it we show that DIHM is sensitive to pitting events with anodic currents on the order of 10 nA and demonstrate simultaneous usage of all three *in situ* optical methods for metastable pit analysis, a definite first. DIHM also allows one to investigate phase changes, much like a phase contrast microscope, but with less limitations since it can be 'refocused' computationally. Interference patterns show phase changes as large as 3π rad, which correspond to an average increase in the index of refraction of $\Delta n = 0.015 \pm 0.005$. If this is caused by increased local concentrations then the enhancement would be on the order of one magnitude compared to the bulk solution [39]. While this seems high, larger concentration enhancements in the pits (between 5 and 24 $\times$ the bulk concentration), measured by flash freezing the solution and then analyzing the relevant portion analytically, have been reported [21].

Closely related to, but additional to the work presented in the article submitted to Corrosion Science, the motion of particles ejected from the large pits (and tracked with DIHM) and the plume shapes (indicated by zones with changes in the index

---

[3]Video Clip 1.2 (File: BeadPathMay3_2010-30s.mov Duration: 30 s) is a movie showing how large pitting events affect the paths of 5 μm beads. While the potential is high, the large pit causes changes in the index of refraction such that light is bent into the geometric shadow of the wire. The bead paths get changed by the active pits. When the potentiostat is set to the initial potential, the anodic current immediately drops and the effects on the bead paths stop.

of refraction) can be understood by analyzing particle motion in low Reynolds number regimes. At low Reynolds numbers, such as for particles on the order of 1 μm (ejected materials observed with the optical microscope) or on the order of angstroms or nanometres (ions or polyatomic ions), particle motion is dictated only by the forces currently acting on them [43]. A competition between Brownian motion and sedimentation will occur: the diffusion coefficient is inversely proportional to the effective radius of the particle, while the terminal velocity is proportional to the square of the effective radius and the difference in its density from the density of the solution. This implies that movement associated with Brownian motion will be negligible for particles with effective radii on the order of 2 μm, and that sedimentation rates should be on the order of 70 μm/s (measured velocities were $\sim$ 100 μm/s). On the other hand, for ions or polyatomic ions in the Angstrom to nanometer size range, sedimentation will be negligible and diffusion associated with Brownian motion will dominate unless other forces are present. For ions or polyatomic ions associated with a metastable pitting event lasting 5 s, diffusion should yield an average distance travelled on the order of 50 to 150 μm. The width of the 'plumes' originating at the pitting sites correspond well with these distances associated with diffusion ($\sim$ 70 μm), but the length of the plumes are already $>$ 300 μm approximately 2 s into the pitting events. This implies that additional forces are present, and since the plumes consistently appear to be perpendicular to the wire face, electric field effects on ions seem like a probable cause for the plumes.

The novel aspect of adding DIHM for electrochemical analysis of the solution at the electrode/solution interface was at first thought to be diminished when a set of papers from one group were found [44–48]. However, their digital work is interferometric in nature rather than holographic despite the article titles. In addition, there is no clear evidence that they reconstruct the complex wave at different planes to obtain 3D information about the changes in the index of refraction in the solution, and their film-based techniques use holographic interferometry [49, 50]. Thus, the implementation of DIHM by itself would still be novel and our simultaneous use of

the three complementary optical techniques is even more unique.

1.2 Surface Treatments for Increased Pitting Resistance and Introduction to the Second Paper

In an effort to reduce pitting and intergranular corrosion, many stainless steel surface modification techniques have been investigated. These techniques include high current pulsed electron beams [51, 52], laser resurfacing [10, 53], and chemical surface treatments [54, 55]. Zhijun Bai, a post-doctoral researcher here, and Matthew Lobban, an honours student in the group, also investigated various chemical surface treatments of SS 316LVM in an effort to enhance pitting corrosion resistance in biological solutions. One of their surface treatments included sample immersion in 90 °C nanopure water immediately after polishing the sample. Their studies showed improved pitting resistance, but they were unsure if it was caused by the treatment or if the epoxy that the samples were embedded in had melted and coated the sample. As the focus of the second project, investigations were repeated with uncoated wires using *in situ* imaging techniques. Scanning Electron Microscopy (SEM) and Energy Dispersive X-ray Spectroscopy (EDS) were also performed before and after the water treatments to observe any compositional changes caused by the treatments. It was found that MnS inclusions were removed from the surface of SS 316L samples during the water treatments, which led us to believe that there was a correlation between the improved pitting resistance in a Cl^- environment and the removal of potential pitting sites. An Arrhenius relationship for the dissolution reaction rate and a low solubility of MnS in water would explain why 90 °C water and durations of 2 h or longer appear are required for significant pitting corrosion enhancement. These studies are presented in the paper reprinted from Electrochemistry Communications in Chapter 3.

1.3 The Kirchhoff-Fresnel Diffraction Integral and Holographic Reconstructions

1.3.1 Simplification of the Kirchhoff-Fresnel Diffraction Integral

The Kirchhoff-Fresnel (also called the Kirchhoff-Helmholtz) diffraction integral provides a firm mathematical basis for the phase and amplitude terms that were assumed to hold true for secondary waves in the Huygens-Fresnel theory of the propagation of light. It relates the complex wavefront at the volume surface to the distribution of light sources within the volume and is also used to solve diffraction problems for coherent monochromatic light. To develop a method to reconstruct holograms numerically, we start with a general solution for the diffraction of light from an aperture in a screen. The solution as derived in Fourier Optics [56] and Principles of Optics [57] is:

$$U(\mathbf{P}) = \frac{1}{4\pi} \int \int_{\Sigma} \frac{\partial U}{\partial n} G - U \frac{\partial G}{\partial n} ds \tag{1.2}$$

where $U(\mathbf{P})$ is the complex wave at a point on the opposite side of the screen with the aperture, Σ indicates that the region of interest is the aperture alone, $\frac{\partial U}{\partial n}$ is the partial derivative of the wave at points on the aperture with respect to the normal of the aperture, G is a Green's function, U is the complex wave at a point on the aperture, and $\frac{\partial G}{\partial n}$ is the partial derivative of the Green's function with respect to the normal of the aperture. The solution presented in Equation 1.2 was already simplified in that the surface that the volume was integrated over was carefully chosen so that all contributions that were not from the aperture opening equalled zero. A diagram showing the geometry used for this setup is shown in Figure 1.5.

The wave function at the aperture is defined as:

$$U(\mathbf{r}) = A_{ref} \frac{\exp(ik|\mathbf{r}|)}{|\mathbf{r}|} \tag{1.3}$$

where $\mathbf{r}$ is the vector from the source of light to a point on the aperture, A_{ref} is the amplitude of the reference wave, and $k \equiv 2\pi/\lambda$ where λ is the wavelength of the light.
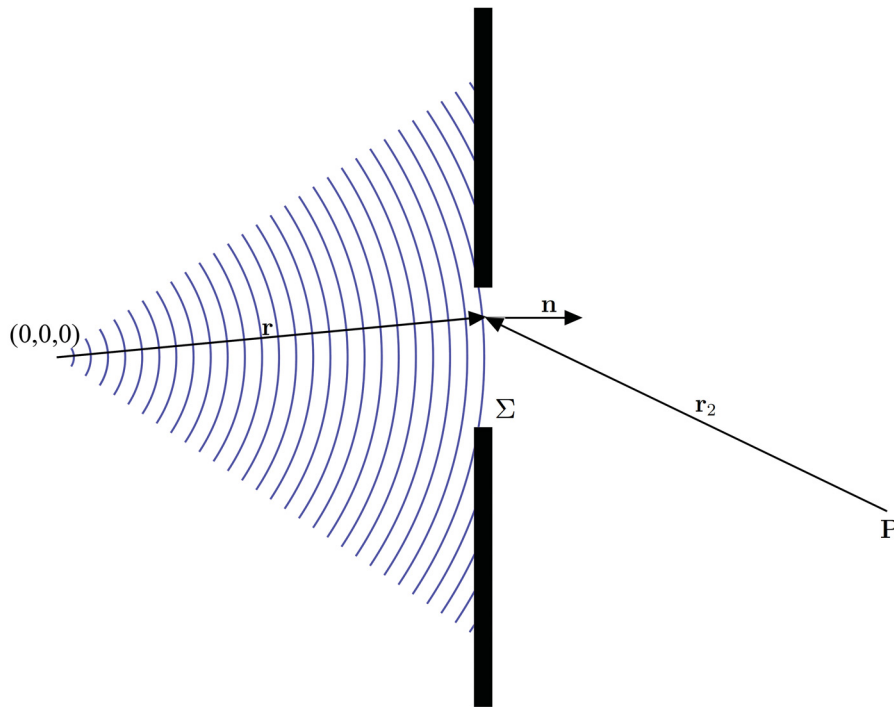
Figure 1.5: A diagram of the configuration used when discussing diffraction of point source monochromatic light from an aperture at a point, P.

Thus,

$$
\begin{aligned}
\frac{\partial U}{\partial n} &= ikA_{ref}\frac{\exp(ik|\mathbf{r}|)}{|\mathbf{r}|}\frac{\partial \mathbf{r}}{\partial n} - \frac{1}{|\mathbf{r}|}A_{ref}\frac{\exp(ik|\mathbf{r}|)}{|\mathbf{r}|}\frac{\partial \mathbf{r}}{\partial n} \\
&= ikA_{ref}\frac{\exp(ik|\mathbf{r}|)}{|\mathbf{r}|}\cos(\mathbf{r},\mathbf{n}) - \frac{1}{|\mathbf{r}|}A_{ref}\frac{\exp(ik|\mathbf{r}|)}{|\mathbf{r}|}\cos(\mathbf{r},\mathbf{n}) \\
&= \left(ik - \frac{1}{|\mathbf{r}|}\right)\cos(\mathbf{r},\mathbf{n})\left[A_{ref}\frac{\exp(ik|\mathbf{r}|)}{|\mathbf{r}|}\right] \\
&= \left(ik - \frac{1}{|\mathbf{r}|}\right)\cos(\mathbf{r},\mathbf{n})U
\end{aligned}
\tag{1.4}
$$

If $|\mathbf{r}| \gg \lambda$ then this reduces to

$$
\frac{\partial U}{\partial n} = ik\cos(\mathbf{r},\mathbf{n})U
\tag{1.5}
$$

In the case of the Kirchhoff-Fresnel solution, the Green's function, G, is chosen as

$$
G = \frac{\exp(ik|\mathbf{r}_2|)}{|\mathbf{r}_2|}
\tag{1.6}
$$

where G is a diverging spherical wave, like the original source, only with its origin at the test point, $\mathbf{P}$. Since its form is almost identical to U, the partial derivative with respect to normals at the screen is

$$\frac{\partial G}{\partial n} = ik\cos(\mathbf{r}_2, \mathbf{n})G \tag{1.7}$$

Combining 1.5 and 1.7 into 1.2 we obtain

$$
\begin{aligned}
U(\mathbf{P}) &= \frac{ik}{4\pi} \int\int_\Sigma A_{ref} \frac{\exp(ik|\mathbf{r}|)}{|\mathbf{r}|} \frac{\exp(ik|\mathbf{r}_2|)}{|\mathbf{r}_2|}[\cos(\mathbf{r}, \mathbf{n}) - \cos(\mathbf{r}_2, \mathbf{n})]ds \\
&= \frac{i}{\lambda} \int\int_\Sigma A_{ref} \frac{\exp(ik|\mathbf{r}|)}{|\mathbf{r}|} \frac{\exp(ik|\mathbf{r}_2|)}{|\mathbf{r}_2|} \frac{[\cos(\mathbf{r}, \mathbf{n}) - \cos(\mathbf{r}_2, \mathbf{n})]}{2}ds
\end{aligned} \tag{1.8}
$$

where the last term actually adds two values together because the origins of the vectors $\mathbf{r}$ and $\mathbf{r}_2$ are on opposite sides of the aperture.

Writing the wavefront at the aperture plane as

$$U' = \frac{i}{\lambda} A_{ref} \frac{\exp(ik|\mathbf{r}|)}{|\mathbf{r}|} \frac{[\cos(\mathbf{r}, \mathbf{n}) - \cos(\mathbf{r}_2, \mathbf{n})]}{2} \tag{1.9}$$

we see that it matches the form initially used by Fresnel to describe the secondary wavefronts, and it does so without making assumptions about how the phases must change for these secondary points. Equation 1.8 can also be rewritten using U'

$$U(\mathbf{P}) = \int\int_\Sigma U' \frac{\exp(ik|\mathbf{r}_2|)}{|\mathbf{r}_2|}ds \tag{1.10}$$

to emphasize the fact that knowing the complex wavefront at all of the points across the aperture plane is equivalent to knowing where the source was located in order to calculate the diffraction at point $\mathbf{P}$. This can be further generalized: if we know the complex wavefront at the aperture plane, then we have information about the entire volume before it, and we can also propagate the wavefront beyond the aperture plane.[4] It is this result that we employ in holography; however, it is difficult to obtain the complex wave correctly since the frequency of light is on the order of 10^{14} Hz.

---

[4]For a discussion about the Rayleigh-Sommerfeld diffraction integral and how it compares/differs from the Kirchhoff-Fresnel result presented here, please refer to Appendix A

1.3.2 Holography

Dennis Gabor had the insight that a complex wave can be recorded and then recovered using the intensity of the light alone if the complex wave is made to interfere with a well-defined coherent reference wave [58–63].[5] The recorded intensity takes the form

$$I = U^2_{reference} + U^*_{reference}U_{scatter} + U_{reference}U^*_{scatter} + U^2_{scatter} \qquad (1.11)$$

where $U_{reference}$ designates the complex wave associated with the well-defined coherent reference, $U_{scatter}$ designates the complex waves associated with light that scatters from objects, and $*$ denotes that the complex conjugate is used. If objects are small and scattering is weak, then the effects of the fourth term are negligible. The first term is the intensity pattern of the reference wave alone and the second and third terms correspond to waves proportional to the real and conjugate (or twin) objects, respectively.

Gabor introduced holography before lasers were invented so his light sources were limited to short coherence lengths; the only configuration available to him was in-line holography. The twin, according to Born and Wolf [57] in this configuration appears to originate from a fictitious object (the image of the true object in a spherical mirror) located symmetrically with the real object across the source of light. The irradiance from this twin at any point in the plane of the object is inversely proportional to the square of the distance from the twin to the object plane, so the effects of the twin image on reconstructions decrease as the point source to object distance increases.

Our group also uses the in-line configuration, but we now have lasers (Toptica iPulse 406 nm) and use digital sensors (Toshiba-Teli CSB4000F-10) rather than photographic emulsions to capture holograms. Aside from reduced material costs and chemical development time, digital holography allows us to remove the effects of the reference wave from the captured intensity (by pairing holograms from a sequential time series of holograms, or by recording a separate reference hologram). This modified intensity is referred to as a contrast hologram and is denoted by $\widetilde{I}$.

---

[5]He was awarded the Nobel prize in physics for his work in 1971 [64].

We build off of the techniques developed and refined by Dr Kreuzer, Dr Jericho, and their colleagues over the years [65–79]. One of the goals in this project was to develop real-time reconstruction capabilities: as previously stated, we define real-time reconstruction rates as > 10 reconstructions per second and/or reconstructions as fast as holograms can be acquired. At full resolution, 4 Mpixel holograms are acquired at a rate of 7 fps, so reconstructions need only be reconstructed at 7 fps without creating system lag and slowing acquisition rates. To achieve these rates, an approximate version of Equation 1.10 must be used; the following section discusses the possible methods that can be used.

1.4   Comparison of Diffraction Integral Approximations

For numerical holographic reconstruction algorithms Equation 1.10 is the starting point, however, the notation often gets changed slightly. Figure 1.6 shows the configuration used and the coordinates that are adopted. Note that the camera sensor takes the place of the aperture in Figure 1.5 since the complex wavefront can be recreated there using the interference pattern and *a priori* knowledge of the reference wave. If the original positions of the scatterers between the source and the sensor are to be determined, then the complex wave at the once-aperture-now-sensor plane, U', is computed by multiplying either the interference pattern, I, or the contrast hologram, $\widetilde{I}$, with the complex conjugate of the reference wave. This is like interfering a collapsing spherical wave with the hologram to determine the real positions of the objects. If, on the other hand, the original forward propagating wavefront at the sensor plane is desired, the interference pattern should be multiplied by the original complex reference wave. However, the numerical equivalent of a lens setup is required to 'focus' the light to create images at different planes beyond the sensor. In this treatment, the real positions of the scattering objects are desired, so using the conjugate form of

a point source reference wave, Equation 1.10 becomes

$$U(\mathbf{r}) = \frac{i}{\lambda} \int \int_{\Sigma} I(\boldsymbol{\xi}) \underbrace{\frac{\exp\left(-ik|\boldsymbol{\xi}|\right)}{|\boldsymbol{\xi}|} \overbrace{\left[\frac{\cos(\boldsymbol{\xi} - \mathbf{r}, \mathbf{n}) + \cos(\boldsymbol{\xi}, \mathbf{n})}{2}\right]}^{\text{obliquity factor}} \frac{\exp\left(ik|\boldsymbol{\xi} - \mathbf{r}|\right)}{|\boldsymbol{\xi} - \mathbf{r}|}}_{U'} ds$$

(1.12)

where the origin coincides with the location of the reference point source, $\mathbf{r}$ is the point (x, y, z) at which the complex wavefront is to be computed, $\boldsymbol{\xi}$ is a point (X, Y, Z) on the once-aperture-now-sensor plane, and a plus sign appears in the obliquity factor because the source and reconstruction plane now lie on the same side of the 'aperture' plane.
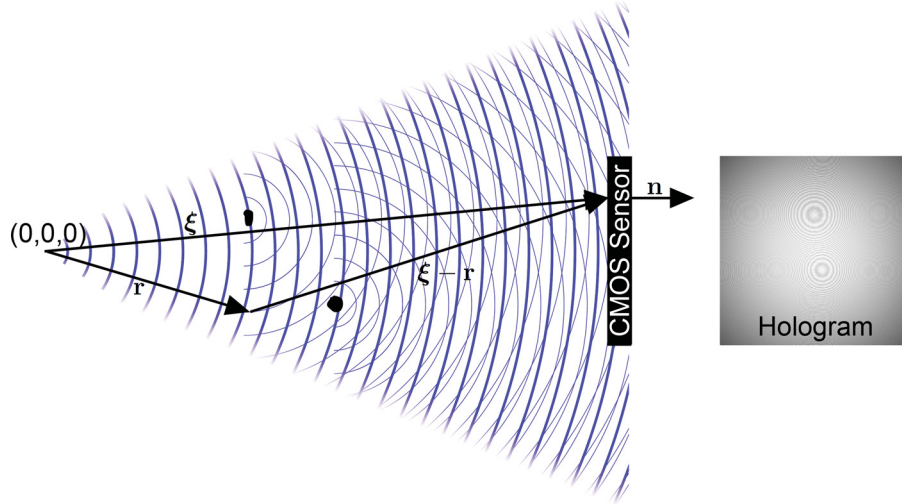
Figure 1.6: A diagram showing the setup for point source digital in-line holographic microscopy which includes the relevant vectors used in the derivations. Also shown is a simulated hologram for two scatterers.

The first approximation that is made assumes that angles are small so that the obliquity factor ≈ 1. This becomes increasingly accurate as distances from the sensor increase; for a point source with numerical aperture of 0.5, $\cos(\theta_{max}) = 0.87$. Thus

Equation 1.12 becomes

$$U(\mathbf{r}) = \frac{i}{\lambda} \int \int_{\Sigma} \underbrace{I(\boldsymbol{\xi}) \frac{\exp\left(-ik|\boldsymbol{\xi}|\right)}{|\boldsymbol{\xi}|}}_{U'} \frac{\exp\left(ik|\boldsymbol{\xi} - \mathbf{r}|\right)}{|\boldsymbol{\xi} - \mathbf{r}|} ds \qquad (1.13)$$

This approximation is used frequently and it has even been used in the shifted-impulse convolution method described in Chapter 4, though an approximate form of it (or an exact form of the Rayleigh-Sommerfeld diffraction integral) could have been used. This approximation was made so that comparisons with the dot-product approximation, which already used this method, could be made.

1.4.1   Dot Product Approximation

The next set of approximations are all related to the path-length difference in the complex exponential term of the Green's function. The first to be explained, the Dot Product Approximation, is named for the key feature present in the final equation. First, the path length difference is rewritten as

$$
\begin{aligned}
|\boldsymbol{\xi} - \mathbf{r}| &= \sqrt{(X - x)^2 + (Y - y)^2 + (Z - z)^2} \\
&= \left[(X^2 + Y^2 + Z^2) + (x^2 + y^2 + z^2) - 2(Xx + Yy + Zz)\right]^{\frac{1}{2}} \\
&= \left[|\boldsymbol{\xi}|^2 + |\mathbf{r}|^2 - 2\boldsymbol{\xi} \cdot \mathbf{r}\right]^{\frac{1}{2}} \\
&= |\boldsymbol{\xi}| \left[1 + \frac{|\mathbf{r}|^2}{|\boldsymbol{\xi}|^2} - \frac{2\boldsymbol{\xi} \cdot \mathbf{r}}{|\boldsymbol{\xi}|^2}\right]^{\frac{1}{2}} \qquad (1.14)
\end{aligned}
$$

Grouping the last two terms in the brackets together, the square root can be rewritten as a binomial series expansion

$$|\boldsymbol{\xi} - \mathbf{r}| = |\boldsymbol{\xi}| \left[1 + \frac{1}{2}\left(\frac{|\mathbf{r}|^2}{|\boldsymbol{\xi}|^2} - \frac{2\boldsymbol{\xi} \cdot \mathbf{r}}{|\boldsymbol{\xi}|^2}\right) - \frac{1}{8}\left(\frac{|\mathbf{r}|^2}{|\boldsymbol{\xi}|^2} - \frac{2\boldsymbol{\xi} \cdot \mathbf{r}}{|\boldsymbol{\xi}|^2}\right)^2 + \ldots\right] \qquad (1.15)$$

and if $|\mathbf{r}|$ is small compared to $|\boldsymbol{\xi}|$ then quadratic and higher terms can be neglected. Equation 1.15 then becomes

$$|\boldsymbol{\xi} - \mathbf{r}| \approx |\boldsymbol{\xi}| + \frac{1}{2}\frac{|\mathbf{r}|^2}{|\boldsymbol{\xi}|} - \frac{\boldsymbol{\xi} \cdot \mathbf{r}}{|\boldsymbol{\xi}|} \qquad (1.16)$$

If the second term is $\leq \lambda/4$ then the approximation will be negligibly different from the true expression for the path-length difference. This implies that the reconstructions will be most accurate near the point source of light. The limit for $|\mathbf{r}|$ is found by comparing terms

$$\frac{1}{2}\frac{|\mathbf{r}|^2}{|\boldsymbol{\xi}|} \leq \frac{\lambda}{4}$$

$$|\mathbf{r}| \leq \sqrt{\frac{\lambda|\boldsymbol{\xi}|}{2}} \tag{1.17}$$

Under the assumption that this limit for $|\mathbf{r}|$ holds, Equation 1.13 is then rewritten and simplified as

$$
\begin{aligned}
U(\mathbf{r}) &\approx \frac{i}{\lambda}\int\int_{\Sigma} I(\boldsymbol{\xi})\frac{\exp\left(-ik|\boldsymbol{\xi}|\right)}{|\boldsymbol{\xi}|}\frac{\exp\left[ik\left(|\boldsymbol{\xi}|-\frac{\boldsymbol{\xi}\cdot\mathbf{r}}{|\boldsymbol{\xi}|}\right)\right]}{|\boldsymbol{\xi}-\mathbf{r}|}ds \\
&= \frac{i}{\lambda}\int\int_{\Sigma}\frac{I(\boldsymbol{\xi})}{|\boldsymbol{\xi}||\boldsymbol{\xi}-\mathbf{r}|}\exp\left[-ik\left(\frac{\boldsymbol{\xi}\cdot\mathbf{r}}{|\boldsymbol{\xi}|}\right)\right]ds \\
&\approx \frac{i}{\lambda}\int\int_{\Sigma}\frac{I(\boldsymbol{\xi})}{|\boldsymbol{\xi}|^2}\exp\left[-ik\left(\frac{\boldsymbol{\xi}\cdot\mathbf{r}}{|\boldsymbol{\xi}|}\right)\right]ds
\end{aligned}
\tag{1.18}
$$

where the scaling factor outside the exponential was further approximated since the integral is most sensitive to changes in the rapidly changing complex exponential. This expression is referred to as the Dot Product approximation and is the most accurate of commonly used approximations for holographic reconstructions. It is this expression that is used as a starting point in Kreuzer's patented reconstruction algorithm [70].

While Equation 1.17 seems to limit the volume where reconstructions can be made, reconstructions can be made in the volume closest to the pinhole to approximately 1/3 the source-to-sensor distance. Beyond this distance, aliasing causes image overlapping in reconstructions. When reconstructions of the wavefront are made with $|\mathbf{r}| > \sqrt{\lambda|\boldsymbol{\xi}|/2}$, the distances from the point source at which objects appear 'in-focus' will be systematically larger than they should be, the objects will appear slightly distorted, and the sizes of the objects will also be systematically larger than they should be. It should be noted, however, that this is one of the fastest, most accurate

approximations available, and with user defined pixel spacing in the reconstructions using Kreuzer's patented method it is one of the most flexible, too.

1.4.2   On-Axis Approximation

The ability to choose the reconstruction pixel spacing arbitrarily in Kreuzer's method is a consequence of his clever use of convolutions. This method can also be applied to the on-axis approximation of the dot product approximation. The on-axis approximation assumes that the numerical aperture of the system defined by the point source to sensor distance and the physical size of the chip is small. If that is the case then Equation 1.18 can be written as

$$U(\mathbf{r}) \approx \frac{i}{\lambda} \int \int_{\Sigma} \frac{I(\boldsymbol{\xi})}{Z^2} \exp\left[-ik\left(\frac{\boldsymbol{\xi} \cdot \mathbf{r}}{Z}\right)\right] ds \qquad (1.19)$$

This form of the equation speeds up calculations a little compared to the dot product approximation while retaining the ability to have user defined pixel spacing, but the reconstruction errors are more significant. This method has not been adopted since the performance of the more accurate dot product approximation is already very good.

1.4.3   Fresnel Approximation

The Fresnel approximation is less accurate again, but it is still commonly used for numerical reconstructions. It uses the object to sensor distance, so we define $d \equiv Z - z$. The path length difference is then approximated in the following manner

$$
\begin{aligned}
|\boldsymbol{\xi} - \mathbf{r}| &= \sqrt{(X-x)^2 + (Y-y)^2 + (Z-z)^2} \\
&= d\left[1 + \frac{(X-x)^2 + (Y-y)^2}{d^2}\right]^{\frac{1}{2}} \\
&= d\left[1 + \frac{1}{2}\frac{(X-x)^2 + (Y-y)^2}{d^2} - \frac{1}{8}\left[\frac{(X-x)^2 + (Y-y)^2}{d^2}\right]^2 + \ldots\right] \\
&\approx d + \frac{1}{2}\frac{(X-x)^2 + (Y-y)^2}{d} \qquad (1.20)
\end{aligned}
$$

This approximation is accurate when

$$\frac{d}{8} \left[\frac{[(X-x)^2 + (Y-y)^2]_{max}}{d^2} \right]^2 \leq \frac{\lambda}{4} \tag{1.21}$$

that is, when

$$d > \left[\frac{[(X-x)^2 + (Y-y)^2]^2_{max}}{2\lambda} \right]^{\frac{1}{3}} \tag{1.22}$$

Practically speaking, this minimum object to sensor distance is on the order of 0.5 m, and since the resolution limit is inversely proportional to the numerical aperture of the holographic setup this method is not well-suited to holographic microscopy.

1.4.4 Fraunhofer Approximation

The only other approximation that might be considered is the Fraunhofer approximation. However, Fraunhofer diffraction describes far field diffraction patterns; it occurs when the second term of Equation 1.20 is negligible (pp. 74-75 [56]). This approximation is not valid except for large object to sensor distances (> 350 m), or when additional optics are introduced into the optical system. This approximation is not used in numerical reconstruction methods.

1.5 Decreasing Numerical Reconstruction Times

1.5.1 Multicore Central Processing Units

One of the main ways that computational speed has increased over the years has been through increased clock rates for the Central Processing Unit (CPU). In the last 30 years, clock rates have increased by a factor of 1000, but processor speeds, now in the GHz range, cannot be increased much more. Thus, in order to perform more calculations per second, processes must be spread out over many processors; this is the method that supercomputers have used for years. While home computers commonly have 4 processors and can have even more, programming them to use their full computational power effectively can be a difficult prospect. Setting up

computational threads takes time as resources are allocated, so depending on the number of cores available and their speed, there are some computations that take longer to divide and run over multiple processors than to do serially on one CPU. Still, when processes are optimized, multiple CPUs can be effective at computing complicated scientific problems, such as diffraction integrals. After first optimizing and simplifying Kreuzer's patented reconstruction algorithm that uses Fast Fourier Transforms (FFTs) [80] and convolutions, reconstruction times for a transform of a 2048×2048 pixel hologram to a 2048×2048 pixel reconstruction were tested on an 8 core (2 GHz) computer system. Computing reconstructions with 1 core took 1.56 s per frame; with 2 cores, 0.90 s per frame; with 4 cores, 0.57 s per frame; and with 8 cores reconstructions took 0.39 s per frame. With the additional time required to split the job up for the multiple processors, 8 times as many processors only resulted in a speed increase factor of 4. These tests made it clear that a home computer using multiple CPU cores would not be capable of doing real-time reconstructions, since adding more than 8 cores would not increase the speed significantly.

1.5.2 Parallel Processing Hardware

A recent review by Gao and Kemao [81] talks about the various possible systems that can be used to compute data in parallel. The primary techniques include Multiple Instruction Multiple Data (MIMD) processors (e.g. multicore computers, compute clusters), Single Instruction Multiple Data (SIMD) processors (e.g. Graphics Processing Units (GPUs), vector processors), and hybrids of the two (e.g. Field Programmable Gate Array (FPGA), IBM Cell processor, Application Specific Integrated Circuit, Digital Signal Processor, and a computer that can leverage GPU computations). When this project started, FPGAs, IBM Cell processors, and GPUs all offered approximately the same processing power. The high cost, low level programming, and limited technical support precluded the use of FPGAs. The limited amount of memory for the IBM Cell in the cheapest available platform (the Sony Playstation 3) meant that Fast Fourier Transforms (FFTs) of large two-dimensional arrays

would be difficult or impossible. The remaining method, GPU programming, was the approach taken to achieve real-time hologram reconstructions.

While GPUs were comparable to the other techniques at the start of the project, their computational power has increased faster than the other techniques since then. The ever-increasing demands for realism and special effects in the gaming industry has led to dramatic increases in computational power on GPUs: a single modern GPU (GTX 580) can achieve more than 1500 GigaFLOPS (FLoating point Operations Per Second), or approximately 10 times more than the other methods [81]. This year's model, the GTX 680, has peak performance of more than 3000 GigaFLOPS. If problems are suited to the SIMD nature of GPUs, then GPUs are the clear choice for hardware acceleration.

1.5.3   Graphics Processing Units and Introduction to the Third Paper

GPUs, initially designed for graphics acceleration, are becoming increasingly important for scientific computing. In 2006 nVidia introduced the Compute Unified Device Architecture (CUDA), which allows programmers to use the computational power of a GPU with the C programming language and access hundreds of parallel cores, with low thread setup times. Unlike the CPU where accessing memory can be preferable to computing certain mathematical functions, GPU programming often works best by computing everything explicitly rather than using look-up tables.

For computations that are easy to parallelize, using a GPU shows notable performance increases over CPU computations. Using a Tesla c1060 with 240 compute cores, Kreuzer's patented reconstruction algorithm was computed in 60 ms for a 2048×2408 pixel hologram and a significant portion of that time was actually associated with memory transfers to and from the GPU. This is approximately 10 times faster than a quad core CPU and fulfils the original project goals for real-time reconstructions. The newest series of GPUs released this year have faster memory, new (faster) transfer methods to and from the main computer, and approximately 7 times more compute cores compared to the Tesla c1060 (the GTX 680 has 1536 compute

cores). All of these factors will work to increase reconstruction speeds and if the number of memory transfers to and from the host device are minimized, it may be possible to see further performance increases.

With such an improvement in computational speed and with the knowledge that the dot product approximation used in the patented algorithm has its limitations, different methods to solve the Kirchhoff-Fresnel integral without approximations were investigated. The explicit calculation of the integral in Equation 1.12 for 2048×2048 reconstruction points based on a 2048×2048 pixel hologram takes ~ 1 h on the Tesla c1060 compared to 1 week on a quad core CPU. For geometries symmetric about the optical axis, 4-fold symmetry can be exploited in the calculations; the computation time for one reconstruction on the GPU, without approximations, was reduced to 22 minutes. However, despite the performance increase over the CPU, this is still too slow to be practical.

While analyzing the geometries involved with the path-length differences used in the direct evaluation of the diffraction/reconstruction integral to optimize the reconstruction algorithms, it became clear that many parts of these calculations were repeated (see Figure 1.7). In fact, if the spacing of the reconstruction points is set to equal the pixel spacing of the recorded hologram, then the problem reduces to a convolution integral[6], which can then be evaluated much more quickly using FFTs. This reconstruction pixel spacing is chosen purely for mathematical convenience so that reconstructions can be evaluated quickly; information can still be present in the hologram that allows higher resolution reconstructions to be made.

To obtain higher resolution reconstructions using the convolution method one must evaluate the integral multiple times by shifting the origin of the impulse function laterally subpixel-sized distances (that is, in x or y, while maintaining the same

---

[6]The problem reduces to a convolution integral so long as there isn't a sum of cosines in the obliquity factor, like with the full Kirchhoff-Fresnel integral, which would then make it impossible to separate pieces of the integral.
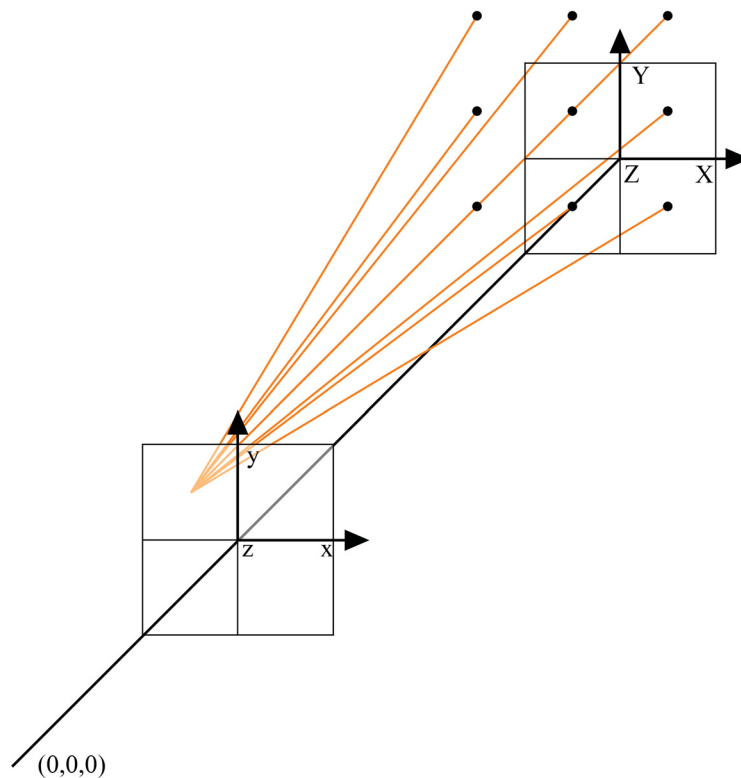
Figure 1.7: In this figure all of the vectors $(\boldsymbol{\xi} - \mathbf{r})$ that are possible when the reconstruction pixel spacing equals the hologram pixel spacing have been drawn (orange lines). This geometric representation also makes it clear that convolutions can be used to reconstruct the hologram if the hologram is zero padded from N × M pixels to 2N × 2M pixels.

reconstruction plane, z) for each evaluation, and then interleave the results (see Figure 1.8).[7] Using GPUs to evaluate high resolution reconstructions (i.e. with multiple reconstructions in a plane), comparing the reconstruction accuracy to results from the dot product approximation, and showing the flexibility of the convolution technique for various geometries in holography are the subjects presented in the Optics Letter submission, which can be found in Chapter 4.

---

[7]One can think of the origin of the impulse function as the position of the centre-most point in the reconstruction plane if one were to evaluate the diffraction integral directly. Constructing the impulse response function is as simple as calculating $\exp(ik[(X - x_0)^2 + (Y - y_0)^2 + (Z - z)^2]^{\frac{1}{2}})$ for each point on the screen, and shifted impulse response functions are calculated as $\exp(ik[(X - x_0 - \delta x)^2 + (Y - y_0 - \delta y)^2 + (Z - z)^2]^{\frac{1}{2}})$, where δx and δy are the subpixel-sized lateral shifts.
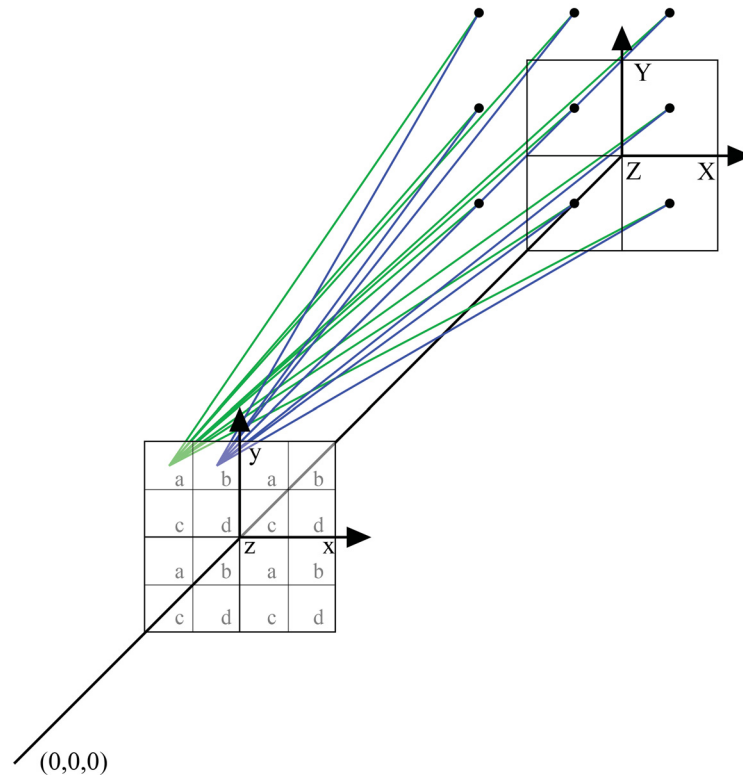
Figure 1.8: For higher reconstruction resolution with convolutions, multiple impulse response functions are required. In the setup shown here, 4 separate impulse response functions will be needed. All vectors $(\boldsymbol{\xi} - \mathbf{r})$ that are possible for two of the four impulse response functions are shown here, to demonstrate the subtle differences between the vectors. The reconstruction points for each of the separate functions (labelled a, b, c, and d) all have the same pixel separation as the hologram.

It is important to note that using convolutions for reconstructions itself is not new; the theory for performing reconstructions using single convolutions was developed as early as 1966 [82, 83], and the first known use of convolutions in optical and digital reconstructions of sub-optical (acoustic or microwave) holograms was as early as 1974 [84]. The first use of multiple convolutions in a single reconstruction plane was presented with multiple integer pixel sized shifts in an effort to make a larger field of view, rather than increasing the resolution for microscopic purposes [85–90]. It was found, after submitting the paper (found in Chapter 4) to Optics Letters, that Lenart *et al.* [91–93], have also used this subpixel-sized shifting technique in

FPGA accelerated reconstruction techniques. However, the power of the GPU, its rapid development cycle, and its ease of programming all lend favour to its future and continued use over FPGA solutions. The large market and the competition between video card manufacturers in the gaming industry keep consumer prices low while pushing the development of GPUs with greater numbers of parallel computing cores faster than FPGA development. The GPU based reconstructions presented in this body of work have some room for optimization, but they already compare well against the FPGA methods. In their 2008 paper [93], Lenart *et al.* propose an FPGA architecture that should attain 20 fps for a method that is most comparable to the patented method of Kreuzer [70], which already runs at ~ 16 fps ($\frac{1}{60 \text{ ms/reconstruction}}$) on the Tesla c1060 (240 cores). Additionally, Kreuzer's method on GPUs could be sped up by as much as one order of magnitude with the newest generation of GPU (Kepler with 1536 compute cores) provided memory transfers do not become an issue. The code from this body of work, created to achieve these reconstruction rates with the GPU, has already been integrated into the commercially available holographic microscope by Resolution Optics [94].

Chapter 2

Simultaneous Holographic, Ellipsometric, and Optical Imaging of Pitting Corrosion on SS 316LVM

Authors: P. E. Klages, M. K. Rotermund, and H. H. Rotermund

Department of Physics and Atmospheric Science, Dalhousie University, 6310 Coburg Road, Halifax, Nova Scotia, B3H 4R2, Canada

2.1 Abstract

Digital in-line holographic microscopy, a three-dimensional imaging technique, is incorporated for simultaneous usage with the previously established surface sensitive optical imaging techniques, ellipsomicroscopy and microscopy. This addition allows volume reconstructions of the solution in the vicinity of the working electrode with microscopic resolution, and particle tracking. Holography is also sensitive to local variations in the solution concentrations; estimations of the index of refraction can be made using the interference patterns alone. These three optical techniques complement each other and simultaneously provide information about changes in the oxide layer, pit developments, and local solution changes during electrochemical testing of stainless steel.

2.2 Introduction

It has been suggested that after pit nucleation has occurred at surface heterogeneities [4,5], physical barriers such as perforated oxide layers [17,18], salt films [19], or poly-sulphide skins [16] assist in the transition to metastable and stable pitting regimes [20]. Most nucleation events that occur on an open surface have spikes in the anodic current on the order of picoamps and immediately end in repassivation [95]. However, when physical barriers are present, aggressive anolytes with low pH values, and high Cl^- and metal cation concentrations can be maintained, allowing continued dissolution of the metal [13,18,20]. In the metastable regime, the current rises in a stepwise fashion as new holes form in the cover as the pit grows and undercuts the once-protective oxide layer [17–20]. If the cover should rupture or break before the depth of the pit is sufficient to limit the diffusion of cations and sustain the aggressive local environment, then the pit will repassivate. If, on the other hand, the current and pit radius should exceed a 'pit stability product' threshold, then pit growth will continue without a cover and the pit is considered to be stable [20,96].

While it is clear that inclusions, defects and crevices are the primary sites for pitting, it is less clear whether nucleation sites are spatially and temporally stochastic or whether the initiation and metastable pitting sites work together in a reaction-diffusion manner [26]. Using bundles of insulated microelectrodes, spatiotemporal relationships for pitting events based on local solution changes have been investigated [31], but for testing relationships between pits on a single electrode, *in situ* optical techniques excel.

Despite the spatial resolution limitations for optical imaging techniques, the parallel nature of optical image acquisition lends itself well to spatiotemporal analysis of metastable and stable pitting events. While scanning techniques such as electrochemical atomic force microscopy [97] and scanning tunnelling microscopy [98] have nanometre lateral resolution, they are limited by scan times and scan areas. Optical microscopic techniques, on the other hand, have the ability to meaningfully image an

entire area from many hundred μm^2 to several mm^2 *in situ* and in real-time, with temporal resolutions limited only by the recording devices used; commercial devices are available with recording rates higher than 1000 frames per second (fps). These temporal characteristics compensate for the spatial resolution ($\sim$ micron resolution) available to optical techniques.

To correlate anodic current events with physical pits at the surface of stainless steel samples, two complementary optical methods have previously been investigated by our group: Ellipsomicroscopy for Surface Imaging (EMSI), and background subtracted contrast enhanced microscopy [29, 30]. Used simultaneously, microscopy and EMSI revealed the interplay between the initial pits: after a pitting event was observed with the *in situ* microscope, a weakening of the surrounding oxide layer in a diameter of 50 to 100 μm around the pit was observed with EMSI [30], which consequently allowed more pitting events to initiate.

While simultaneous *in situ* microscopy and EMSI has enhanced the analysis of spatiotemporal relationships in potentiostatic and potentiodynamic experiments, there are still limitations in using these methods alone. For example, the lensing effects at active pits observed by microscopy [29] indicate local changes in the solution but microscopy cannot measure them. In addition, the optical methods we have used until now cannot determine how far into the volume from the wire face the electrolyte is affected, nor do they show how great the change in the index of refraction may be. Also, the limited depth of field associated with both of the imaging techniques means that they are very sensitive to alignment errors and has only allowed for the observation of debris released into the electrolyte from large active pitting sites (e.g. pieces of pit covers, or undissolved inclusion pieces) directly in front of the samples. To overcome these limitations we require a three dimensional microscopic technique.

Holography, originally developed by Gabor [58], is a coherent light optical technique that uses a priori knowledge of a reference wave to recover, or reconstruct, the complex wave-front corresponding to light scattered from an entire volume using a

single 2-dimensional interference pattern. In the field of corrosion, local concentration changes in the solution or deformations at the surface have been analyzed using 2-beam holographic interferometric techniques [44, 49, 99, 100]. To add microscopic resolution volume imaging to our system, while maintaining the ability to analyze local concentration changes via interferometric techniques, point source digital in-line holographic microscopy (DIHM) [65, 69, 72, 76] is implemented here. It is the simplicity of this single-beam technique that allows it to be used simultaneously with other optical techniques, such as microscopy and EMSI.

This paper describes the implementation of the three concurrent optical techniques. Using case studies of pitting corrosion on SS 316LVM in 0.9 % (by mass) NaCl solution, it discusses the merits and limitations of each individual technique and shows how, when they are used together, new insights can be gained.

2.3 Optical Techniques and Experimental Setup

Figure 2.1 shows a diagram of the optical setups used for the experiments. The optical paths for EMSI and microscopy lie in one plane and image the polished face of the wire. The central optical axis for DIHM is perpendicular to the other two paths and is parallel to the plane of the sample. DIHM records information about the volume of the solution in front of the polished surface. Each technique uses a different wavelength of light and optical filters are used to suppress crosstalk of the light sources from the individual techniques: a band pass filter is used on the camera for holography and an interference filter on the camera for microscopy.

For the EMSI path, a collimated HeNe (632.8 nm) laser beam passes through a linear polarizer, followed by a compensator (quarter-wave plate) to create elliptically polarized light. If the elliptically polarized light strikes a polished, flat surface at the Brewster angle ($\sim 65°$) then the light reflected from the sample will be linearly polarized. This polarized light passes through a second linear polarizer (the analyzer), and is imaged onto a CCD sensor and recorded at 25 fps. The sensor is tilted to best
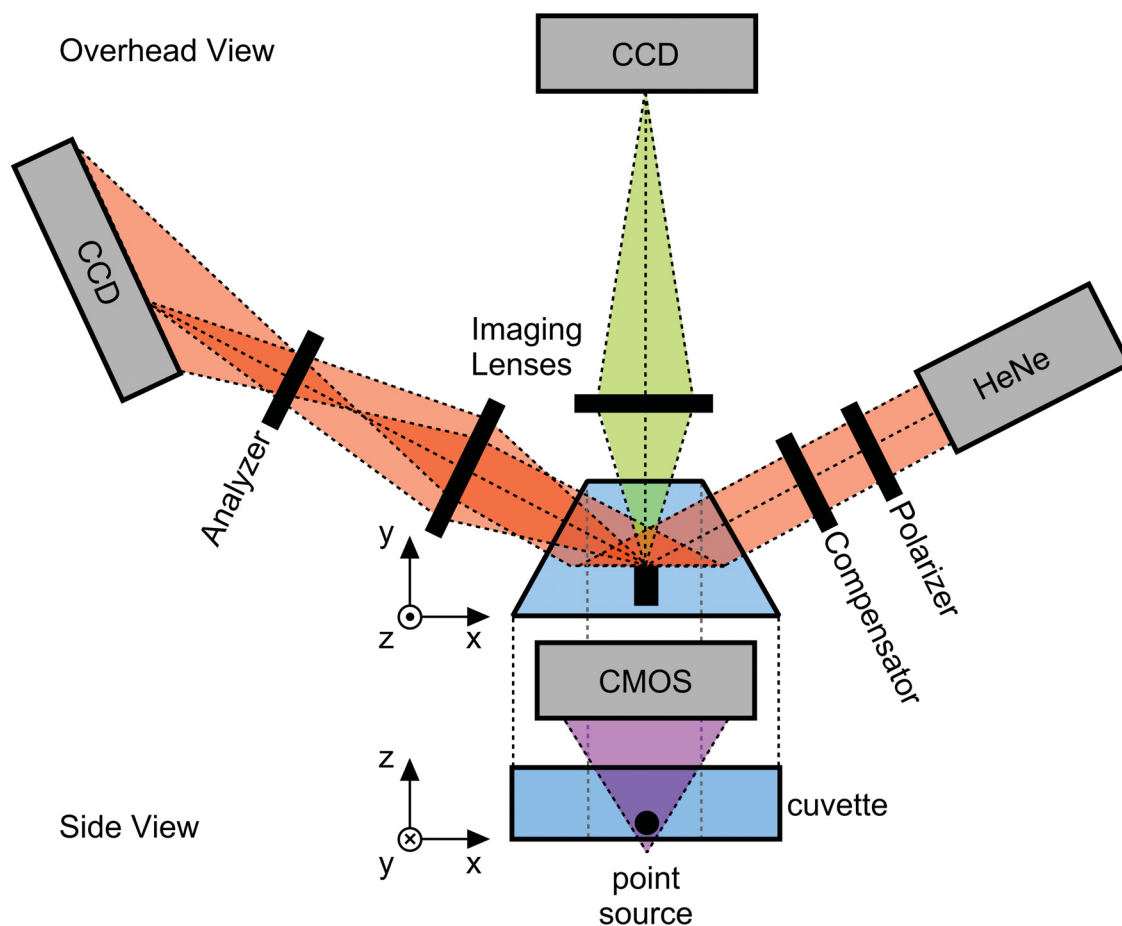
Figure 2.1: The optical setup for the complementary techniques. For Ellipsometry for Surface Imaging (EMSI), light originates at a HeNe laser, and then travels through a polarizer and compensator to create elliptically polarized light. This light reflects off the polished surface of the wire face passes through another polarizer before being recorded at the CCD camera. The microscope images the face of the wire. In the holography setup, as depicted in the side view, the point source of light is located directly below the cuvette, and light scatters off of objects in the cuvette, creating an interference pattern with the spherical reference beam, which is recorded at the CMOS camera. The sample wire itself is visible as a shadow and the corresponding interference fringes. These holograms can be used to numerically reconstruct the volume of solution in front of the working electrode with microscopic resolution.

fulfil the Scheimpflug criteria [40] to correct for the distortions and focusing problems that occur when imaging a surface at 65°. Any remaining distortions can be removed with computer processing, if required. In EMSI, the analyzers polarization angle is set such that the intensity of light received at the camera is close to a minimum, and is then kept at that orientation for the duration of the experiment. Differences in the image from the almost-nulled image show qualitative changes in the oxide layer and the surface of the wire face. A well-aligned EMSI setup is sensitive to changes in the oxide layer on the order of nanometers despite having lateral resolution on the order of 10 microns.

Additional details of the experimental setup are shown in Figure 2.2. For the optical microscope the LED light source and the camera are in two separate paths and are combined using a beam splitter before the lens. The lens both focuses the light from the LED onto the polished face of the wire and images the reflected light onto a CCD sensor. The lateral resolution is approximately 2 microns, which is close to the diffraction limit for our system, and images are again recorded at 25 fps. The brightness and contrast of the microscopic images can be adjusted after the experiment using either a Hamamatsu image processor or a video editing program.

The DIHM setup is composed of a violet laser (iPulse 406 nm, Toptica) working in continuous wave mode that is focused onto a 700 nm pinhole in a thinned molybdenum disk (Norsam Technologies) using a $100 \times$ (0.9 NA Zeiss) objective. The light that passes through the pinhole is spatially filtered and closely approximates a point source. This semi-hemispherical reference wave interferes with light scattered from objects in the electrolyte such as the wire itself and ejected material from active pitting sites, as well as light passing through regions with local solution concentration changes. The resulting interference patterns, or holograms, are recorded with a monochrome CMOS camera (Toshiba Teli CSB4000-10F) with 6 μm pixel size. At full resolution (2008×2044), images are recorded at 6 fps, and at half resolution (2000×1000 pixels), 12 fps sequences are taken.
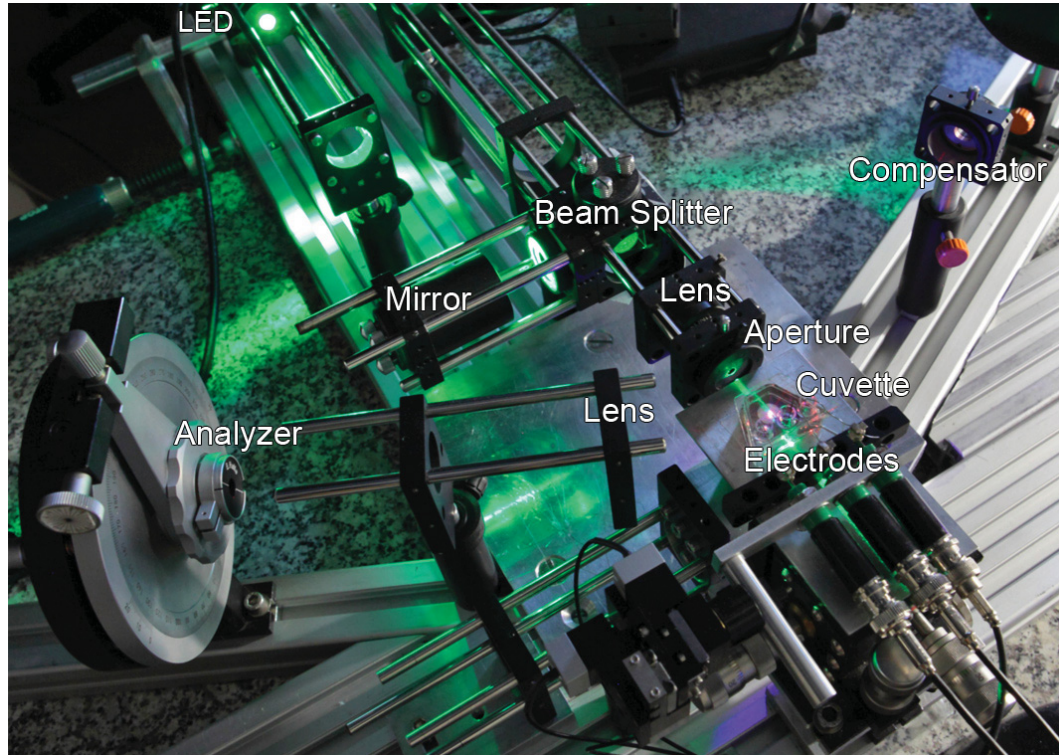
Figure 2.2: A photo of the aligned experimental setup with additional details of the components compared to the schematic in Figure 2.1. The bright violet light below the centre of the cuvette is the point source of light for the DIHM, created by a laser beam focused through a 700 nm pinhole.

To achieve the best possible volume reconstructions from each hologram, the expected positions for objects being imaged and the point source-to-sensor distance must be considered carefully. The resolution limit of a digital hologram reconstruction is inversely proportional to the numerical aperture of the system. To increase the numerical aperture and thereby lower the resolution limit for reconstructions, the point source-to-sensor distance can be decreased. As an example, 1 micron diameter latex beads have been successfully resolved with a point source-to-screen distance of 15 mm [77]. However, decreasing the point source-to-screen distance also reduces the distance from the point source where aliasing problems begin to occur in the reconstructions of objects. To avoid aliasing in reconstructions for the solution volume contained by the cuvette, while still maintaining a lateral resolution of a few microns,

the source-to-screen distance for our specific setup was fixed to a minimum of 25 mm.

Custom glass cuvettes were created to accommodate the 3 separate imaging methods. The cuvettes have an isosceles trapezoid shape, with a base angle of 65° to allow the laser beam for the EMSI, as well as the microscope path, to pass through the glass walls perpendicularly. The glass cuvette walls were melted and bent to the correct angles over a mould, then annealed to relieve stresses that would otherwise affect the polarization of the light for the EMSI measurements. Since the resolution for DIHM reconstructions is best closest to the point source of light, cover-slide glass (0.17 mm thick) was used as the base.

Glass lids with cylindrical access ports for the electrodes were created for the cuvettes to improve the holographic optical path while eliminating the effects of evaporation during experiments. With open cuvettes, it was found that evaporation rates were as high as 8 μg s^{-1} cm^{-2} in dry winter months, which would lead to vertical temperature gradients and convection in the solution. It was also found that with the small cuvette size (surface area: 4.1 cm^2), a meniscus would form that was strongly dependent on the volume of the electrolyte in the cuvette. This curved liquid-air interface would act as an ill-defined lens, and would therefore preclude accurate numerical holographic reconstructions of the solution below this interface, since the reference wave could no longer be accurately modelled. Filling the cuvette up into the access ports with electrolyte creates a well defined optical path for holography and controls the evaporation problem. If it is desired, mineral oil can be added to fill the access ports after the wires have been inserted to completely stop evaporation.

Prior to experiments, stainless steel AISI 316LVM wires, 0.381 mm (0.015 ") diameter (Smallparts Inc), were polished to a one-micron finish using silicon carbide paper and diamond suspensions. The wires were cleaned with acetone, rinsed with either ethanol or methanol, and then finally rinsed with high purity deionized water. Wire faces were inspected with an optical microscope and additional cleaning was done if it was necessary. The stainless steel wires were then bent so they could be inserted into the access ports and finally were painted with nail polish under

a stereomicroscope so that only the polished faces of the wire remained uncoated (Figure 2.3).
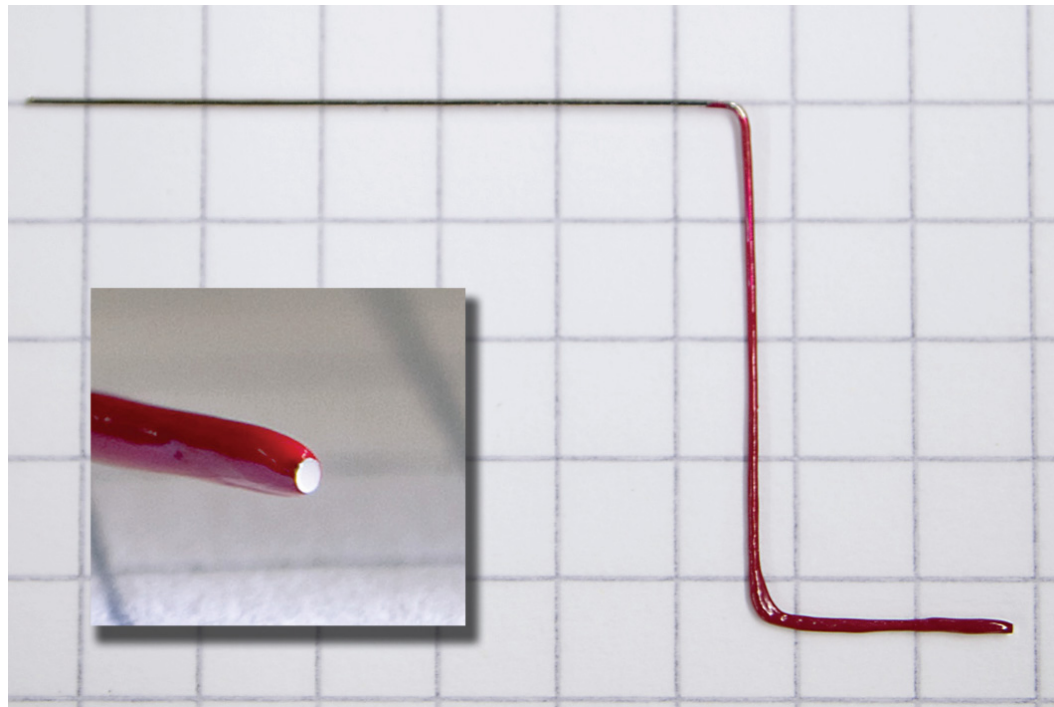
Figure 2.3: A photo showing a stainless steel working electrode that has been prepared for experiments. For reference, the graph paper squares measure 5 mm by 5 mm. Inset: a photo showing the polished face that serves as the working electrode.

For the electrochemical experiments, a 3 electrode configuration was used: an Ag/AgCl wire was chosen as the reference electrode, a platinum wire served as the counter electrode, and a prepared stainless steel wire was used as the working electrode. The potentiostat (Fritz-Haber-Institute, Berlin) and analog to digital converter combined had a minimum and maximum current sensitivity of 10 nA and 50 μA, respectively. The electric potential, current, and photodetector current (used to synchronize the data to the different optical techniques) were all sampled at 500 Hz. The electrolyte was a 0.9 % (by mass) NaCl solution to mimic biological conditions, and was filtered through a 0.2 μm filter before being put into the electrochemical cell. Experiments were started once the wires were aligned for all three optical setups using a 3-axis hydraulic manipulator (Siskiyou MX630R). The initial potential was set to

-400 mV and was increased at 10 mV/s until it reached 100 mV where it was held for 1 minute, then raised in 50 mV steps at ramp rates of 2 mV/s, holding at each step for 1 minute. After reaching +600 mV with respect to the Ag/AgCl electrode, the voltage was decreased at a rate of 10 mV/s until it again reached the starting potential of -400 mV, at which point the experiments were concluded.

2.4   Results and Discussion

For concurrent visualization of all of the data sets, the combined movies were set at a frame rate of 25 fps. The electric potential (with respect to the Ag/AgCl electrode) and anodic current data were plotted versus time as a sequence of graphs at 25 Hz. Background subtraction was performed on both the microscope and EMSI image sequences to show the changes associated with pitting events more clearly. A camera flash was fired for the initial synchronization of the separate feeds, and embedded timestamps were used to align the hologram and reconstruction sequences to the other data sets. To check the synchronization at the end of the experiments the flash was fired again. The duration of experiments ranged between 20 to 40 minutes; the synchronization error between the different data sets started below 40 ms and remained below 160 ms by the end of each experiment.

In general, metastable pits with peak anodic currents greater than 100 nA can be observed with all three optical techniques simultaneously. Discrimination between crevice corrosion and metastable pitting can easily be performed visually using these *in situ* techniques. For the set of experiments performed here, large pitting events (anodic currents > 10 μA) often displayed a lacelike pitting pattern indicating under-cutting of the oxide layer. Initial pitting events appeared to occur stochastically, both spatially and temporally; however, clusters of pits could be seen in the final images, so there may be evidence for the weakening of the oxide layer near pits, which allow

further nucleation of events. Video Clip 2.1[1] shows the different data sets synchronized in time for a metastable pitting event. The strengths and limitations for each of the individual optical techniques are discussed below.

Pits become visible in the microscopic images during periods of increasing anodic current and they remain essentially unchanged during periods of constant anodic current. Changes in the brightness at the face of the wire were observed around active pits of all anodic current magnitudes when background subtraction was performed on the images. This visual effect has previously been observed for large pitting events [16], and is caused by a local enhancement of ions at the pitting site–the concentration gradient in the solution effectively creates a lens over the pitting site. These distortions persist while the pit is active, and then disappear as the current drops when the pit repassivates. While the drop in current is sudden ($\sim$ 0.1 s), the relaxation periods for these distortions in the microscopic images are many times longer (on the order of seconds), which correspond with the diffusion and mixing times for the saline solution.

Because of its sensitivity to changes in the oxide layer via subtle changes in polarization, EMSI is still a very useful tool despite having lower lateral resolution than standard microscopy. Pitting sites can be determined by local brightness changes in background-subtracted EMSI images before the events are observable with the microscope. One such event (Video Clip 2.2[2] and Figure 2.4) shows a pitting site at anodic current levels of 50 nA, nearly 2 s before the pit is observable in the microscope images. However, since EMSI is also sensitive to concentration changes in the solution,

---

[1]Video Clip 2.1 (File: klages_CorrSci_videoClip2_1.mov Duration: 7 s) Time synchronized data sets for a corrosion experiment of SS 316LVM in 0.9 % by mass NaCl solution. This video shows the first metastable pitting event observed with microscopy, EMSI, and holography during the experiment. The resulting pit is located near the right edge of the wire. Since the reconstructions are based on sequentially paired holograms, only changes in the solution at the end of the event occur rapidly enough to show as bright regions.

[2]Video Clip 2.2 (File: klages_CorrSci_videoClip2_2.mov Duration: 5 s) Time synchronized data sets for a corrosion experiment of SS 316LVM in 0.9 % by mass NaCl solution. This is the same event that was reanalyzed with a reference hologram from before the event (Figure 2.4) and shows how the sensitivity to changes in the solution is limited when sequentially paired holograms are used.

differentiating between changes in the oxide layer on the wire face and concentration changes in the solution can be difficult. With the addition of simultaneous digital in-line holographic microscopy we can differentiate between the two effects. The holographic microscope will not be sensitive to oxide layer changes (nanometer features), but it will be sensitive to solution changes. If a feature or event is visible with EMSI, but not with holography, then it is considered to be only oxide layer related; observing an event with holographic reconstructions does not, however, exclude the possibility of surface oxide layer effects.

Since tens of thousands holograms are recorded during each experiment, holograms are paired with their nearest temporal neighbours (sequential pairing) for the reconstructions used in the combined data movies. Each numerical reconstruction represents a single in-focus microscope image, however the user chooses the plane that is in-focus after the experiment has concluded. For the time-synchronized movies a representative depth, often the plane associated with the bottom edge of the wire face, is used. These contrast holograms, paired in time, are only sensitive to changes that occur faster than the time difference between them. The changes in the solution associated with the mixing after a drop in the anodic current appear as a bright region on a dark background (see again Video Clip 2.2). Anodic current events $\geq$ 100 nA are visible in these sequentially paired reconstructions so for events smaller than 100 nA, which are still observed with EMSI, one cannot determine whether the changes are related to the oxide layer or the solution.

The sensitivity to pitting events using sequentially paired holograms is approximately the same as the optical microscope, but can be improved to include events $<$ 100 nA by using a different pairing technique. To achieve this higher level of sensitivity, one must analyze an anodic event frame by frame using a hologram chosen prior to the event as the background. Subtracting subsequent holograms from the background hologram shows changes in the interference patterns (holograms) from the undisturbed state as a function of time. If the holograms remain unchanged in time, then the reconstruction results will be comprised essentially of noise. If, on the
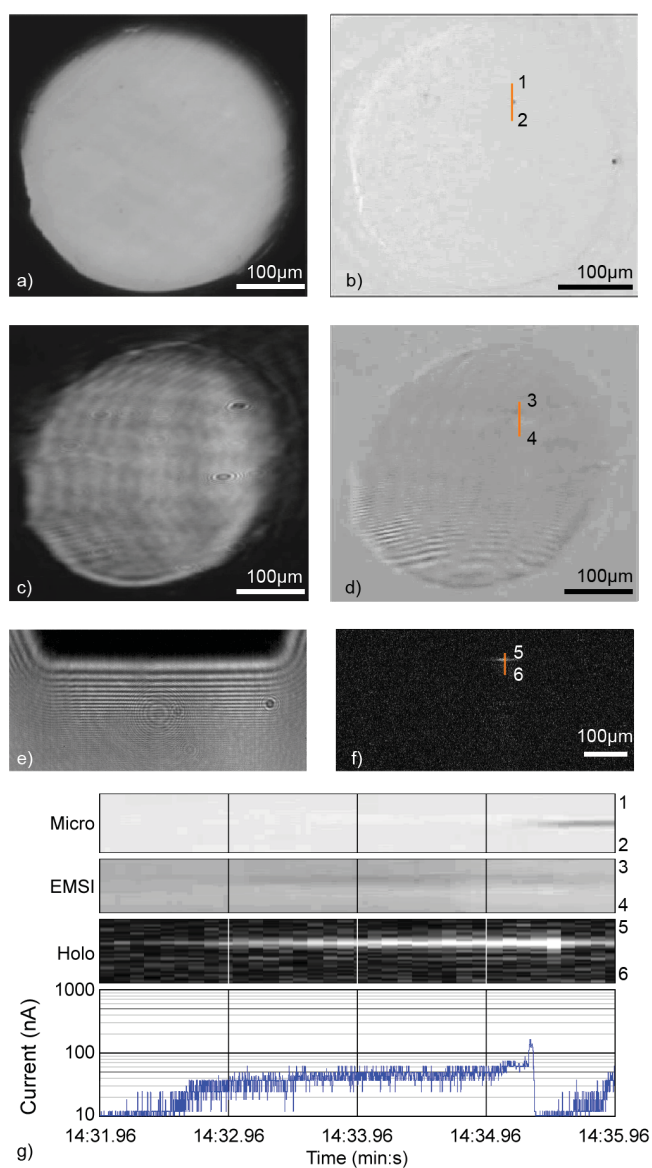
Figure 2.4: (a) *In situ* microscope image, (b) contrast enhanced, background subtracted microscope image, (c) EMSI image, (d) contrast enhanced, background subtracted EMSI image, (e) a hologram and (f) a reconstructed image showing a bright disturbance at the edge of the wire associated with the pitting event. In (g) space-time plots along the indicated lines: 1-2 (b), 3-4 (d), 5-6 (f), each 50 μm in length, are presented along with the anodic current versus time plot. The pitting site is visible in the reconstructed images near the very beginning of the anodic event. By 14:33 it is visible with EMSI, and it is only visible in the microscope at the end of the pitting event.

other hand, concentration changes should occur in the solution, then subtle changes in the fringe patterns will reconstruct to give the 3D location of that change in the solution. Reanalysis of the pitting event previously analyzed above, using this more sensitive reconstruction method, shows changes in the solution at the wire face in a region ~ 4 μm wide at an anodic current of ~ 25 nA. This implies that the changes were primarily solution based for this pitting event. Cuts of the reconstructed holograms and of the contrast enhanced, background subtracted EMSI and microscope images with the corresponding anodic current are plotted versus time in Figure 2.4. Sample source images from the end of the pitting event are also shown for context. The changes in the solution near the pitting site were detected with DIHM at almost the very beginning of the pitting event as registered with the potentiostat and approximately 1 s before the event was observed in with EMSI. Using this method it is also observed that the region of enhanced concentration does not fully disappear before a new anodic current event starts at the same position. It should be noted that for this experiment, the signal to noise ratio in the holograms was not ideal, so by improving the DIHM setup to increase the brightness of the point source, it is possible that even smaller changes in the solution would be detectable. With sensitivity to anodic events in the range of nano amperes or smaller, it could be possible to start to detect nucleation events as well as these microscopic sized metastable events.

Three-dimensional volumes can be recreated for any given time in the experiment by combining 2 dimensional reconstructions from the appropriate hologram for that time. In our present configuration of DIHM, the lateral (x-y as described in Figure 2.1) resolution is approximately 2 μm and the depth (z) resolution is ≥ 10 μm. Since single scattering is assumed in the numerical reconstruction procedure, it is easiest to accurately locate the z position for small regions (≤ 10 μm diameter) that contain concentration gradients. As well as concentration gradients, which have already been mentioned, one can observe physical objects moving through the solution with DIHM. Pitting sites, tens of microns in diameter, would occasionally eject pieces of sample that were large enough to be seen as individual particles using optical microscopy;

these particles have been measured and tracked through the solution using DIHM. In Figure 2.5 the 3-dimensional tracks of 3 particles ejected from a large pit are shown. The ejected particles ranged between 1 and 3 μm in diameter as deducted from the holographic reconstructions. They originate from the cluster of pits near the centre of the wire (Figure 2.6), travel downward, and then disperse as they pass the bottom edge of the wire. Since tracking these microscopic particles in 3D is possible, it should also be feasible, in future experiments, to separate particles if they are susceptible to effects from external fields such as static magnetic fields.

In an effort to identify the ejected particles, the solution can be studied using *ex situ* techniques such as Scanning Electron Microscopy (SEM) and Energy Dispersive X-ray Spectroscopy (EDS). After an experiment that clearly showed ejected particles with the optical microscope, the solution from the cuvette was filtered through a 0.4 μm Nucleopore track-etch membrane filter and the filter was then prepared for SEM/EDS analysis. Based on the x-ray spectra collected, for particles whose largest lateral dimension was ≤ 10 μm, a variety of chemical compositions were observed. We found particles containing strong sulphur peaks, as well as particles with strong oxygen, chromium, and iron signals, including some particles with the entire chemical makeup of stainless steel. However, since the particle ejections correlate with increases in the anodic current or with sudden drops in anodic current, it can be speculated that these large particles, observable individually in the microscopic image sequences (see Video Clip 2.3[3] for an example), were pieces of the pit cover.

For large pitting events, strong distortions in the holograms caused by the ion concentration gradients near the pit were observed. These regions behave like lenses and even refract light into the geometric shadow of the wire (see Figure 2.7). In practice, the smooth change in the index of refraction makes it difficult to obtain the

---

[3]Video Clip 2.3 (File: klages_CorrSci_videoClip2_3.mov Duration: 8 s) Time synchronized data sets for a corrosion experiment of SS 316LVM in 0.9 % by mass NaCl solution. This video clip shows a particle being ejected from the large pitting site (most clearly seen in the background subtracted microscope images). The particle comes into focus in the holographic reconstructions approximately 5 s into the clip. This video also shows multiple simultaneous events. As these events end, the anodic current drops suddenly and bright flashes are seen in the holographic reconstructions.
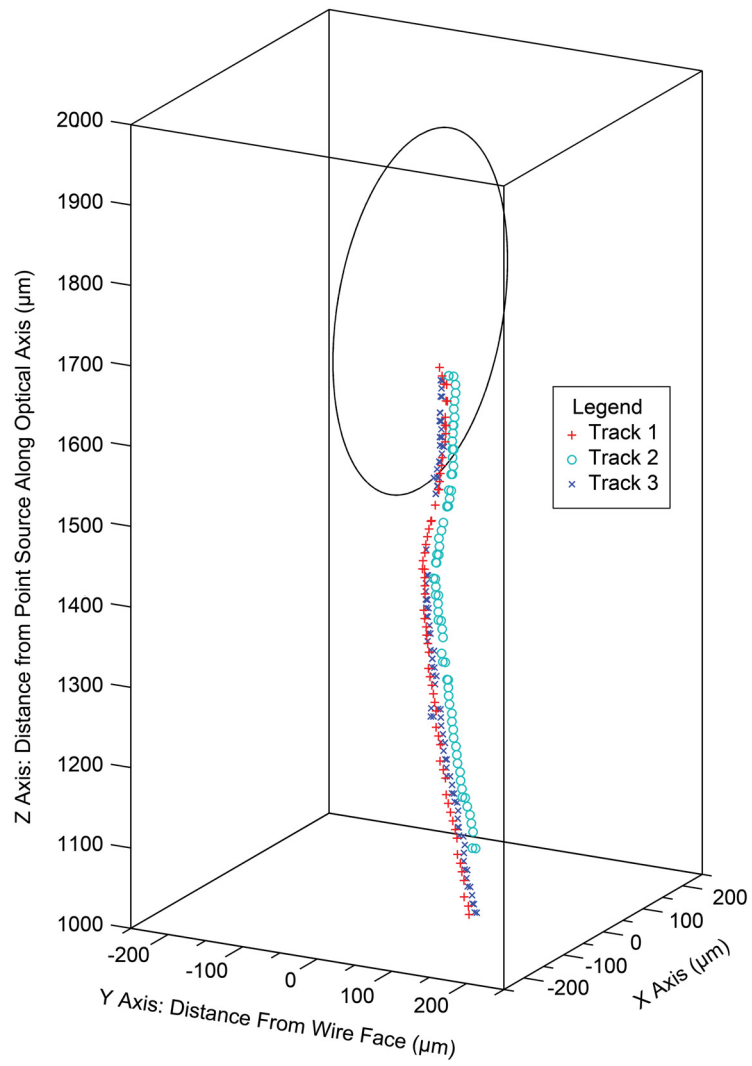
Figure 2.5: 3D tracks of particles emitted from near the centre of the wire face. A microphotograph of the wire face can be seen in Figure 2.6.
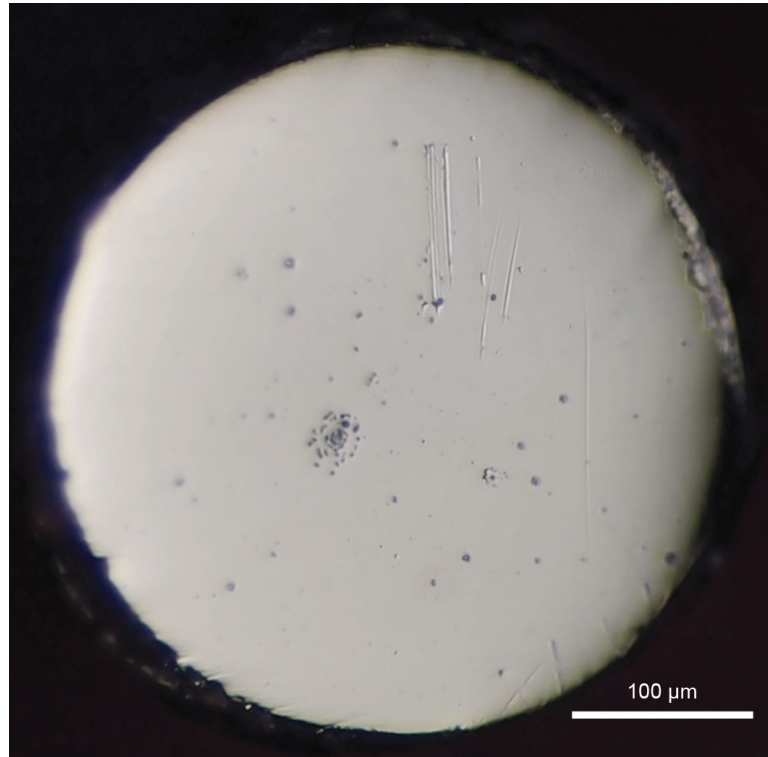
Figure 2.6: A microphotograph of the wire that the particles were released from and tracked in Figure 2.5. The cluster of dots near the centre is the pitting site that the particles originated from.

correct z-plane for these regions from the holographic reconstructions since there is no sharply defined edge, as is the case for particles, that can be used to determine the correct focal plane. However, the large events are clearly visible with EMSI and microscopy, so obtaining the correct z-position is a simple matter of correlating the x-position of the bright region in a reconstruction with active events sharing the same x-position in the microscope and EMSI images. For these types of events, one can estimate the change in the index of refraction caused by the ion concentration gradient in front of a pitting site. It is known that the macroscopic shape of the wire remains essentially unchanged during a pitting event, so if there are distortions in the interference fringe patterns that are associated with the wire then they are a result of the local disturbances. For a phase change of 3π radians in the fringe pattern, as seen in Figure 2.7b, if one assumes the disturbance has the same diameter

as the large (40 μm) pit observed with optical microscopy, then the average index of refraction for that region would be 1.347 (compared to 1.332 for 0.9 % by mass NaCl solution). This average index of refraction gives a way to estimate the local increase in ion concentrations at pitting sites, and is actually a low-end estimation since the index of refraction will not be constant, but will have a larger peak value that changes smoothly to the bulk value for the saline solution.

Reconstructions of holograms recorded with the wire face in line with the central optical axis visually demonstrate that the affected volume is strongly dependent on the anodic current associated with the event. However, to investigate how far from the wire face the solution is affected by active pitting sites and to establish the best position of the working electrode for sensitivity to pitting events, another set of experiments was performed. In these experiments, the face of the working electrode was moved both away from and beyond the central optical axis of the point source. If the wire face was before the central optical axis and the camera was moved to record the interference pattern starting at the geometric shadow of the wire, then a wedge shaped portion of the volume in front of the wire that increases from the top to the bottom of the wire would be obscured by the geometric shadow cast by the wire. Similarly, if the wires were beyond the central optical axis, then the bottom of the wires would cast shadows that would obscure the effects of small pitting events near the top of the wire. Events can only be detected with holography if the light goes through volumes with changes in the index of refraction so these occluded zones provide a method to test how far the local changes in concentration extend into the volume in front of the pits. The minimum anodic current at which a pitting event was detected using the most sensitive reconstruction technique is plotted against the occlusion distance in Figure 2.8; the occlusion distance is calculated using the position of the pit on the face of the wire and the distance of the wire from the central optical axis. If a pitting event was not detected with holography, then the maximum anodic current associated with that event was plotted with an open symbol. Only pitting events that occurred individually were plotted since the contributions of multiple
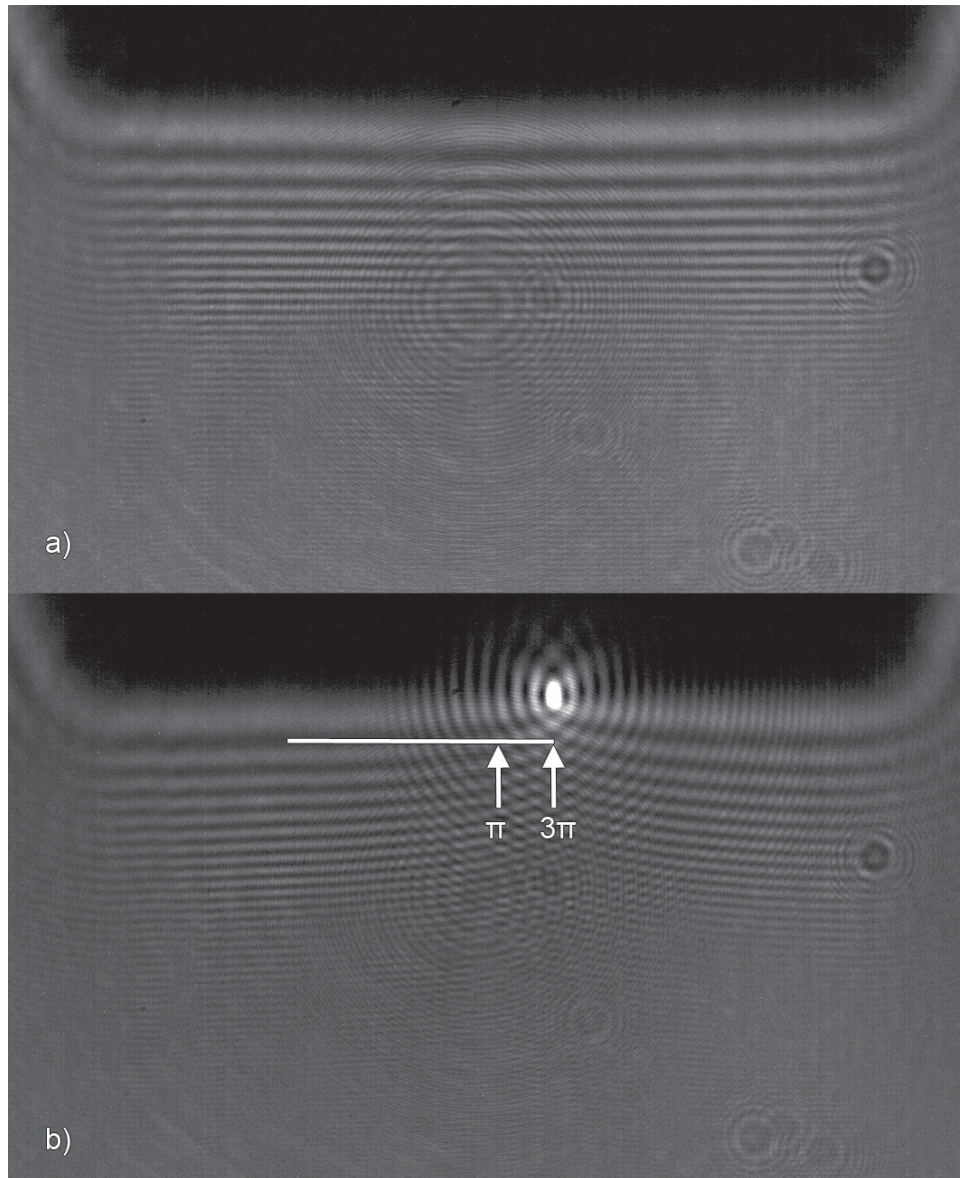
Figure 2.7: (a) the interference pattern (or hologram) of the wire before any events and (b) during a large pitting event. (b) shows how there is a 3π phase change to the centre of the disturbance from the hologram in (a) for a pitting event that measured ~ 40 μm in the *in situ* microscope image. The pixel spacing for the 1800×1000 pixel holograms is 6 μm and the point source to recording screen distance is 33.5 mm. The light from the point source scatters from the 381 μm diameter wire and a magnified interference pattern is created at the recording screen. Static objects on the glass surfaces of the cuvette appear as concentric circles in the interference patterns.

pitting events that occurred simultaneously could not be separated easily. It is for this reason that the data from the second experiment was excluded; experiment 2 had a stable pit form early in the experiment.

As it was expected, for each individual experiment, as the occlusion distance increased, the minimum anodic current required to observe the corresponding event also increased; the volume of solution affected by a pitting event is dependent on the magnitude of the anodic current. Ideally in Figure 2.8 one would expect to see a complete separation of observed and unobserved pitting events. However, this trend is slightly obscured because the sensitivity to events for experiment 5 using holography was reduced by a thick coating of nail polish at the bottom of the wire, which increased its effective occlusion zone. Further experiments will be performed in the future to make a more complete local volume extent map for anodic currents.

It was also seen that for small angles ($< 6°$) with the wire before the central optical axis of the point source, light reflected from the face of the wire would contribute to the interference patterns. This could increase the sensitivity to small events, and suggests the possibility to perform new holography configurations that would allow direct imaging of the wire face while also being sensitive to solution effects. The presented data show that for maximum sensitivity to pitting events the polished face of the working electrode should be at or before the central optical axis with an angle $< 6°$.

2.5 Conclusions and Outlook

We have shown that the addition of concurrent DIHM to EMSI and microscopy helps to increase sensitivity to pitting events, to discriminate against corrosion types that we are not studying (such as crevice corrosion), and gives new ways to visualize the events. Point source Digital In-line Holographic Microscopy complements microscopy and EMSI well; it gives additional information about the electrolyte near the electrode/electrolyte interface, while maintaining spatiotemporal information about the
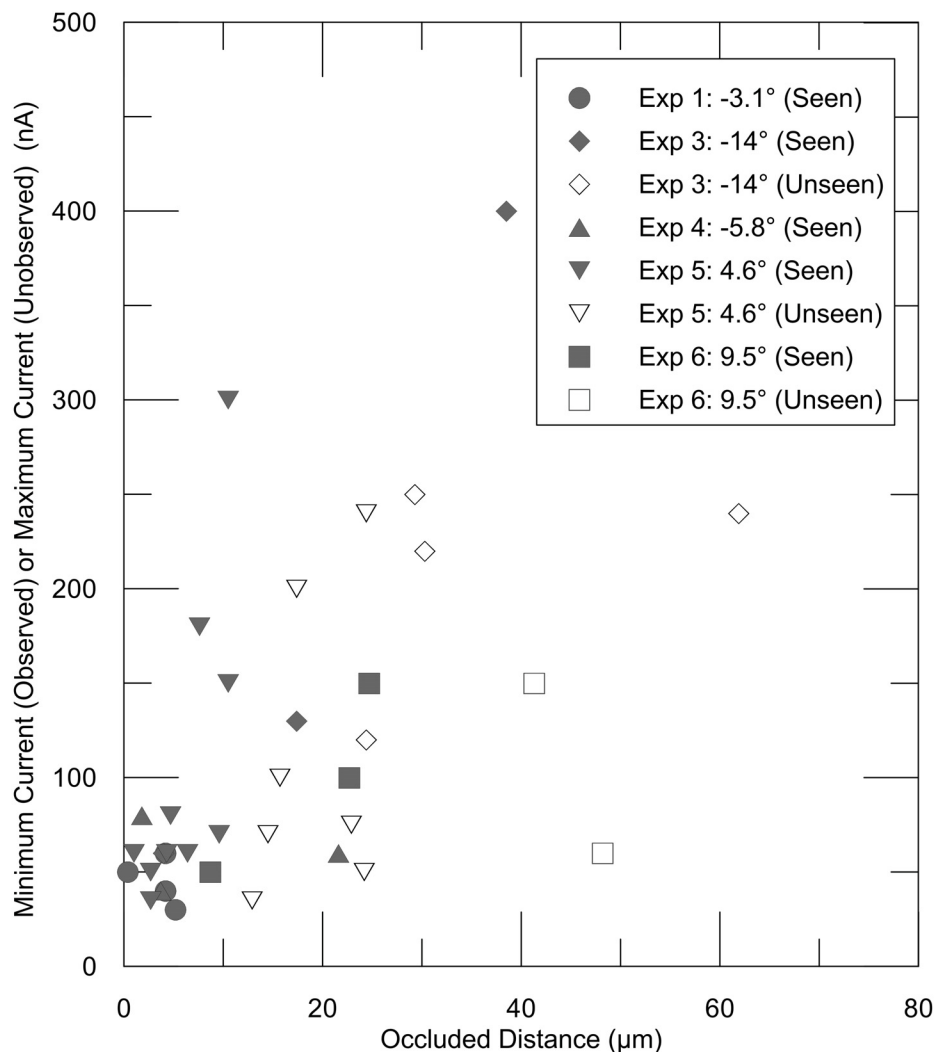
Figure 2.8: For events that occurred individually, the minimum current an event was detected at with DIHM reconstructions is plotted (shaded symbol) versus the occlusion distance. The occlusion distance from the face of wire is based on the shadow cast by the wire, so it is dependent on both the position of the event as observed with microscopy and EMSI and the angle before (negative angles) or beyond (positive angles) the central optical axis of the point source. If an event was observed with microscopy/EMSI but not holography, then the maximum anodic current associated with the event was plotted with an open symbol. For each individual experiment, the minimum current required to observe an event with holographic reconstructions increases with occlusion distance and there is a separation between seen and unseen events. The larger than expected anodic currents required to observe an event in experiment 5 could be caused by thick nail polish at the bottom of the wire, which would enhance the occluded zone.

wire face and the oxide layer using microscopy and EMSI. DIHM has also added the ability to track ejected particles from the sample surface through the electrolyte. Since these particles have been observed to originate at active pitting sites with microscopy and are emitted when the anodic current is increasing or just before sudden drops in anodic current, it is probable that they are pieces of the pit covers. In the future it may be possible to separate certain types of particles ejected from the sample using external fields and then retrieve them for chemical analysis. Since those objects can be traced back to their original pits at the surface, additional information about those pitting sites would be gained. In addition, the distortions of the fringe patterns in the holograms associated with pitting events and the lensing effects seen in the other two optical methods are evidence for local changes in the index of refraction in the volume at the pitting sites caused by enhanced ion concentrations. Using these holograms as interferograms one can estimate the change in the index of refraction and estimate the magnitude of these concentration enhancements.

DIHM is sensitive to changes in the solution associated with anodic currents as small as 25 nA; increasing the brightness for the point source may increase this sensitivity even further into the low nA range. The volume extent of this local change in index of refraction is dependent on the anodic current associated with a pitting event, as shown with the experiments where the wires were positioned before and beyond and the central optical axis of the point source. A more complete volume dependence of enhanced ion concentration on anodic current can be deduced in future experiments.

Combining DIHM with microscopy and EMSI has clearly increased the sensitivity to small metastable pitting events, and has created new opportunities to systematically analyze aspects of electrochemical systems that were previously inaccessible.

2.6   Acknowledgements

Chapter 3

Enhancing Resistance to Pitting Corrosion in Mechanically Polished Stainless Steel 316LVM by Water Treatment

Authors: P. E. Klages[1], Z. Bai[1,2], M. Lobban[1], M. K. Rotermund[1], H. H. Rotermund[1]

[1]Department of Physics and Atmospheric Science, Dalhousie University, 6310 Coburg Road, Halifax, Nova Scotia, B3H 4R2, Canada
[2]Boston Scientific, St. Paul, 4100 Hamline Avenue North, St. Paul, Minnesota 55112-5798 United States of America

3.1 Abstract

We present an extremely simple and environmentally friendly technique that appears to dramatically reduce pitting corrosion on stainless steel 316LVM. Mechanically polished SS 316LVM wire samples were treated in 90 °C high purity deionized water for different durations, then tested for pitting corrosion using potentiodynamic, potentiostatic as well as in situ imaging techniques. Wires treated for 2 or 3 h showed the greatest enhancement of pitting resistance when tested in 0.9 % (by mass) NaCl

solutions. To investigate the most plausible cause for the increased corrosion resistance, preliminary Scanning Electron Microscopy (SEM) and Energy Dispersive X-ray Spectroscopy (EDS) tests were performed on SS AISI 316L disks. We identified micron sized MnS inclusions on the polished disk surfaces. After treatments in heated high purity deionized water, SEM revealed micropits and EDS did not detect sulphur where MnS previously existed.

3.2   Introduction

The corrosion resistance property of stainless steel (SS) originates from the protective oxide film that spontaneously forms on its surface and acts as a barrier against aggressive diffusive molecules in the environment. Disruptions in this passive oxide layer lead to localized metastable pitting, which can lead to long-lived corrosion. These disruptions can include scratches, defects, grain boundaries and inclusions [4]. The idea that manganese sulphide (MnS) inclusions play a critical role as initiation centres for pitting corrosion on stainless steel goes back nearly 40 years [8, 101] and has continued into recent times [13, 16, 102].

The importance of MnS inclusions in pitting corrosion initiation has led to a variety of methods to remove them from the surface of stainless steels. Some of these methods include chemical surface treatments [54], and resurfacing using high current electron beams [52] and lasers [10]. In one set of experiments Virtanen *et al.* [55] used water as a control against their cerium solutions for location specific oxide treatments. They used low S stainless steel and were primarily interested in the oxide layer; they showed only minor changes in the oxide after treating samples in 90 °C water for 30 min, and did not discuss the water treatment further.

Our first investigations compared the pitting corrosion resistance of polished SS AISI 316LVM wires against polished wires treated in chemical baths or high purity deionized water at 90 °C for extended periods of time. Much to our surprise we found that the simple water treatment was more effective than any of the chemical

treatments we used at preventing pitting corrosion in 0.9 % (by mass) NaCl solutions. To verify those results and to ensure that the epoxy used to encase the thin SS wires was not somehow the cause of the increased corrosion resistance, new experiments with uncoated samples were performed. This paper describes those experimental results and includes some preliminary SEM and EDS results to elucidate the cause of the enhanced corrosion resistance.

3.3 Materials and Methods

3.3.1 Materials and Sample Preparation

This study was conducted using low carbon SS samples. Our samples were 0.381 mm (0.015 in.) diameter SS 316LVM wires (Smallparts Inc.) and 1.5 mm thick disks cut from a 19 mm (0.75 in.) diameter rod of SS 316L. From wavelength dispersive spectroscopy, the sulphur content was found to be as high as 0.07 % for the bulk in the wires; the sulphur content of the disks is 0.025 % (composition certificate from Outokumpu). All samples underwent mechanical polishing and cleaning before the start of the experiments. For mechanical polishing, the wires were mounted in larger stainless steel holders using Crystalbond adhesive. The wire faces were first ground flat with 53 μm grit SiC paper, then polished with successively smaller grit SiC paper to 15 μm, followed by 9, 3, and 1 μm diamond suspensions, creating a mirror-like finish. The wires were then removed from the holder and were cleaned prior to treatments by sonication in acetone, followed by rinsing with methanol or ethanol and deionized water. Microscopic inspections were performed to ensure no visible particles were left on the face of the wires. The wires were exposed to air and the stainless steel disks were stored in an Argon filled container before treatments.

3.3.2 Water Treatment

The samples were placed in a 500 mL glass container filled with high purity deionized water (18 MΩ cm^{-1} Nanopure), which was then placed in a temperature controlled

immersion bath (Thermo Haake C F3) at 90 °C (± 5 °C) for different durations (1 to 6 h). The samples were checked periodically for bubbles, and if any were found the samples were gently tapped to free the bubbles. Wires were held vertically in a Teflon holder, while the disks were unsupported and had their polished side facing upwards into the water.

3.3.3 Electrochemical Testing

To simulate the environment of implanted biomedical devices, a three-electrode electrochemical cell with 0.9 % (by mass) NaCl solution was used to test the corrosion resistance of the wires. A total of 17 new experiments, with wires treated in the heated high purity deionized water for 0, 1, 2, or 3 h, were performed to confirm our previous findings. A Ag/AgCl wire was used as the reference electrode, a Pt wire served as the counter electrode, and the polished stainless steel wire face was the working electrode. The sides of the wire were electrically insulated from the solution by carefully covering them with nail polish. The potential was increased from -400 mV with respect to the Ag/AgCl electrode to 100 mV at 10 mV/s, and held for 1 min. It was then increased in steps of 50 mV at a rate of 2 mV/s and held at each step for 1 min. The potential was increased to a minimum of +600 mV. Since our aim was to observe the onset of pitting, if no significant pits (>1 μA) occurred we would continue to increase the potential in either 50 mV or 100 mV steps above +600 mV.

To verify that pitting events occurred on the polished face, in situ optical techniques were employed. Contrast enhanced microscopy, ellipsomicroscopy for surface imaging (EMSI), and digital in-line holographic microscopy were used simultaneously. For a full description of these techniques, see [29,30,103]. Note that to accommodate these optical techniques, our electrochemical tests were done at room temperature instead of body temperature (37 °C) like our previous studies had used.

3.3.4 Scanning Electron Microscopy (SEM) and Energy-Dispersive X-ray Spectroscopy (EDS)

To investigate how the water treatment affects the stainless steel we decided to analyze the surfaces before and after the treatment. Instrumental constraints on the SEM/EDS machine made it unfeasible to measure the wire samples at this time. In order to address the problem, we chose to use three SS 316L disks with a diameter of 19 mm and 1.5 mm thickness. To reduce oxidation after the mechanical polishing, the disks were stored in an Argon filled container until the treatments could be performed. The samples were imaged with a Hitachi FE-SEM 4700, and for selected regions EDS elemental composition maps were created. After analyzing the samples, disk 1 was exposed to air for 2 weeks, while disks 2 and 3 were treated for 3 and 6 h, respectively, then stored in Argon again until the next SEM/EDS run was performed.

3.4 Results and Discussion

3.4.1 Potentiostatic Testing

A total of 17 SS wires were tested to see the effects of the water treatment on pitting corrosion. 6 wires were treated with 90 °C high purity deionized water for 3 h, 2 were treated for 2 h, and 2 were treated for 1 h. The 7 remaining polished wires were left untreated to compare against the treated wires. One of the wires treated for 3 h showed an increase of anodic current without any corresponding changes observed on the wire face using the in situ microscopy techniques; that data set was removed under the assumption that there was a scratch in the insulating coating on the wire.

We found that pitting resistance was best for those wires treated directly after polishing and cleaning. As a reference, all 7 untreated wires showed large current events (> 5 μA) below 600 mV and initial pitting occurred between 200 mV and 400 mV. In the same range for electric potentials, the wires treated for 3 h directly after polishing showed no anodic current above 35 nA and only 2 current events (possibly noise) occurred above our detection limit of 25 nA. The wires treated for

3 h but one or two days after polishing all exhibited pitting events > 500 nA below 600 mV, though no current event exceeded 3 μA below 600 mV. This shows that it is important to minimize the duration of exposure to air after mechanical polishing and before water treatments for the best pitting corrosion resistance.

To present typical experiments on a continuous time scale, we chose the worst case for treated wires and one of the best cases for untreated wires and plotted them together in Figure 3.1. The time scale for the untreated wire was shifted to line up the potential plots at early times. The untreated wire (black) shows the first metastable pitting event via an anodic spike at 350 mV; the magnitudes and frequency of events increased as time progressed with a maximum anodic current > 10 μA before 600 mV when we stopped the experiment. The wire treated for 1 h (light orange curve) has its first metastable pitting event at 450 mV and only four more events above 30 nA occurred before 800 mV, all of which had peak anodic currents below 820 nA. Above 800 mV large pitting events occurred and the experiment was stopped at 900 mV.
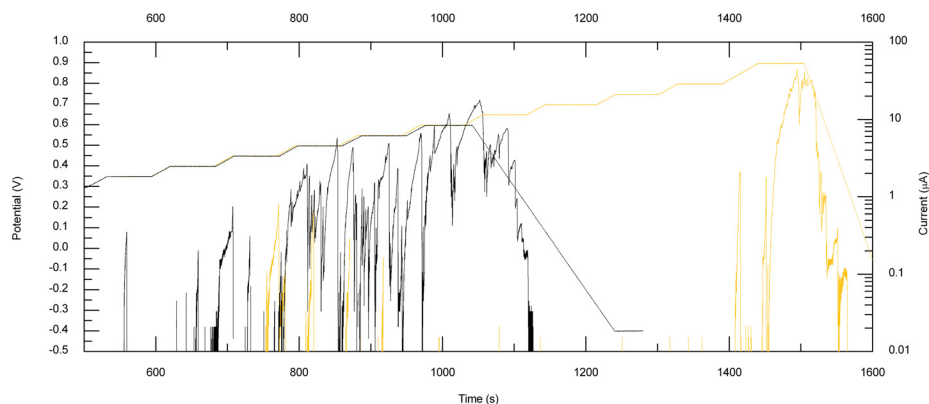
Figure 3.1: A plot of potential versus time and current versus time for the worst case of treated wires (June 17, light orange) and one of the best cases for untreated wires (May 17, black).

We also tested the effect of water treatment duration on pitting corrosion resistance for wires treated directly after polishing and cleaning. Figure 3.2 (top) compares wires treated for 1, 2, or 3 h directly after polishing and cleaning. Wires treated for 2 or 3 h showed better pitting resistance in the NaCl solution, having higher initial

pitting potentials and lower anodic currents associated with events than wires treated for 1 h for the same electric potential range. However, the difference between any of the treated samples compared to the untreated samples is striking. Figure 3.2 (bottom) shows that all untreated samples developed major pitting events between 400 and 560 mV, with some already starting at 300 mV. In contrast, the best of the 3 h treated samples reaches 1000 mV before the anodic current associated with pitting events exceeded 50 nA. The plots shown in Figure 3.1 are included in Figure 3.2 (top, bottom) using the same colour scheme.
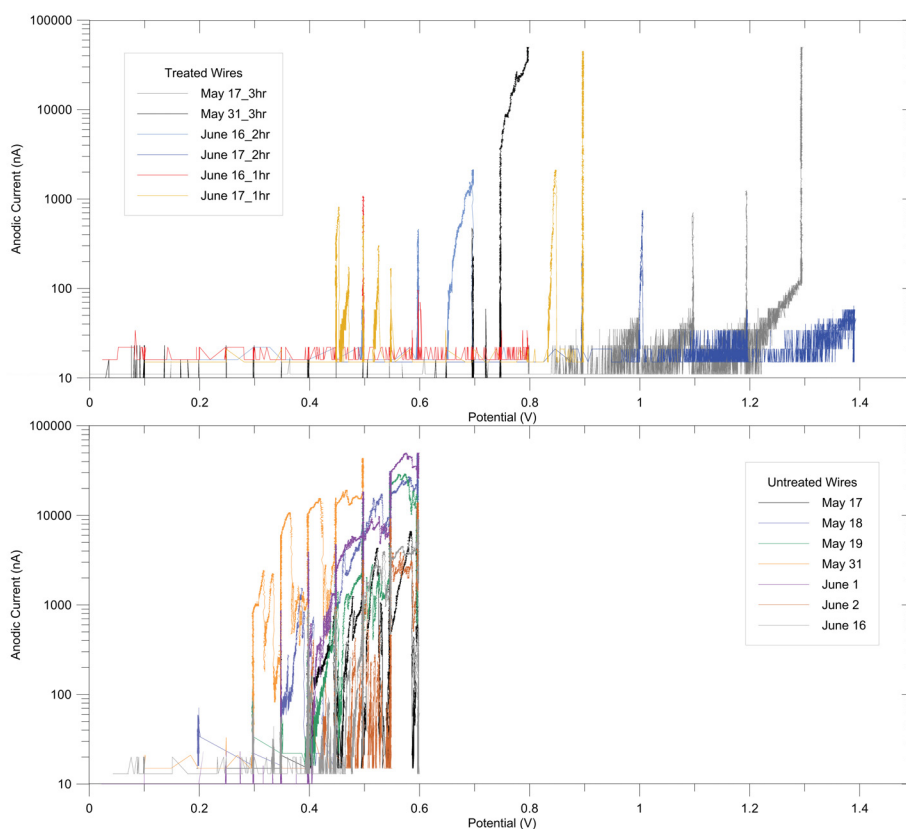
Figure 3.2: Forward scan anodic current versus electric potential plots for treated (top) and untreated (bottom) wires. (Top) 2 plots for each water treatment length: 1 h (red and orange), 2 h (blue and cyan), and 3 h (black and gray). The initial pitting potential increased for treated wires and the total current associated with events decreased. (Bottom) Plots for 7 untreated wires. Initial pitting started as low as 200 mV.

These results are in good agreement with our preliminary results using the epoxy-encased wires. Those experiments showed no pitting on treated wires below 550 mV for potentiodynamic testing, with only 2 of the 9 wires transitioning directly to stable pitting below 1000 mV.

3.4.2 SEM and EDS

As a first test to elucidate the effect of the high purity deionized water at 90 °C on stainless steel, we imaged and analyzed the surfaces of 3 mechanically polished disks before water treatments, using SEM and EDS techniques. 15 regions (125 μm × 90 μm) were imaged with SEM, and on average roughly 50 dark spots between 0.1 μm and 5 μm in their largest dimension could be detected in each of the images. We randomly magnified 3 areas that included a few dark surface spots and created EDS chemical composition maps. The upper half of Figure 3.3 shows a region with six dark spots in the SEM image and the corresponding EDS composition maps for that region. Increased Mn and S (or Mo) concentrations were observed at positions corresponding to the dark surface marks. S and Mo cannot be differentiated well based on their X-ray spectra alone, but since MnS inclusions are common in stainless steels, the dark spots were assumed to be MnS. The resolution of the EDS composition maps precluded any ability to observe FeS, which often surrounds MnS inclusions [16].

After two of the disks underwent water treatments and the third was allowed to oxidize in air, they were again imaged using SEM and EDS techniques. Distinct differences between the untreated disk and the treated disks were clearly visible in SEM images. The untreated disk appeared unchanged despite the exposure to air; the typical MnS inclusions were observed across the surface. However, the two disks treated in 90 °C water for 3 h and 6 h, showed small crevices instead of the usual inclusions. Since sulphides occupy less than 1 % of the surface area, even with low solubilities this result is plausible. The lower half of Figure 3.3 shows an SEM image of a region including 6 of these crevices and the corresponding composition maps. The EDS images at these sites reveal that no S remains at these excavated sites,
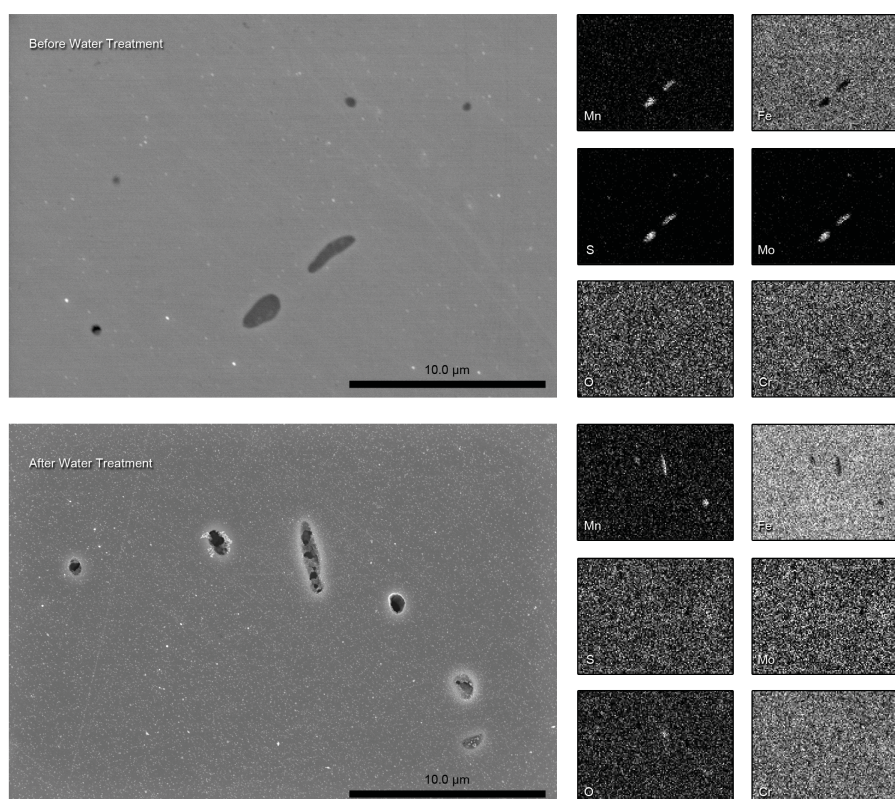
Figure 3.3: SEM (left side) and EDS (right side) for a SS sample. Each composition map is normalized to its largest signal which is shown as white. Upper half: Untreated sample. The dark gray regions, as seen with the SEM, show enhanced Mn and S (or Mo) concentrations in the composition maps. Lower half: After 3 h water treatment. The crevices show no enhancement for S (or Mo) though there is still some Mn for the larger crevices, as well as some O, which was not present at inclusions before treatments.

while some Mn is still detectable, and some O is present at the larger crevices with the Mn.

3.5 Conclusions

Our data shows that when SS 316LVM is mechanically polished and then treated in high purity deionized water at 90 °C, it has better pitting corrosion resistance in NaCl solutions. Our potentiostatic and previous potentiodynamic experiments demonstrate that the onset potential, number of pitting events and magnitude of anodic current

decreased dramatically for the treated wires. Preliminary SEM and EDS investigations showed that the MnS inclusions were largely eliminated, and this is the most likely cause for the increased pitting resistance in the NaCl solution. Additional work optimizing the treatment duration and temperature as well as testing the efficacy of this treatment with other stainless steel types and in different concentration NaCl solutions is in progress. For future SEM/EDS tests the same wire samples will be used allowing us to image identical regions before and after treatment because the areas of the wire faces are much smaller. This will then present a clear-cut argument for the cause of the major improvements that we have observed for pitting corrosion resistance after water treatments.

3.6 Acknowledgements

Chapter 4

Increased Resolution in Convolution Based Hologram Reconstructions Using Subpixel-Sized Shifts of the Impulse Response Function

Author: Peter E. Klages

Department of Physics and Atmospheric Science, Dalhousie University, 6310 Coburg Road, Halifax, Nova Scotia, B3H 4R2, Canada

4.1 Abstract

Convolutions can be used to reconstruct holograms using the Rayleigh-Sommerfeld diffraction integral without approximations, and the Kirchhoff-Fresnel diffraction integral with approximations only in the obliquity factor, but have the same pixel spacing as the sampled hologram for a single reconstruction. Multiple reconstructions at a single plane with subpixel-sized shifts of the impulse response function can be performed to increase the reconstruction resolution; for n subdivisions, $(n + 1)^2$ reconstructions are required. To reduce the computational time, parallel processing via graphical processing units has been employed: 4 megapixel holograms are reconstructed with sub-wavelength pixel spacing ($n = 15$) in 17 s.

4.2   Content

Holography, invented by Gabor [58], is a technique in which a complex wavefront is recreated from a 2D interference pattern using *a priori* knowledge of the coherent reference wave that was used in the recording process. The advantage of recording holograms (interference patterns) over in-focus images is that the reconstructed wavefront contains information about an entire volume and can be analyzed *ex situ* for different applications. Thus holographic microscopy, the subject of this letter, allows analysis that would otherwise be impossible with conventional imaging: moving and/or living organisms can be imaged and tracked, microfluidic experiments can show flow patterns around irregular 3D objects, and changes in the index of refraction can be detected, as just a few examples [42, 76, 79, 104, 105].

The hologram intensity, I, created by the interference between a reference wave and elastically scattered light, can be written as:

$$I = U_{ref}^2 + U_{ref}U_{scat}^* + U_{ref}^*U_{scat} + U_{scat}^2 \tag{4.1}$$

where U_{ref} and U_{scat} represent the complex reference and scattered waves, respectively, and * denotes that the complex conjugate is to be used. If the amplitude of the scattered wave is small compared to the reference wave, then the fourth term on the right-hand side is negligible and the recorded holograms can be used in conjunction with diffraction integrals to numerically reconstruct the volume. To remove the effects of the source from the reconstructions, it is common to subtract the intensity map created by the reference wave alone, or, in the case of moving objects, to subtract another hologram from the time sequence of holograms. Subtracting the reference wave has the additional bonus of removing static camera noise in experimental setups.

Numerical reconstructions of the complex wavefront at different planes can be performed using the angular spectrum approach to wave propagation, or either the Kirchhoff-Fresnel (KF) or Rayleigh-Sommerfeld (RS) diffraction integrals. Sherman [82] has shown that the angular spectrum approach, while it appears to be different, is

actually equivalent to the RS diffraction integral, so only the KF and RS integrals will be discussed in this letter. The RS solution uses different boundary conditions from the KF solution, and was derived in part to overcome mathematical inconsistencies found in Kirchhoff's solution [56, 57], but the fact that the solution is for an aperture in an infinite conducting sheet could make the solution less relevant to experimental holographic setups. Despite the differences in the derivations, the resulting diffraction integrals, as discussed in detail by Born and Wolf [57] and Goodman [56], are almost identical when the distance to the aperture is much greater than the wavelength of light. These integrals differ only by an obliquity factor based on angles to positions on the aperture from the source and the scattering positions; the form that these integrals take is:

$$U(\mathbf{r}) = \frac{1}{i\lambda} \int \int I(\boldsymbol{\xi}) \frac{\exp[ik(|\boldsymbol{\xi}| + |\boldsymbol{\xi} - \mathbf{r}|)]}{|\boldsymbol{\xi}||\boldsymbol{\xi} - \mathbf{r}|} \psi dX dY \tag{4.2}$$

where the origin is co-located with the point source reference, $U(\mathbf{r})$ is the complex wave at point $\mathbf{r} = (x, y, z)$, $k = 2\pi/\lambda$ and λ represents the wavelength of light, $\boldsymbol{\xi} = (X, Y, Z)$ is a location on the aperture, and ψ represents the obliquity factor for the diffraction formula. The obliquity factors are:

$$
\begin{aligned}
\text{KF} &: \quad \psi = \tfrac{1}{2}\left[\cos(\boldsymbol{\xi}, \hat{\mathbf{k}}) + \cos(\boldsymbol{\xi} - \mathbf{r}, \hat{\mathbf{k}})\right] \\
\text{RS I} &: \quad \psi = \cos(\boldsymbol{\xi} - \mathbf{r}, \hat{\mathbf{k}}) \\
\text{RS II} &: \quad \psi = \cos(\boldsymbol{\xi}, \hat{\mathbf{k}})
\end{aligned}
\tag{4.3}
$$

where $\hat{\mathbf{k}}$ is the unit vector normal to the aperture. In the paraxial limit, these obliquity factors are all ≈ 1.

To reconstruct a recorded hologram, the recording screen takes the place of the aperture and the general diffraction equation 4.2 is modified so that the complex conjugate of the reference wave is used [90]:

$$U(\mathbf{r}) = \int \int I(\boldsymbol{\xi}) \underbrace{\frac{\exp(-ik|\boldsymbol{\xi}|)}{|\boldsymbol{\xi}|}}_{\text{complex source}} \underbrace{\frac{\exp(ik|\boldsymbol{\xi} - \mathbf{r}|)}{i\lambda|\boldsymbol{\xi} - \mathbf{r}|}}_{\text{impulse response}} \psi dX dY \tag{4.4}$$

Since the obliquity factor of the KF form of this integral is dependant on the cosines of both the reference and impulse response vectors, it can only be solved exactly by evaluating $U(\mathbf{r})$ explicitly for every $\mathbf{r}$. However, if the obliquity factor is dependant on only $\boldsymbol{\xi}$ or $(\boldsymbol{\xi} - \mathbf{r})$ then convolutions can be used to evaluate 4.4 for an array of points simultaneously [82, 85, 90]. Thus $U(\mathbf{r})$ can be solved exactly for the two RS integrals and approximately for the KF integral using convolutions (for KF one must assume that $\cos(\boldsymbol{\xi}, \hat{\mathbf{k}}) = 1$).

Each individual convolution solution is a subset of the possible solutions found by explicitly calculating equation 4.4, with pixel spacing for each reconstruction equal to the recorded hologram. Since recorded holograms have pixel spacing on the order of 6 μm, individual reconstructions have limited usefulness for microscopy. To increase the resolution in a single convolution reconstruction, one can use geometric magnifications, or decrease the pixel spacing in the hologram by resampling or by using different sensors [90]. Each of these methods has its own issues, however. Geometric magnifications use reference waves that differ from the true reference wave and introduce distortions into the reconstructions, and resampling the hologram creates smoother gradients from pixel site to pixel site while the true pattern with more, smaller pixels, would be more complex. Reducing the pixel spacing would help, but only if more pixels were also added, since the ultimate resolving limit for a reconstruction, based on the point-spread function taking the form of the Fraunhofer diffraction pattern of the aperture, is:

$$\Delta x_{resolved} = 2\lambda(Z - z)/a \qquad (4.5)$$

where $Z - z$ is the distance from the reconstruction plane to the hologram plane and a is the physical width of the hologram.

To create higher resolution reconstructions without geometric magnifications or resampling the recorded hologram, I propose that multiple convolution reconstructions in the same plane with subpixel-sized (*i.e.* non-integer) lateral shifts of the impulse response function should be performed. Integer pixel-sized lateral shifts have

been discussed in the context of creating a larger field of view for macroscopic sized objects and it was noted that any lateral shift in a space invariant system is valid [85]. Subpixel-sized lateral shifts make the impulse response function array non-symmetric and have a large enough effect on the phase term of the complex exponential in equation 4.4 that the full informational content of the hologram can be realized. For n additional equally spaced subpixel shifts performed in both the x and y directions, $(n + 1)^2$ reconstructions at a single reconstruction plane are required to build the high-resolution reconstruction without making approximations to the integral, decreasing the pixel size, or resampling the hologram (see Figure 4.1).
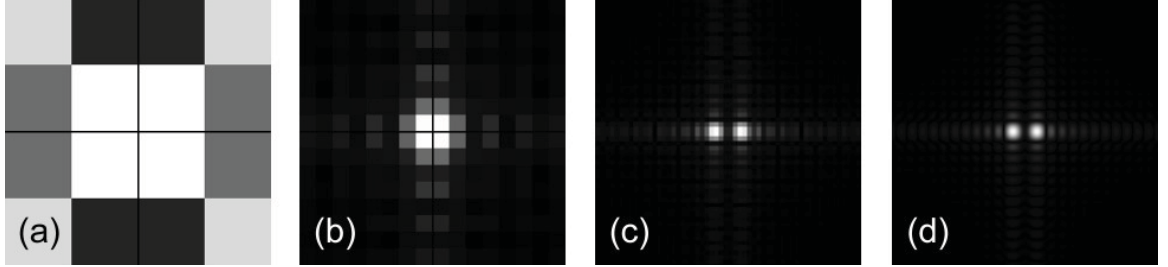
Figure 4.1: Reconstructions (normalized to the largest amplitude) of a 2048 × 2048 pixel hologram of 2 simulated point sources separated by 1.88 μm, with source to object (SO) distance = 5 mm, λ = 406 nm, and source to screen (SS) distance = 33.5 mm. Each image is 24 μm × 24 μm. (a) single convolution solution: lateral pixel spacing $\Delta x_{recon} = \Delta x_{holo} = 6$ μm. (b) 4×4 convolution reconstructions interleaved: $\Delta x_{recon} = 1.5$ μm. (c) 16×16 convolution reconstructions interleaved: $\Delta x_{recon} = 375$ nm. (d) 64×64 convolution reconstructions interleaved: $\Delta x_{recon} = 93.75$ nm.

Because no approximations are made (except for the obliquity term in the KF form of equation 4.4), the region where this method is valid extends almost to the recording screen. With in-line holographic microscopy this method complements the reconstruction method used by Kreuzer *et al.*, which uses a Dot Product (DP) approximation to the path-length difference in the complex exponentials of equation 4.4 [65, 76, 79, 106]. For errors in the path length difference $\leq \lambda/4$,

$$|\mathbf{r}| \leq (\lambda|\boldsymbol{\xi}|/2)^{1/2} \tag{4.6}$$

When $|\mathbf{r}|$ surpasses this value the hologram will still reconstruct; objects will, however,

be 'in-focus' farther from the source than they should be and will become increasingly distorted and magnified. Figure 4.2 demonstrates this, using reconstructions of simulated holograms of two point sources separated as per equation 4.5 for a variety of source-to-object distances, and compares the DP approximation to the exact/interleaved convolution solution. Figure 4.3 shows reconstructions of a hologram of a real object, a wire with a physically measured diameter of 381 μm; the diameter measures 413 μm using the DP approximation, and 382 μm using the convolution method with subpixel-sized shifts. These figures show that for experimentally feasible setups, commonly used approximations in holographic microscopy can give inaccurate results; however, the cost for more accurate reconstructions is increased computational time.
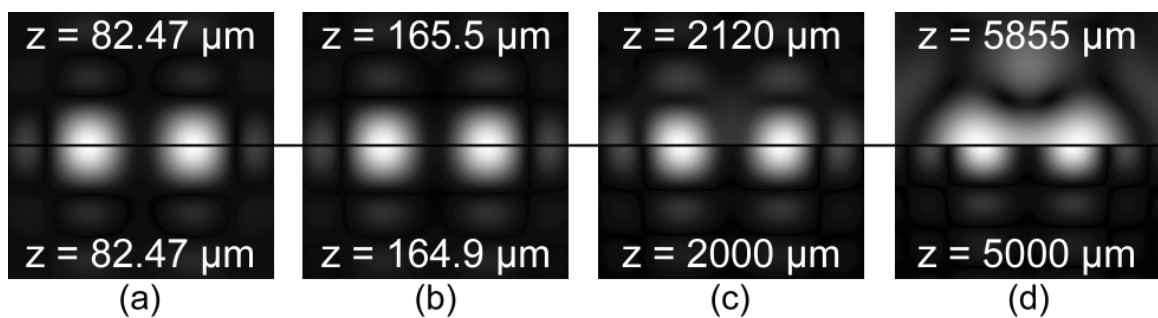
Figure 4.2: Dot product approximation reconstructions (top) and exact/interleaved convolution reconstructions (bottom) (SS = 33.5 mm, λ = 406 nm). In (a), equation 4.6 is fulfilled; the DP approximation is essentially identical to the exact solution. As this requirement is exceeded, the 'in-focus' object distance increases and distortions occur. (a) SO distance = 82.47 μm: $\lambda/4$ error in DP approximation. (b) SO = 164.9 μm: λ error in DP approximation. (c) SO = 2000 μm. (d) SO = 5000 μm.

To reduce the computational time, graphical processing units (GPUs) are used to compute the reconstructions in parallel. CUDA, by nVidia, is a parallel programming platform that allows functions to be programmed easily in a C-like language. Highly optimized functions like discrete Fourier transforms have performance gains on the order of 10$\times$ for an nVidia Tesla c1060 card compared to a quad-core CPU. Other methods can see significantly greater gains, however: the explicit evaluation of equation 4.4 for 2048 $\times$ 2048 reconstruction points from a hologram with 2048 $\times$ 2048 pixels takes $\sim$ 1 hr with the GPU, compared to 1 week computing with a
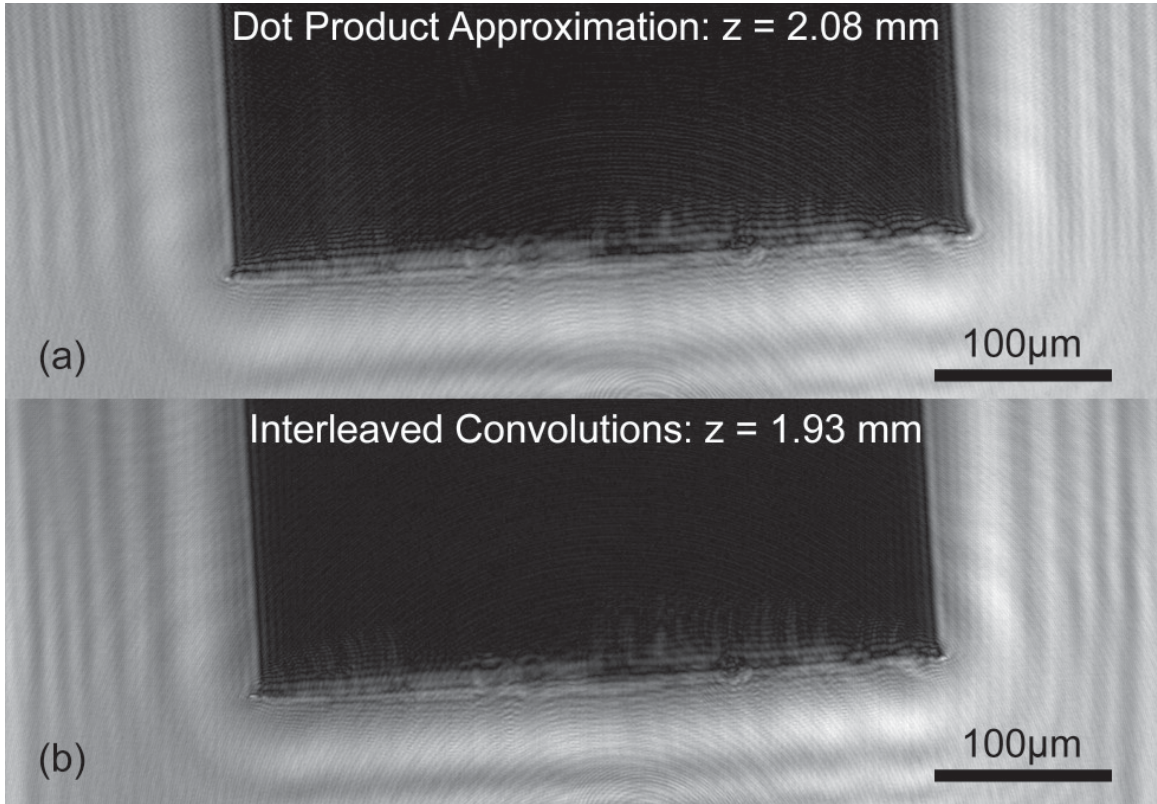
Figure 4.3: Comparison of reconstructions using the DP approximation (a) and the exact/interleaved convolution method (b) for a 381 μm wire (SS = 33.5 mm, λ = 406 nm). In (a) the wire reconstructs at z = 2.08 mm and measures 412 μm. In (b) the centre of the wire reconstructs at z = 1.93 mm with wire diameter = 382 μm.

quad-core CPU. The DP approximation, with user chosen Δx_{recon}, takes $\sim$ 60 ms for the same size reconstruction. Each individual convolution reconstruction takes $\sim$ 10 ms since less preprocessing is required. If 15 additional shifts are made for 6 μm pixels, then the final lateral pixel spacing in the combined reconstructions will be 6 μm/16 = 375 nm, and 256 individual reconstructions will need to be performed. The final resolution would be (2048$\times$16)$\times$(2048$\times$16)), but only a subset of this reconstruction plane, again with dimensions measuring 2048 $\times$ 2048 pixels, is retained. The complete time to reconstruct, including interleaving the results from individual reconstructions using the convolution method takes $\sim$ 17 s if the hologram is zero padded to 4096 $\times$ 4096 pixels and the impulse response function is constructed at 4096 $\times$ 4096 pixels (so that every pixel in the hologram will be used), or $\sim$ 5 s if

everything is left at 2048×2048 pixels. This reconstruction time is already almost short enough to use the convolution method exclusively if accuracy is paramount. The newest GPUs released this year have approximately $7\times$ more processors, faster on-board ram, and faster transfers to and from the main computer memory, which should create speedups on the order of 1 magnitude or more.

The greatest benefit to using the convolution approach, however, is that the clarity of the math in equation 4.4 is retained. Because of this, reconstructing holograms that are recorded off-axis or at an angle to the central optical axis, as well as shifting the reconstruction region for off-line holographic setups are straight-forward; simulations have already been tested and experiments will follow. The only limitations to this method are that the obliquity factor can only be dependent on either the reference wave or the impulse response function and the reconstruction planes must be parallel to and, individually, the same size as the recorded hologram. This method, computationally feasible now with the advent of multi-processor GPUs, shows great promise as a tool for accurate reconstructions of holograms.

4.3 Acknowledgements

Chapter 5

Conclusions and Outlook

The projects presented here have shown a novel use of optical techniques to gain additional information about metastable pitting and the solution nearby *in situ*, have shown a simple technique to improve the pitting resistance of SS 316LVM when exposed to simulated biological solutions, and have developed methods to reconstruct holograms quickly and without approximations.

Using optical microscopy, EMSI, and DIHM simultaneously, it has become possible to acquire high resolution images of the pits as they form, to obtain qualitative information about nanometer changes in the protective passive layer, and to image the volume of solution adjacent to the corroding surface with micrometre resolution. This also enables one to track particles emerging from pits and facilitates their collection after the experiments have concluded.

In an effort to enhance the pitting corrosion resistance of SS 316LVM when it is exposed to simulated biological solutions, wires were polished to remove the passive layer then immersed in 90 °C nanopure water for several hours. This simple surface treatment yields a great enhancement in pitting resistance. Untreated samples exhibit initial pitting at potentials ranging from 200 to 400 mV (with respect to a Ag/AgCl reference wire), while initial pitting potentials for treated samples range from 600 to 1000 mV and the number and frequency of pitting events also decrease. Tests using SEM and EDS have shown that removal of sulphide inclusions is the most probable cause for this enhanced pitting resistance. These results could have a profound impact on how stainless steels are treated, especially for medical applications.

Having physically added DIHM to the set of optical techniques for *in situ* pitting corrosion studies, it became imperative to increase the software performance to allow

real-time analysis. Utilizing GPUs has increased reconstruction rates from ~ 1.7 frames per second (fps) to more than 10 fps. This not only reduces the time required to process the tens of thousands of holograms recorded per experiment, but can also change the way one approaches a holographic experiment. Reconstructing holograms live (in real-time as one acquires the holograms) allows one to interactively adjust the experimental parameters for optimal reconstruction quality.

With the newfound computational power available from GPUs, methods to calculate the Kirchhoff-Fresnel and Rayleigh-Sommerfeld integrals quickly, exactly (except for approximations in obliquity factors), and at arbitrary resolutions were also developed. To obtain 0.375 μm pixel spacing in reconstructions from holograms with 6 μm pixel spacing, 16×16 individual shifted convolution reconstructions must be calculated and interleaved. When 2048×2048 pixel holograms are padded up to 4096×4096 pixels it takes 17 s with a Tesla c1060 GPU; new hardware should decrease that time by a factor of approximately 10. This shows that we are approaching a period in time when it will no longer be necessary to use approximations to compute holographic reconstructions in a reasonable amount of time. Of course, using approximations will continue to have tremendous value in regions where they are valid since before long hardware improvements will allow near real-time navigable volume reconstructions. However, for regions and configurations where the approximations do not hold, it will be possible to apply the full methods without great time penalties.

Regarding the *in situ* techniques, the sensitivity of holography to changes in the index of refraction of the solution allows one to detect metastable pitting events with anodic currents on the order of 10 nA. This detection efficiency is already better than the sensitive EMSI and microscopy techniques and it is possible that the sensitivity limits can be increased for DIHM. However, to test the limits further, noise levels in the anodic current measurements must first be reduced by shielding the apparatus using a Faraday cage.

More sensitive anodic current measurements along with additional holographic studies would allow one to obtain more precise and accurate measurements of the

volume of solution affected by pitting events of different anodic current magnitudes. The convolution based reconstruction method should be used for these experiments since they require the camera position to be offset from the central optical axis. Also, automated video and potentiostatic data processing (pit occurrence, location, duration, and whether it is detectable with the various optical and potentiostatic techniques) should be developed before experiments are continued.

The sensitivity of holography to changes of the index of refraction in the solution has shown the possibility of misinterpreting EMSI data, since changes in the optical path also affect EMSI. Hence, additional experiments to test the extent of the effects caused by changes of the index of refraction should be performed, to verify that passive layer changes are the dominant features observed by EMSI.

While our experiments show that the water treatment technique generally enhances the resistance to pitting corrosion in 0.9 % by mass NaCl solution, occasionally a sample will pit at comparable potentials to untreated samples. If the removal of sulphides is the correct mechanism to explain the increased pitting corrosion resistance, then incomplete removal of inclusions would create a micropit or crevice with an inclusion at the bottom that would pit at comparable or even lower potentials than polished untreated samples. Future work along these lines has begun and includes the systematic variation of treatment parameters including ratios of surface area treated to volume of water, changing the nanopure water periodically, treatment duration, and the temperature of the water. The effects of these variations on the resulting states (passive layer thickness and development, the remaining number of inclusion sites, whether pitting resistance continues after abrasion following treatment, etc.) are being studied to gain a better understanding of how this treatment works and to optimize the treatment.

Computationally, the initial goal of reconstructing 10 fps has been achieved by optimizing the logic of the code and by using GPUs. However, there is still room for additional code optimization, and GPU technology continues to improve. Additional code optimization could include minimizing communication between the CPU and

GPU (since memory transfers are generally a bottleneck in the reconstruction algorithm) and tuning individual kernels. Kernels (the subprograms that run in parallel on the GPU) should be tuned so that the number of code branches are minimized ('if statements' require sections to be run multiple times), compute core occupancy is high, and memory transfers are coordinated properly. Since basic optimizations have already been performed, buying new hardware is the simplest way to further improve reconstruction speeds. Reconstruction speeds using CUDA are highly dependent on both the GPU specifications and the memory bus system used, and the computer gaming industry keeps the costs very reasonable. Consumer graphics cards currently range from less than \$50 for a card with 48 CUDA compute cores to \$600 for the newest consumer graphics card with 1536 compute cores. GPUs made specifically for scientific computing cost more than \$2000 per unit, but include error correction code (ECC) for the memory, are better suited for double precision floating point math, and generally have more RAM.

As camera sensors increase in size, additional optimization of the code for memory usage on the CUDA cards may also become important. Consumer cameras, such as the single lens reflex Sigma SD1 Merrill boast 15 MPixel resolutions for each colour channel (red, green, and blue) with 5 μm pixels [107]. The Foveon technology uses stacked pixels to record images, so the sensor will act like 3 separate monochrome cameras, each most sensitive to a different wavelength [108]. If the raw files can be interpreted easily, this consumer camera shows great promise for digital holography because of the resolution provided for the cost. When zero-padded correctly for convolution reconstructions, the holograms from this camera will be 8192 × 8192 pixels. With 4 GB RAM on a GPU, 8192 × 8192 arrays are the limit for the FFT routines currently used; however, with careful memory management it might be possible to reconstruct arrays as large as 16384 × 16384 pixels or larger with the same hardware. Reusing memory will slow down reconstructions since additional memory transfers will be required, but with the ever-increasing compute power available with GPUs this might not be an issue.

With regards to the convolution reconstruction approach with subpixel-sized shifting, computational speeds should increase with new GPUs and additional holographic geometries applicable to pitting corrosion studies could be investigated with no extra computational costs. Additional holographic geometries include rotations of the imaging sensor, shifted sensor positions, and off-line holography. Single beam off-line holography, where the imaging sensor and the object being imaged are moved in opposite directions from the central optical axis within the cone of light emanating from the point source, has already been tested in simulations and physically (in a preliminary way) on polished wires (see Figure 5.1). With this method the entire wire face could be imaged while remaining sensitive to changes in the solution associated with the pitting events. Future pitting corrosion studies might be able to incorporate this technique, however the best configurations need to be determined and the cuvettes may need to be redesigned to minimize reflections.
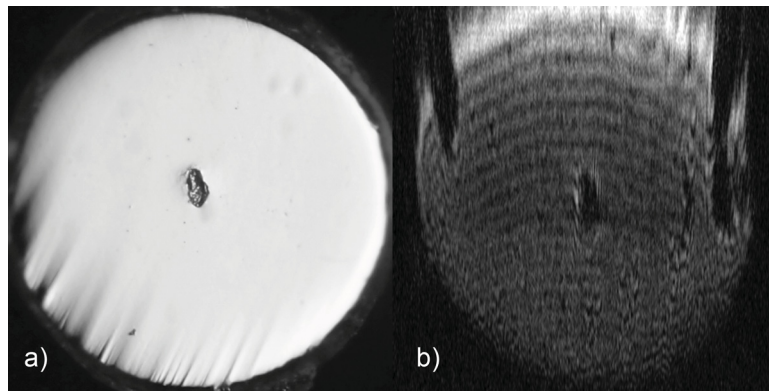
Figure 5.1: (a) A microscopic image of a SS 316LVM wire (diameter 381 μm) mechanically dented in the centre and (b) the results of one of the first single beam off-line holographic reconstruction tests. The offset of the wire from the central optical axis was ~ 0.5 mm and the offset of the camera (in the opposite direction) was ~ 7.7 mm. The centre of the wire was 2 mm above the point source and the camera was 34.8 mm above the point source. To visualize the wire face, a stack of reconstructions was created and the stack was then rotated. The wire face was cleaned after the hologram was recorded and before the microscopic image was taken, so the dark marks at the edges in the hologram reconstruction were most likely caused by surface contaminants.

During the time spent completing this body of work, custom image acquisition

software was also created and integrated into the reconstruction software for the Windows XP 32 bit operating system. This software allows the user to specify the hologram acquisition rate arbitrarily, and timestamps the files accordingly. By using a timestamp method, any system lags or acquisition problems can be accounted for in analysis. It was used by S. K. Jericho *et al.* for their underwater holographic microscopic experiments in the Canadian High Arctic [109]. New programmers at Resolution Optics used updated drivers to incorporate the acquisition software into the Windows 7 (32 and 64 bit) version of their reconstruction software suite.

The three projects shown here have involved theoretical, computational, and experimental aspects. On the theoretical side, comparisons between the full and approximate expressions for holographic reconstructions have been made, showing when it is necessary to use the full Kirchhoff-Fresnel integral for reconstructions. Computationally, methods to calculate the full expression in reasonable periods of time have been made: for reconstructions of 2048×2048 pixel holograms to 2048×2048 pixels it takes 1 hour for the full expression with arbitrary reconstruction positions and screen placements, 22 minutes for the full expression with on-axis symmetry, and 17 s for convolution based reconstructions composed of 256 individual reconstructions (performed on 4096×4096 pixel arrays) and applicable to a variety of geometries. Additionally, Kreuzer's patented algorithm using the dot product approximation has been refined and optimized to the point where more than 10 reconstructions per second can be made using consumer grade GPUs. This code has also been integrated into a commercial software package by Resolution Optics, in which holograms can be reconstructed during acquisition at a rate of 7 fps, the maximum acquisition rate for the camera included with their product. On the experimental side, a new optical method for detecting metastable pitting sites and the local changes in the surrounding solution has been developed using simultaneous *in situ* DIHM, EMSI, and contrast enhanced microscopy. Changes in the index of refraction of the solution for events as small as 10 nA can be detected. The ability to track material ejected from the active pits on the working electrode throughout the solution should facilitate the collection and

identification of this material in the future. Finally, treatments of SS 316LVM with 90 °C nanopure water have shown a great pitting corrosion resistance enhancement over untreated samples. Treated samples pit at higher potentials, and the number and frequency of pitting events is lowered. This simple technique should have great importance for medical implant materials, especially as it is refined in the future. All three of these aspects: theory, computation, and experiment, were essential for the successful development of the simultaneous *in situ* real-time microscopic techniques used for corrosion testing of SS 316LVM.

Bibliography

[1] H. M. Cobb, *The History of Stainless Steel.* Materials Park, OH: ASM International, 2010.

[2] J. Beddoes and J. G. Parr, *Introduction to Stainless Steels.* Materials Park, OH: ASM International, 1999.

[3] P. Monnartz, "Beitrag zum studium der Eisenchrom Legierungen unter besonderer berücksichtigung der säurebeständigkeit; Contribution to studies of iron-chromium alloys with special attention to acid resistance," *Metallurgie*, vol. 6, pp. 161–176, March 1911.

[4] G. S. Frankel, "Pitting corrosion of metals: A review of the critical factors," *Journal of the Electrochemical Society*, vol. 145, no. 6, pp. 2186–2198, 1998.

[5] R. C. Newman, "2001 W. R. Whitney Award Lecture: Understanding the Corrosion of Stainless Steel," *Corrosion*, vol. 57, no. 12, pp. 1030–1041, 2001.

[6] M. Pourbaix, L. Klimzack-Mathieiu, C. Mertens, J. Meunier, C. Vanleugenhaghe, L. de Munck, J. Laureys, L. Neelemans, and M. Warzee, "Potentiokinetic and corrosimetric investigations of the corrosion behaviour of alloy steels," *Corrosion Science*, vol. 3, no. 4, pp. 239–259, 1963.

[7] R. J. Brigham and E. W. Tozer, "Temperature as a pitting criterion," *Corrosion*, vol. 29, no. 1, pp. 33–36, 1973.

[8] G. Wranglen, "Pitting and sulfide inclusions in steel," *Corrosion Science*, vol. 14, no. 5, pp. 331–349, 1974.

[9] Z. Szklarska-Smialowska, *Pitting and Crevice Corrosion.* NACE International, 2005. Knovel e-version.

[10] J. Stewart and D. E. Williams, "The initiation of pitting corrosion on austenitic stainless-steel: On the role and importance of sulfide inclusions," *Corrosion Science*, vol. 33, pp. 457–474, March 1992.

[11] T. Suter and H. Bohni, "A new microelectrochemical method to study pit initiation on stainless steels," *Electrochimica Acta*, vol. 42, no. 20-22, pp. 3275–3280, 1997.

[12] T. Suter, H. Bohni, J. R. Gray, J. Alameda, and R. C. Alkire, "Pit initiation at single sulfide inclusions on stainless steel," in *Critical Factors in Localized Corrosion IV: A symposium in Honor of the 65th Birthday of Hans Bohni*

(S. Virtanen, P. Schmuki, and G. Frankel, eds.), (Pennington, NJ, USA), pp. 1–15, Electrochemical Society Inc, 2003.

[13] M. P. Ryan, D. E. Williams, R. J. Chater, B. M. Hutton, and D. S. McPhail, "Why stainless steel corrodes," *Nature*, vol. 415, pp. 770–774, February 14 2002.

[14] Q. Meng, G. S. Frankel, H. O. Colijn, and S. H. Goss, "Metallurgy (communication arising): Stainless-steel corrosion and MnS inclusions," *Nature*, vol. 424, pp. 389–390, July 24 2003.

[15] M. P. Ryan, D. E. Williams, R. J. Chater, B. M. Hutton, and D. S. McPhail, "Metallurgy (communication arising): Stainless-steel corrosion and mns inclusions," *Nature*, vol. 424, p. 390, July 24 2003.

[16] D. E. Williams, M. R. Kilburn, J. Cliff, and G. I. N. Waterhouse, "Composition changes around sulphide inclusions in stainless steels, and implications for the initiation of pitting corrosion," *Corrosion Science*, vol. 52, pp. 3702–3716, November 2010.

[17] G. T. Burstein, P. C. Pistorius, and S. P. Mattin, "The nucleation and growth of corrosion pits on stainless-steel," *Corrosion Science*, vol. 35, no. 1-4, pp. 57–62, 1993.

[18] N. J. Laycock, S. P. White, J. S. Noh, P. T. Wilson, and R. C. Newman, "Perforated covers for propagating pits," *Journal of the Electrochemical Society*, vol. 145, pp. 1101–1108, April 1998.

[19] N. J. Laycock and R. C. Newman, "Localised dissolution kinetics, salt films and pitting potentials," *Corrosion Science*, vol. 39, pp. 1771–1790, October-November 1997.

[20] P. C. Pistorius and G. T. Burstein, "Metastable pitting corrosion of stainless-steel and the transition to stability," *Philosophical Transactions of the Royal Society of London Series A-Mathematical Physical and Engineering Sciences*, vol. 341, pp. 531–559, December 15 1992.

[21] J. Mankowski and Z. Szklarska-Smialowska, "Studies on accumulation of chloride ions in pits growing during anodic polarization," *Corrosion Science*, vol. 15, pp. 493–501, 1975.

[22] H. D. Gesser, *Applied Chemistry: A Textbook for Engineers and Technologists*. New York: Kluwer Academic/Plenum Publishers, 2002.

[23] B. Wu, J. R. Scully, J. L. Hudson, and A. S. Mikhailov, "Cooperative stochastic behavior in localized corrosion: I. model," *Journal of the Electrochemical Society*, vol. 144, pp. 1614–1620, May 1997.

[24] T. T. Lunt, S. T. Pride, J. R. Scully, J. L. Hudson, and A. S. Mikhailov, "Cooperative stochastic behavior in localized corrosion: II. Experiments," *Journal of the Electrochemical Society*, vol. 144, pp. 1620–1629, May 1997.

[25] T. T. Lunt, J. R. Scully, V. Brusamarello, and A. S. Mikhailov, "Spatial interactions among localized corrosion sites: Experiments and modeling," *Journal of the Electrochemical Society*, vol. 149, no. 5, pp. B163–B173, 2002.

[26] L. Organ, J. R. Scully, A. S. Mikhailov, and J. L. Hudson, "A spatiotemporal model of interactions among metastable pits and the transition to pitting corrosion," *Electrochimica Acta*, vol. 51, pp. 225–241, October 10 2005.

[27] A. S. Mikhailov, S. Jain, L. Organ, and J. L. Hudson, "Cooperative stochastic behavior in the onset of localized corrosion," *Chaos*, vol. 16, p. 037104, 2006.

[28] L. Organ, Y. Tiwary, J. R. Scully, A. S. Mikhailov, and J. L. Hudson, "Interactions among metastable pits on heterogeneous electrodes," *Electrochimica Acta*, vol. 52, pp. 6784–6792, August 1 2007.

[29] C. Punckt, M. Bölscher, H. H. Rotermund, A. S. Mikhailov, L. Organ, N. Budiansky, J. R. Scully, and J. L. Hudson, "Sudden onset of pitting corrosion on stainless steel as a critical phenomenon," *Science*, vol. 305, pp. 1133–1136, August 20 2004.

[30] M. Dornhege, C. Punckt, J. L. Hudson, and H. H. Rotermund, "Spreading of corrosion on stainless steel simultaneous observation of metastable pits and oxide film," *Journal of the Electrochemical Society*, vol. 154, no. 1, pp. C24–C27, 2007.

[31] N. D. Budiansky, J. L. Hudson, and J. R. Scully, "Origins of persistent interaction among localized corrosion sites on stainless steel," *Journal of the Electrochemical Society*, vol. 151, no. 4, pp. B233–B243, 2004.

[32] H. H. Rotermund, G. Haas, R. U. Franz, R. M. Tromp, and G. Ertl, "Imaging pattern formation: Bridging the pressure gap," *Applied Physics A-Materials Science & Processing*, vol. 61, pp. 569–574, December 1995.

[33] H. H. Rotermund, G. Haas, R. U. Franz, R. M. Tromp, and G. Ertl, "Imaging pattern formation in surface reactions from ultrahigh vacuum up to atmospheric pressures," *Science*, vol. 270, no. 5236, pp. 608–610, 1995.

[34] G. Haas, R. U. Franz, H. H. Rotermund, R. M. Tromp, and G. Ertl, "Imaging surface reactions with light," *Surface Science*, vol. 352-354, pp. 1003–1006, 1996.

[35] H. H. Rotermund, "Imaging of dynamic patterns on surfaces by light," *Surface Science Reports*, vol. 29, no. 7-8, pp. 267–364, 1997. esp. pp. 277-292.

[36] H. H. Rotermund, "Imaging pattern formation in surface reactions from ultra-high vacuum up to atmospheric pressures," *Surface Science*, vol. 386, pp. 10–23, October 1997.

[37] H. H. Rotermund, "Imaging of dynamic patterns on surfaces," *Current Opinion in Solid State & Materials Science*, vol. 3, pp. 354–360, August 1998.

[38] M. A. Genshaw and R. S. Sirohi, "An ellipsometric study of chromium passivation," *Journal of the Electrochemical Society*, vol. 118, no. 10, pp. 1558–1563, 1971.

[39] W. M. b. M. Yunus and A. b. A. Rahman, "Refractive-index of solutions at high-concentrations," *Applied Optics*, vol. 27, pp. 3341–3343, August 15 1988.

[40] T. Scheimpflug, "Improved method and apparatus for the systematic alteration or distortion of plane pictures and images by means of lenses and mirrors for photography and for other purposes. patent no 1196." Patent Application, 1904.

[41] J. Carpentier, "Improvements in elarging or like cameras. patent no 1139." Patent Application, 1901.

[42] M. H. Jericho, H. J. Kreuzer, M. Kanka, and R. Riesenberg, "Quantitative phase and refractive index measurements with point-source digital in-line holographic microscopy," *Applied Optics*, vol. 51, pp. 1503–1515, April 2012.

[43] E. M. Purcell, "Life at low Reynolds number," *American Journal of Physics*, vol. 45, pp. 3–11, January 1977.

[44] X. G. Yang, S. H. Chen, C. Wang, and L. Li, "In-line digital holography for the study of dynamic processes of electrochemical reaction," *Electrochemistry Communications*, vol. 6, pp. 643–647, July 2004.

[45] X. Yang, S. Chen, L. Li, and C. Wang, "Digital holographic study of the effect of magnetic field on the potentiostatic current oscillations of iron in sulfuric acid," *Journal of Electroanalytical Chemistry*, vol. 586, pp. 173–179, 2006.

[46] H. Jia, S. Chen, B. Yuan, C. Wang, and L. Li, "Mapping the concentration changes during the dynamic processes of crevice corrosion by digital holographic reconstruction," *Journal of the Serbian Chemical Society*, vol. 74, no. 2, pp. 197–202, 2009.

[47] B. Yuan, C. Wang, L. Li, and S. Chen, "Real time observation of the anodic dissolution of copper in NaCl solution with the digital holography," *Electrochemistry Communications*, vol. 11, pp. 1373–1376, 2009.

[48] L. Wang, S. Chen, B. Yuan, F. Meng, J. Wang, C. Wang, and L. Li, "Digital holographic reconstruction detection of localized corrosion arising from scratches," *Journal of the Serbian Chemical Society*, vol. 75, no. 4, pp. 505–512, 2010.

[49] S. H. Chen, C. Wang, and X. L. Yu, "Investigation of iron anodic process in acidic solution by holographic microphotography," *Electrochimica Acta*, vol. 39, pp. 731–736, April 1994.

[50] L. Li, C. Wang, S. Chen, X. Hou, and X. Yang, "Investigation of the pitting of aluminum induced by chloride ions by holographic microphotography," *Journal of the Serbian Chemical Society*, vol. 73, no. 5, pp. 561–568, 2008.

[51] S. Hao, P. Wu, J. Zou, T. Grosdidier, and C. Dong, "Microstructure evolution occurring in the modified surface of 316L stainless steel under high current pulsed electron beam treatment," *Applied Surface Science*, vol. 253, pp. 5349–5354, 2007.

[52] K. Zhang, J. Zou, T. Grosdidier, C. Dong, and D. Yang, "Improved pitting corrosion resistance of aisi 316l stainless steel treated by high current pulsed electron beam," *Surface & Coatings Technology*, vol. 201, pp. 1393–1400, October 5 2006.

[53] R. K. Dayal, "Laser surface modification for improving localised corrosion resistance of austenitic stainless steels," in *Surface Modification Technologies X* (T. S. Sudarshan, K. A. Khor, and M. Jeandin, eds.), (Gower House, Croft Road, Aldershot, England), pp. 667–676, Ashgate Publishing Ltd, 1997.

[54] C. B. Breslin, C. Chen, and F. Mansfeld, "The electrochemical behaviour of stainless steels following surface modification in cerium-containing solutions," *Corrosion Science*, vol. 39, pp. 1061–1073, June 1997.

[55] S. Virtanen, M. B. Ives, G. I. Sproule, P. Schmuki, and M. J. Graham, "A surface analytical and electrochemical study on the role of cerium in the chemical surface treatment of stainless steels," *Corrosion Science*, vol. 39, pp. 1897–1913, October-November 1997.

[56] J. W. Goodman, *Introduction to Fourier Optics*. Englewood, Colorado: Roberts and Company Publishers, 2005.

[57] M. Born and E. Wolf, *Principles of Optics*. New York: Cambridge University Press, 7th ed., 1999.

[58] D. Gabor, "A new microscopic principle," *Nature*, vol. 161, pp. 777–778, May 1948.

[59] D. Gabor, "Microscopy by reconstructed wave-fronts," *Proceedings of the Royal Society of London Series A-Mathematical and Physical Sciences*, vol. 197, no. 1051, pp. 454–487, 1949.

[60] D. Gabor, "Microscopy by reconstructed wave-fronts 2," *Proceedings of the Physical Society of London Section B*, vol. 64, no. 378, pp. 449–469, 1951.

[61] D. Gabor, "Diffraction microscopy," *Research; A Journal of Science and its Applications*, vol. 4, no. 3, pp. 107–112, 1951.

[62] D. Gabor, G. W. Stroke, D. Brumm, A. Funkhous, and A. Labeyrie, "Reconstruction of phase objects by holography," *Nature*, vol. 208, no. 5016, pp. 1159–1162, 1965.

[63] D. Gabor and W. P. Goss, "Interference microscope with total wavefront reconstruction," *Journal of the Optical Society of America*, vol. 56, no. 7, pp. 849–858, 1966.

[64] D. Gabor, "Holography, 1948-1971," *Science*, vol. 177, pp. 299–313, July 28 1972.

[65] H. J. Kreuzer, K. Nakamura, A. Wierzbicki, H. W. Fink, and H. Schmid, "Theory of the point source electron microscope," *Ultramicroscopy*, vol. 45, pp. 381–403, November 1992.

[66] H. J. Kreuzer, H.-W. Fink, H. Schmid, and S. Bonev, "Holography of holes, with electrons and photons," *Journal of Microscopy*, vol. 178, no. 3, pp. 191–197, 1995.

[67] H. J. Kreuzer, "Low energy electron point source microscopy," *Micron*, vol. 26, no. 6, pp. 503–509, 1995.

[68] W. B. Xu, M. H. Jericho, I. A. Meinertzhagen, and H. J. Kreuzer, "Digital in-line holography for biological applications," *Proceedings of the National Academy of Sciences of the United States of America*, vol. 98, pp. 11301–11305, September 25 2001.

[69] H. J. Kreuzer, M. H. Jericho, I. A. Meinertzhagen, and W. B. Xu, "Digital in-line holography with photons and electrons," *Journal of Physics-Condensed Matter*, vol. 13, pp. 10729–10741, November 26 2001.

[70] H. J. Kreuzer, "Holographic microscope and method of hologram reconstruction." US Patent 6411406 B1, 2002.

[71] W. Xu, M. H. Jericho, I. A. Meinertzhagen, and H. J. Kreuzer, "Digital in-line holography of microspheres," *Applied Optics*, vol. 41, pp. 5367–5375, September 2002.

[72] W. Xu, M. H. Jericho, H. J. Kreuzer, and I. A. Meinertzhagen, "Tracking particles in four dimensions with in-line holographic microscopy," *Optics Letters*, vol. 28, pp. 164–166, February 1 2003.

[73] J. Garcia-Sucerquia, W. Xu, S. K. Jericho, M. H. Jericho, P. Klages, and H. J. Kreuzer, "Resolution power in digital in-line holography," in *ICO20: Optical Information Processing, Pts 1 and 2* (Y. L. Sheng, S. L. Zhuang, and Y. M. Zhang, eds.), vol. 6027, (Bellingham, WA), p. H272, SPIE, 2006.

[74] J. Garcia-Sucerquia, D. C. Alvarez-Palacio, M. H. Jericho, and H. J. Kreuzer, "Comment on "reconstruction algorithm for high-numerical-aperture holograms with diffraction-limited resolution"," *Optics Letters*, vol. 31, no. 19, pp. 2845–2847, 2006.

[75] S. K. Jericho, J. Garcia-Sucerquia, W. Xu, M. H. Jericho, and H. J. Kreuzer, "Submersible digital in-line holographic microscope," *Review of Scientific Instruments*, vol. 77, p. 043706, 2006.

[76] J. Garcia-Sucerquia, W. Xu, S. Jericho, P. Klages, M. H. Jericho, and H. J. Kreuzer, "Digital in-line holographic microscopy," *Applied Optics*, vol. 45, pp. 836–850, February 2006.

[77] J. Garcia-Sucerquia, W. B. Xu, M. H. Jericho, and H. J. Kreuzer, "Immersion digital in-line holographic microscopy," *Optics Letters*, vol. 31, pp. 1211–1213, May 1 2006.

[78] J. Garcia-Sucerquia, W. Xu, S. Jericho, M. Jericho, and H. Kreuzer, "4-d imaging of fluid flow with digital in-line holographic microscopy," *Optik - International Journal for Light and Electron Optics*, vol. 119, no. 9, pp. 419–423, 2008.

[79] M. H. Jericho and H. J. Kreuzer, *Coherent Light Microscopy*, ch. Point Source Digital In-Line Holographic Microscopy, pp. 3–30. Springer Series in Surface Sciences, New York: Springer-Verlag, 2011.

[80] J. W. Cooley and J. W. Tukey, "An algorithm for the calculation of complex fourier series," *Mathematics of Computation*, vol. 19, pp. 297–301, 1965.

[81] W. Gao and Q. Kemao, "Parallel computing in experimental mechanics and optical measurement: A review," *Optics and Lasers in Engineering*, vol. 50, pp. 608–617, April 2012.

[82] G. C. Sherman, "Application of the convolution theorem to rayleigh's integral formulas," *Journal of the Optical Society of America*, vol. 57, pp. 546–547, April 1967.

[83] J. T. Winthrop and C. R. Worthington, "Convolution formulation of fresnel diffraction," *Journal of the Optical Society of America*, vol. 56, pp. 588–591, May 1966.

[84] T. H. Demetrakopoulos and R. Mittra, "Digital and optical reconstruction of images from suboptical diffraction patterns," *Applied Optics*, vol. 13, pp. 665–670, March 1974.

[85] T. M. Kreis, M. Adams, and W. P. O. Juptner, "Methods of digital holography: A comparison," in *Optical Inspection and Micromeasurements II*, vol. 3098 of *Proceedings of the SPIE*, (Bellingham, WA), pp. 224–233, 1997.

[86] T. Kreis and W. Juptner, "Principles of digital holography," in *Fringe '97: Automatic Processing of Fringe Patterns* (W. Juptner and W. Osten, eds.), vol. 3 of *Verlag Series in Optical Metrology*, pp. 353–360, Akademie Verlag, Berlin, 1997.

[87] T. M. Kreis, W. P. O. Juptner, and J. Geldmacher, "Digital holography: Methods and applications," in *International Conference on Applied Optical Metrology* (P. Rastogi and F. Gyimesi, eds.), vol. 3407 of *Proceedings of the SPIE*, (Bellingham, WA), pp. 169–177, 1998.

[88] T. M. Kreis, "Frequency analysis of digital holography with reconstruction by convolution," *Optical Engineering*, vol. 41, pp. 1829–1839, August 2002.

[89] T. M. Kreis, *Handbook of holographic interferometry: optical and digital methods*, vol. 26. Wiley-VCH, 2005.

[90] U. Schnars and W. Jueptner, *Digital Holography*. Berlin: Springer-Verlag, 2005.

[91] T. Lenart, V. Owall, M. Gustafsson, M. Sebesta, and P. Egelberg, "Accelerating signal processing algorithms in digital holography using an FPGA platform," in *2003 IEEE International Conference on Field-Programmable Technology (FPT), Proceedings*, (New York, NY), IEEE, 2003.

[92] M. Gustafsson, M. Sebesta, B. Bengtsson, S. Pettersson, P. Egelberg, and T. Lenart, "High-resolution digital transmission microscopy: a Fourier holography approach," *Optics and Lasers in Engineering*, vol. 41, pp. 553–563, March 2004.

[93] T. Lenart, M. Gustafsson, and V. Oewall, "A hardware acceleration platform for digital holographic imaging," *Journal of Signal Processing Systems for Signal Image and Video Technology*, vol. 52, pp. 297–311, September 2008.

[94] "Resolution Optics Corporate Website," Available at: http://resolutionoptics.com/ Last accessed June 17, 2012.

[95] G. T. Burstein and S. P. Vines, "Repetitive nucleation of corrosion pits on stainless steel and the effects of surface roughness," *Journal of the Electrochemical Society*, vol. 148, pp. B504–B516, December 2001.

[96] J. R. Galvele, "Transport processes and mechanism of pitting of metals," *Journal of the Electrochemical Society*, vol. 123, no. 4, pp. 464–474, 1976.

[97] I. Reynaud-Laporte, M. Vayer, J. P. Kauffmann, and R. Erre, "An electrochemical-AFM study of the initiation of the pitting of a martensitic stainless steel," *Microscopy Microanalysis Microstructures*, vol. 8, pp. 175–185, June 1997.

[98] A. Miyasaka and H. Ogawa, "In situ observation of a stainless-steel surface in aqueous-solutions using scanning tunneling microscope," *Corrosion Science*, vol. 31, pp. 99–104, 1990.

[99] K. Habib, "Detection of crevice corrosion by optical interferometry," *Corrosion Science*, vol. 42, pp. 455–467, March 2000.

[100] L. Li, C. Wang, S. Chen, X. Yang, B. Yuan, and H. Jia, "An investigation on general corrosion and pitting of iron with the in-line digital holography," *Electrochimica Acta*, vol. 53, pp. 3109–3119, February 25 2008.

[101] G. S. Eklund, "Initiation of pitting at sulfide inclusions in stainless-steel," *Journal of the Electrochemical Society*, vol. 121, no. 4, pp. 467–473, 1974.

[102] T. L. S. L. Wijesinghe and D. J. Blackwood, "Real time pit initiation studies on stainless steels: The effect of sulphide inclusions," *Corrosion Science*, vol. 49, pp. 1755–1764, April 2007.

[103] P. E. Klages, M. K. Rotermund, and H. H. Rotermund, "Simultaneous Holographic, Ellipsometric, and Optical Imaging of Pitting Corrosion on SS 316LVM," *Corrosion Science*, Submitted 2012.

[104] P. Amsler, O. Stetzer, M. Schnaiter, E. Hesse, S. Benz, O. Moehler, and U. Lohmann, "Ice crystal habits from cloud chamber studies obtained by in-line holographic microscopy related to depolarization measurements," *Applied Optics*, vol. 48, pp. 5811–5822, October 2009.

[105] S. Weisse, M. Heydt, T. Maier, S. Schulz, J. P. Spatz, M. Grunze, T. Haraszti, and A. Rosenhahn, "Flow conditions in the vicinity of microstructured interfaces studied by holography and implications for the assembly of artificial actin networks," *Physical Chemistry Chemical Physics*, vol. 13, pp. 13395–13402, 2011.

[106] J. J. Barton, "Photoelectron holography," *Physical Review Letters*, vol. 61, pp. 1356–1359, September 19 1988.

[107] "Sigma SD1 Merrill Image Capture System," Available at: http://www.sigma-sd.com/SD1Merrill/system.html Last accessed June 17, 2012 2012.

[108] R. M. Turner and R. J. Guttosch, "Development challenges of a new image capture technology: Foveon X3 image sensors," in *ICIS '06: International Congress of Imaging Science, Final Program and Proceedings: Linking the Explosion of Imaging Applications with the Science and Technology of Imaging*, (Springfield, VA), pp. 175–181, Soc Imaging Science & Technology, 2006.

[109] S. K. Jericho, P. Klages, J. Nadeau, E. M. Dumas, M. H. Jericho, and H. J. Kreuzer, "In-line digital holographic microscopy for terrestrial and exobiological research," *Planetary and Space Science*, vol. 58, pp. 701–705, March 2010.

Appendix A

The Rayleigh-Sommerfeld Diffraction Integral

The Green's function chosen for the Kirchhoff-Fresnel Diffraction Integral in Equation 1.8 implies that both the value of the wave, and its derivative with respect to the surface normal are known everywhere. Mathematical objections to this arose, because if the value and normal derivative were equal to zero at some portion of the volume (as was stated in the derivation) they should technically be equal to zero everywhere on the surface of integration. Born and Wolf [57] and Goodman [56] note that the theory is generally adequate and accurate away from the region closest to the aperture/recording screen, so long as the aperture/recording screen is significantly larger than the wavelength of light. Goodman also notes that 'self-consistent' math doesn't mean that the method is necessarily more accurate.

Sommerfeld found two solutions that compensate for the mathematical inconsistencies in the case of an aperture in a planar metal sheet; one solution depends on the complex values for the wave at the aperture and one depends on the normal derivatives. His choice of Green's functions were two point sources on opposite sides of the screen 180° out of phase with each other [56]:

$$G_-(P) = \frac{\exp(ik|\mathbf{r}_2|)}{|\mathbf{r}_2|} - \frac{\exp(ik|-\mathbf{r}_2|)}{|-\mathbf{r}_2|} \tag{A.1}$$

in which case the contribution of G_- at the screen is 0 and derivative of G_- with respect to the normal is twice the value in the Kirchhoff-Fresnel solution. His second solution involves two point sources on opposite sides of the screen that are in phase with each other

$$G_+(P) = \frac{\exp(ik|\mathbf{r}_2|)}{|\mathbf{r}_2|} + \frac{\exp(ik|-\mathbf{r}_2|)}{|-\mathbf{r}_2|} \tag{A.2}$$

in which case the derivative of G_+ with respect to the normal disappears everywhere along the planar metal sheet and the contribution of G_+ is twice that of G from the Kirchhoff-Fresnel solution. The final solutions, dependent only on either U or $\partial U/\partial n$ are

$$
\begin{aligned}
RS(I) : U(\mathbf{P}) &= \frac{ik}{2\pi} \int \int_\Sigma A_{ref} \frac{\exp(ik|\mathbf{r}|)}{|\mathbf{r}|} \frac{\exp(ik|\mathbf{r_2}|)}{|\mathbf{r_2}|} \cos(\mathbf{r}, \mathbf{n}) ds \\
RS(II) : U(\mathbf{P}) &= \frac{ik}{2\pi} \int \int_\Sigma A_{ref} \frac{\exp(ik|\mathbf{r}|)}{|\mathbf{r}|} \frac{\exp(ik|\mathbf{r_2}|)}{|\mathbf{r_2}|} [-\cos(\mathbf{r_2}, \mathbf{n})] ds
\end{aligned}
$$

$$(\text{A.3})$$

The math is now consistent, though the problem that is solved resembles the recording setup for holography less.

Appendix B

Multimedia Descriptions

Included with this thesis are QuickTime .mov files. File descriptions have been included as footnotes in their respective chapters, but they are also repeated here for clarity.

Video Clip 1.1: NeutralDensityFilterTest.mov

Duration: 3 min 19 s. First reference on page 12.

A movie demonstrating the effect of the HeNe laser used in an EMSI configuration on the flow pattern of the 5 μm beads. When the EMSI laser is turned on, the dominant effect is that the beads move upwards through the cuvette. When a neutral density filter (0.0005 transmission) is used on the HeNe laser, the amount of energy at the wire face is on the order of μW and beads are no longer affected.

Video Clip 1.2: BeadPathMay3_2010-30s.mov

Duration: 30 s. First reference on page 13.

A movie showing how large pitting events affect the paths of 5 μm beads. While the potential is high, the large pit causes changes in the index of refraction such that light is bent into the geometric shadow of the wire. The bead paths get changed by the active pits. When the potentiostat is set to the initial potential, the anodic current immediately drops and the effects on the bead paths stop.

Video Clip 2.1: klages_CorrSci_videoClip2_1.mov

Duration: 7 s. First reference on page 42.

Time synchronized data sets for a corrosion experiment of SS 316LVM in 0.9 % by

mass NaCl solution. This video shows the first metastable pitting event observed with microscopy, EMSI, and holography during the experiment. The resulting pit is located near the right edge of the wire. Since the reconstructions are based on sequentially paired holograms, only changes in the solution at the end of the event occur rapidly enough to show as bright regions.

Video Clip 2.2: klages_CorrSci_videoClip2_2.mov

Duration: 5 s. First reference on page 42.

Time synchronized data sets for a corrosion experiment of SS 316LVM in 0.9 % by mass NaCl solution. This is the same event that was reanalyzed with a reference hologram from before the event (figure 2.4) and shows how the sensitivity to changes in the solution is limited when sequentially paired holograms are used.

Video Clip 2.3: klages_CorrSci_videoClip2_3.mov

Duration 8 s. First reference on page 46.

Time synchronized data sets for a corrosion experiment of SS 316LVM in 0.9 % by mass NaCl solution. This video clip shows a particle being ejected from the large pitting site (most clearly seen in the background subtracted microscope images). The particle comes into focus in the holographic reconstructions approximately 5 s into the clip. This video also shows multiple simultaneous events. As these events end, the anodic current drops suddenly and bright flashes are seen in the holographic reconstructions.

Appendix C

Copyright Permission

This appendix contains the copyright permissions required to reprint published material. Since clause 20 of the agreement is worded awkwardly, oral confirmation that this agreement is sufficient for the thesis to be archived with the Library and Archives of Canada was obtained from the Global Rights Department of Elsevier.

C.1 Elsevier License Terms and Conditions

This is a License Agreement between Peter Klages ("You") and Elsevier ("Elsevier") provided by Copyright Clearance Center ("CCC"). The license consists of your order details, the terms and conditions provided by Elsevier, and the payment terms and conditions.

All payments must be made in full to CCC. For payment instructions, please see information listed at the bottom of this form.

Supplier	Elsevier Limited The Boulevard, Langford Lane Kidlington, Oxford, OX5 1GB, UK
Registered Company Number	1982084
Customer Name	Peter Klages
Customer Address	6259 Coburg Road Halifax, NS, B3H 2A2

License Number	2927640817086
License Date	Jun 14, 2012
Licensed Content Publisher	Elsevier
Licensed Content Publication	Electrochemistry Communications
Licensed Content Title	Enhancing resistance to pitting corrosion in mechanically polished stainless steel 316 LVM by water treatment
Licensed Content Author	P.E. Klages, Z. Bai, M. Lobban, M.K. Rotermund, H.H. Rotermund
Licensed Content Date	February 2012
Licensed Content Volume Number	15
Licensed Content Issue Number	1
Number of Pages	5
Start Page	54
End Page	58
Type of Use	reuse in a thesis/dissertation
Portion	full article
Format	both print and electronic
Are You the Author of this Elsevier Article	Yes
Will you be translating	No
Order Reference Number	

Title of Your Thesis/Dissertation	In Situ Real-time Visualization and Corrosion Testing of Stainless Steel 316LVM with Emphasis on Digital In-line Holographic Microscopy
Expected Completion Date	Aug 2012
Estimated Size (number of pages)	100
Elsevier VAT number	GB 494 6272 12
Permissions Price	0.00 USD
VAT/Local Sales Tax	0.0 USD / 0.0 GBP
Total	0.00 USD

Terms and Conditions

INTRODUCTION

1. The publisher for this copyrighted material is Elsevier. By clicking "accept" in connection with completing this licensing transaction, you agree that the following terms and conditions apply to this transaction (along with the Billing and Payment terms and conditions established by Copyright Clearance Center, Inc. ("CCC"), at the time that you opened your Rightslink account and that are available at any time at http://myaccount.copyright.com).

GENERAL TERMS

2. Elsevier hereby grants you permission to reproduce the aforementioned material subject to the terms and conditions indicated.

3. Acknowledgement: If any part of the material to be used (for example, figures) has appeared in our publication with credit or acknowledgement to another source, permission must also be sought from that source. If such permission is not obtained then that material may not be included in your publication/copies. Suitable acknowledgement to the source must be made, either as a footnote or in a reference list at the end of your publication, as follows:

"Reprinted from Publication title, Vol /edition number, Author(s), Title of article / title of chapter, Pages No., Copyright (Year), with permission from Elsevier [OR APPLICABLE SOCIETY COPYRIGHT OWNER]." Also Lancet special credit - "Reprinted from The Lancet, Vol. number, Author(s), Title of article, Pages No., Copyright (Year), with permission from Elsevier."

4. Reproduction of this material is confined to the purpose and/or media for which permission is hereby given.

5. Altering/Modifying Material: Not Permitted. However figures and illustrations may be altered/adapted minimally to serve your work. Any other abbreviations, additions, deletions and/or any other alterations shall be made only with prior written authorization of Elsevier Ltd. (Please contact Elsevier at permissions@elsevier.com)

6. If the permission fee for the requested use of our material is waived in this instance, please be advised that your future requests for Elsevier materials may attract a fee.

7. Reservation of Rights: Publisher reserves all rights not specifically granted in the combination of (i) the license details provided by you and accepted in the course of this licensing transaction, (ii) these terms and conditions and (iii) CCC's Billing and Payment terms and conditions.

8. License Contingent Upon Payment: While you may exercise the rights licensed immediately upon issuance of the license at the end of the licensing process for the transaction, provided that you have disclosed complete and accurate details of your proposed use, no license is finally effective unless and until full payment is received

from you (either by publisher or by CCC) as provided in CCC's Billing and Payment terms and conditions. If full payment is not received on a timely basis, then any license preliminarily granted shall be deemed automatically revoked and shall be void as if never granted. Further, in the event that you breach any of these terms and conditions or any of CCC's Billing and Payment terms and conditions, the license is automatically revoked and shall be void as if never granted. Use of materials as described in a revoked license, as well as any use of the materials beyond the scope of an unrevoked license, may constitute copyright infringement and publisher reserves the right to take any and all action to protect its copyright in the materials.

9. Warranties: Publisher makes no representations or warranties with respect to the licensed material.

10. Indemnity: You hereby indemnify and agree to hold harmless publisher and CCC, and their respective officers, directors, employees and agents, from and against any and all claims arising out of your use of the licensed material other than as specifically authorized pursuant to this license.

11. No Transfer of License: This license is personal to you and may not be sublicensed, assigned, or transferred by you to any other person without publisher's written permission.

12. No Amendment Except in Writing: This license may not be amended except in a writing signed by both parties (or, in the case of publisher, by CCC on publisher's behalf).

13. Objection to Contrary Terms: Publisher hereby objects to any terms contained in any purchase order, acknowledgment, check endorsement or other writing prepared by you, which terms are inconsistent with these terms and conditions or CCC's Billing and Payment terms and conditions. These terms and conditions, together with CCC's Billing and Payment terms and conditions (which are incorporated herein), comprise the entire agreement between you and publisher (and CCC) concerning this licensing

transaction. In the event of any conflict between your obligations established by these terms and conditions and those established by CCC's Billing and Payment terms and conditions, these terms and conditions shall control.

14. Revocation: Elsevier or Copyright Clearance Center may deny the permissions described in this License at their sole discretion, for any reason or no reason, with a full refund payable to you. Notice of such denial will be made using the contact information provided by you. Failure to receive such notice will not alter or invalidate the denial. In no event will Elsevier or Copyright Clearance Center be responsible or liable for any costs, expenses or damage incurred by you as a result of a denial of your permission request, other than a refund of the amount(s) paid by you to Elsevier and/or Copyright Clearance Center for denied permissions.

LIMITED LICENSE

The following terms and conditions apply only to specific license types:

15. **Translation:** This permission is granted for non-exclusive world **English** rights only unless your license was granted for translation rights. If you licensed translation rights you may only translate this content into the languages you requested. A professional translator must perform all translations and reproduce the content word for word preserving the integrity of the article. If this license is to re-use 1 or 2 figures then permission is granted for non-exclusive world rights in all languages.

16. **Website:** The following terms and conditions apply to electronic reserve and author websites:

Electronic reserve: If licensed material is to be posted to website, the web site is to be password-protected and made available only to bona fide students registered on a relevant course if:

This license was made in connection with a course,

This permission is granted for 1 year only. You may obtain a license for future website

posting,

All content posted to the web site must maintain the copyright information line on the bottom of each image,

A hyper-text must be included to the Homepage of the journal from which you are licensing at http://www.sciencedirect.com/science/journal/xxxxx or the Elsevier homepage for books at http://www.elsevier.com, and

Central Storage: This license does not include permission for a scanned version of the material to be stored in a central repository such as that provided by Heron/XanEdu.

17. **Author website** for journals with the following additional clauses:

All content posted to the web site must maintain the copyright information line on the bottom of each image, and the permission granted is limited to the personal version of your paper. You are not allowed to download and post the published electronic version of your article (whether PDF or HTML, proof or final version), nor may you scan the printed edition to create an electronic version. A hyper-text must be included to the Homepage of the journal from which you are licensing at http://www.sciencedirect.com/science/journal/xxxxx. As part of our normal production process, you will receive an e-mail notice when your article appears on Elsevier's online service ScienceDirect (www.sciencedirect.com). That e-mail will include the article's Digital Object Identifier (DOI). This number provides the electronic link to the published article and should be included in the posting of your personal version. We ask that you wait until you receive this e-mail and have the DOI to do any posting.

Central Storage: This license does not include permission for a scanned version of the material to be stored in a central repository such as that provided by Heron/XanEdu.

18. **Author website** for books with the following additional clauses:

Authors are permitted to place a brief summary of their work online only.

A hyper-text must be included to the Elsevier homepage at http://www.elsevier.com.

All content posted to the web site must maintain the copyright information line on

the bottom of each image. You are not allowed to download and post the published electronic version of your chapter, nor may you scan the printed edition to create an electronic version.

Central Storage: This license does not include permission for a scanned version of the material to be stored in a central repository such as that provided by Heron/XanEdu.

19. **Website** (regular and for author): A hyper-text must be included to the Homepage of the journal from which you are licensing at

http://www.sciencedirect.com/science/journal/xxxxx or for books to the Elsevier homepage at http://www.elsevier.com.

20. **Thesis/Dissertation:** If your license is for use in a thesis/dissertation your thesis may be submitted to your institution in either print or electronic form. Should your thesis be published commercially, please reapply for permission. These requirements include permission for the Library and Archives of Canada to supply single copies, on demand, of the complete thesis and include permission for UMI to supply single copies, on demand, of the complete thesis. Should your thesis be published commercially, please reapply for permission.

21. **Other Conditions:**

v1.6

If you would like to pay for this license now, please remit this license along with your payment made payable to "COPYRIGHT CLEARANCE CENTER" otherwise you will be invoiced within 48 hours of the license date. Payment should be in the form of a check or money order referencing your account number and this invoice number RLNK500799231.
Once you receive your invoice for this order, you may pay your invoice by credit card. Please follow instructions provided at that time.

Make Payment To:

Copyright Clearance Center
Dept 001
P.O. Box 843006
Boston, MA 02284-3006

For suggestions or comments regarding this order, contact RightsLink Customer Support: customercare@copyright.com or +1-877-622-5543 (toll free in the US) or +1-978-646-2777.

Gratis licenses (referencing $0 in the Total field) are free. Please retain this printable license for your reference. No payment is required.